Photocatalytic hydrogen production using metal doped TiO_2: A review of recent advances

Vignesh Kumaravel[a,b,*], Snehamol Mathew[a,b], John Bartlett[a,b], Suresh C. Pillai[a,b,*]

[a] Nanotechnology and Bio-Engineering Research Group, Department of Environmental Science, School of Science, Institute of Technology Sligo, Ash Lane, Sligo, Ireland
[b] Centre for Precision Engineering, Materials and Manufacturing Research (PEM), Institute of Technology Sligo, Ash Lane, Sligo, Ireland

ABSTRACT

Hydrogen (H_2) production *via* photocatalytic water splitting is one of the most promising technologies for clean solar energy conversion to emerge in recent decades. The achievement of energy production from water splitting would mean that we could use water as a fuel for future energy need. Among the various photocatalytic materials, titanium dioxide (TiO_2) is the dominant and most widely studied because of its exceptional physicochemical characteristics. Surface decoration of metal/non-metal on TiO_2 nanoparticles is an outstanding technique to revamp its electronic properties and enrich the H_2 production efficiency. Metal dopants play a vital role in separation of electron-hole pairs on the TiO_2 surface during UV/visible/simulated solar light irradiation. In this paper, the basic principles, photocatalytic-reactor design, kinetics, key findings, and the mechanism of metal-doped TiO_2 are comprehensively reviewed. We found that Langmuir-Hinshelwood kinetic model is commonly employed by the researchers to demonstrate the rate of H_2 production. Copper (Cu), gold (Au) and platinum (Pt) are the most widely studied dopants for TiO_2, owing to their superior work function. The metal dopants can amplify the H_2 production efficiency of TiO_2 through Schottky barrier formation, surface plasmon resonance (SPR), generation of gap states by interaction with TiO_2 VB states. The recent advances and important consequences of 2D materials, perovskites, and other novel photocatalysts for H_2 generation have also been reviewed.

1. Introduction

High-energy demand, depletion of fossil fuels and environmental pollution have become major global challenges in recent years [1–5]. The utilization of clean and inexhaustible solar energy is essential to avoid the effects of greenhouse gases and to secure energy supply for the future. Thousands of research articles are published every year on the subject of solar energy conversion techniques such as photocatalytic degradation of emerging organic pollutants, hydrogen (H_2) production *via* photocatalytic water splitting, photovoltaics, and dye sensitized solar cells (DSSC). The photoelectrochemical water splitting by Fujishima and Honda in 1972 is one of the most significant of these [6]. Since then, H_2 production *via* water splitting has become the most promising clean energy technology with minimal impact to the environment [7–9]. Titanium oxide (TiO_2) [10–12], graphitic-carbon nitride (g-C_3N_4) [13–15] and cadmium sulfide (CdS) [16–18] are three extensively studied photocatalysts for water splitting in recent decades. Among them, TiO_2 is more superior, and a benchmark photocatalyst

owing to its photostability, high efficiency, appropriate band edge positions, biocompatibility and non-toxic nature [19–24].

The molecular orbital interactions between titanium (Ti) and oxygen (O) of TiO_2 are shown in Fig. 1. The "*d*" orbitals of Ti and "*p*" orbitals of O are mainly contribute to the bonding and antibonding orbitals [25]. The energy difference between the lowest unoccupied molecular orbital (*i.e.* CB) and highest occupied molecular orbital (*i.e.* VB) is known as bandgap energy (Eg). The bandgap energy of TiO_2 anatase is ~ 3.2 eV. The photocatalytic mechanism of TiO_2 water splitting is illustrated in Fig. 2 [26]. Three significant steps are involved [26]: (1) absorption of photons ($\lambda \geq$ bandgap energy) and generation of electron-hole pairs; (2) separation and migration of electron or hole from the bulk to the surface (or recombination of electron-hole pairs in the bulk material); (3) photo-reduction (H^+ to H_2) and photo-oxidation reactions (H_2O to O_2) at the surface.

The activity of a photocatalyst is strongly ruled by the kinetics of these three steps. H_2 production rate of TiO_2 is proportional to the quantity of photo-excited electrons at the water/TiO_2 interface. The
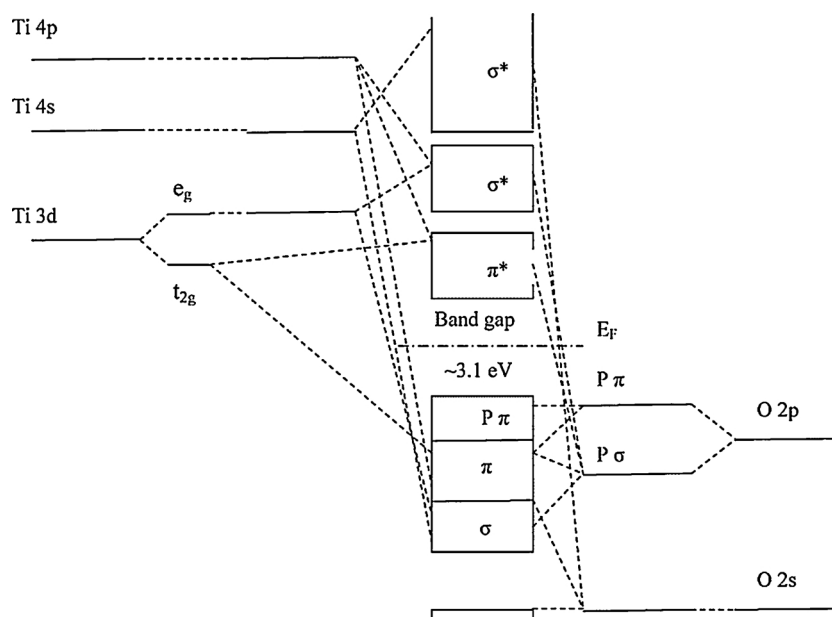
Fig. 1. Schematic representation of molecular orbital interactions between titanium (Ti) and oxygen (O) of TiO$_2$ [25]. Reproduced with permission from ref. [25]. Copyright (2012), Royal Society of Chemistry.
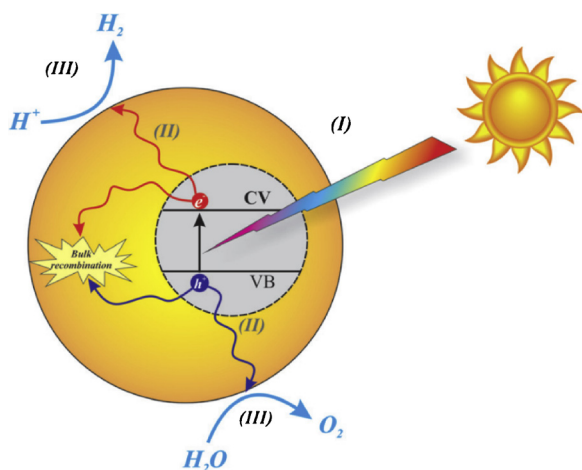

Fig. 2. Schematic representation of the important steps in photocatalytic water splitting using semiconductors [26]. Reproduced with permission from ref. [26]. Copyright (2015), Royal Society of Chemistry.

overall quantum yield is estimated from the number of incident photons and the number of H$_2$ molecules evolved [27]. To facilitate an efficient water splitting, the CB minimum (CBM) edge of a photocatalyst should be smaller than the H$^+$/H$_2$ reduction potential (0 V *vs*. NHE) and the VB maximum (VBM) edge must be greater than the H$_2$O/O$_2$ oxidation potential (+1.23 V *vs*. NHE), respectively. The overall water splitting of TiO$_2$ is comprised of two half reactions:

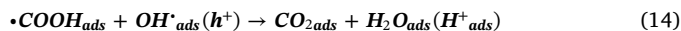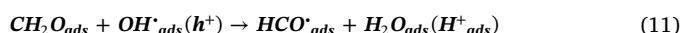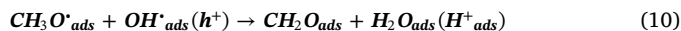$$H_2O + h^+_{VB} \rightarrow 2H^+ + \tfrac{1}{2} O_2 \tag{1}$$

$$2H^+ + 2e^-_{CB} \rightarrow H_2 \tag{2}$$

The overall reaction:

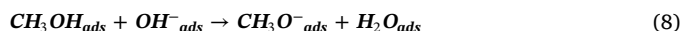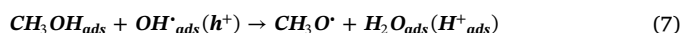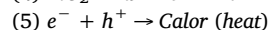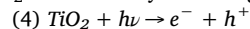$$H_2O \rightarrow H_2 + \tfrac{1}{2} O_2 \tag{3}$$

The timespan of reactive species produced during TiO$_2$ photocatalytic reaction is shown in Fig. 3 [28]. Interfacial charge transfer, recombination and trapping are the important photo-induced reactions inside and on the surface of TiO$_2$. The time-span of the reactions was predicted with the help of time resolved absorption spectroscopy.

Interfacial redox reactions are commonly responsible for the photodegradation of organic pollutants. For photocatalytic H$_2$ production, the efficiency of TiO$_2$ is mainly ruled by the surface trapping reactions. Fig. 3 shows that the time-scale of surface reactions is very low (in the range of picoseconds to femtoseconds). Hence, the photo-generated electrons should be effectively utilized on the catalyst surface to avoid its recombination with holes in the bulk.

Photocatalytic water splitting is energetically an uphill reaction (Gibbs free energy $\Delta H_0 = 286 \, kJ \, mol^{-1}$) [29]. Consequently, the experiments are carried out in the presence of electron donors (sacrificial agents) such as methanol [30,31] (commonly used for TiO$_2$), tri-ethanolamine [32,33] (commonly used for g-C$_3$N$_4$), sodium sulfide/sodium sulfite mixture [34,35] (commonly used for CdS) to avoid a backward reaction. The schematic of photocatalytic water splitting in the presence of sacrificial agents is shown in Fig. 4. The photo-generated holes can be easily consumed by the sacrificial agents, owing to their less positive oxidation potential when compared to H$_2$O. This would lead to the accumulation of photo-generated electrons on the catalyst surface for its reaction with H$^+$.

The important reactions for the photocatalytic H$_2$ production using TiO$_2$ - methanol system are given as follows [36]:

$$(4) \ TiO_2 + h\nu \rightarrow e^- + h^+$$

$$(5) \ e^- + h^+ \rightarrow Calor \ (heat)$$

$$H_2O_{ads} + h^+ \rightarrow OH^{\bullet}_{ads} + H^+_{ads} \tag{6}$$

$$CH_3OH_{ads} + OH^{\bullet}_{ads}(h^+) \rightarrow CH_3O^{\bullet} + H_2O_{ads}(H^+_{ads}) \tag{7}$$

$$CH_3OH_{ads} + OH^-_{ads} \rightarrow CH_3O^-_{ads} + H_2O_{ads} \tag{8}$$

$$CH_3O^{\bullet} + CH_3O^-_{ads} + H^+ \rightarrow 2CH_2O_{ads} + H^+ + e^- \tag{9}$$

$$CH_3O^{\bullet}_{ads} + OH^{\bullet}_{ads}(h^+) \rightarrow CH_2O_{ads} + H_2O_{ads}(H^+_{ads}) \tag{10}$$

$$CH_2O_{ads} + OH^{\bullet}_{ads}(h^+) \rightarrow HCO^{\bullet}_{ads} + H_2O_{ads}(H^+_{ads}) \tag{11}$$

$$HCO^{\bullet}_{ads} + OH^{\bullet}_{ads} \rightarrow HCOOH_{ads} \tag{12}$$

$$HCOOH_{ads} + OH^{\bullet}_{ads}(h^+) \rightarrow \, ^{\bullet}COOH_{ads} + H_2O_{ads}(H^+_{ads}) \tag{13}$$

$$^{\bullet}COOH_{ads} + OH^{\bullet}_{ads}(h^+) \rightarrow CO_{2ads} + H_2O_{ads}(H^+_{ads}) \tag{14}$$

$$2H^+_{ads} + 2e^- \rightarrow H_2 \tag{15}$$

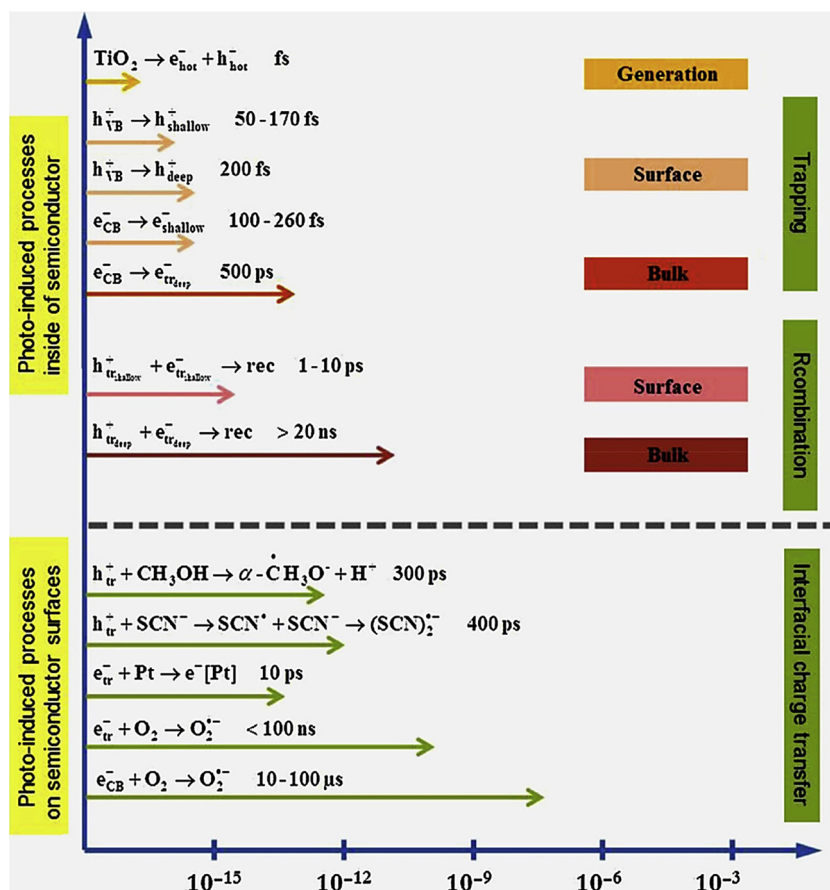Quantum efficiency (Q.E) is the generally recommended parameter

Fig. 3. The time-span of reactive species produced during TiO$_2$ photocatalytic reaction [28]. Reproduced with permission from ref. [28]. Copyright (2014), American Chemical Society.

to perform a quantitative comparison of a photocatalyst with other literature [37–42]. Q.E. is the ratio of number of H$_2$ molecules produced and the number of photons interacting with the photocatalyst. The quantum and photonic (also called as apparent quantum efficiency) efficiencies can be determined as follows:

$$Quantum\ efficiency\ (\%) = 100 \times \frac{n \times r\ (mol\ m^{-3}s^{-1})}{e^a\ (Einstein\ m^{-3}s^{-1})} \qquad (16)$$

$$Photonic\ efficiency\ (\%) = 100 \times \frac{n \times r\ (mol\ m^{-2}s^{-1})\ \times\ V\ (m^3)}{q\ (Einstein\ m^{-3}s^{-1})\ \times\ A\ (m^2)} \qquad (17)$$

Where, n is equal to 1 or 2 depending on the photocatalytic mechanism, r is the rate of reaction, e^a is the local volumetric rate of photon absorption (LVRPA - for liquid phase), q is the incident radiation flux averaged at the light irradiated photo-reactor surface (A) and V is the volume of photo-reactor. In most of the works, the value of n is considered as 2 (*i.e.* transfer of two electrons is required to produce one H$_2$ molecule). Nevertheless, there is a possibility of "current doubling effect" [36,43–45] during the photocatalytic H$_2$ production. In this situation, the hole scavenger (*e.g.* methanol) is altered into a radical anion intermediate (Eq. (8)) and then it injects an electron into the CB of TiO$_2$ (Eq. (9)). Only one photon is required (*i.e.* n is equal to 1) to produce one H$_2$ molecule when the "current doubling effect" is considered. Alternatively, the hole scavenger radical anion could react with the $^\bullet$OH radical to produce H$^+$ (Eq. (10)).

The wide band of pristine TiO$_2$ is not appropriate to receive the visible light for practical applications [46,47]. Moreover, the quantum yield of pristine TiO$_2$ is not remarkable even in the presence of sacrificial agents, because the H$_2$ production efficiency of pristine TiO$_2$ is
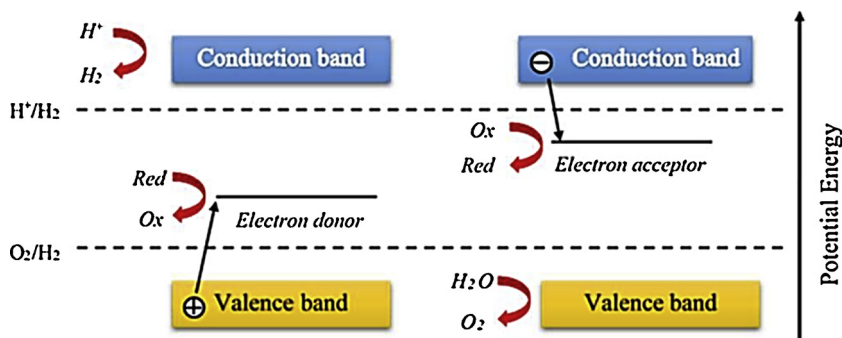

Fig. 4. Schematic of photocatalytic water splitting in the presence of electron donors and acceptors [26]. Reproduced with permission from ref. [26]. Copyright (2015), Royal Society of Chemistry.

Fig. 5. The list of dopants used to enhance the H_2 production efficiency of TiO_2.

influenced by high or unavoidable electron-hole recombination process at the surface or within the bulk [23,48–51]. Various strategies have been reported to tune the bandgap and regulate the electronic properties of TiO_2, such as sensitization with dyes [52,53] or graphene [54,55], use of nanocomposites [56–58], and doping of metals [59–62] or non-metals [63,64]. Among these different approaches, doping with metal ions (the introduction of foreign elements without affecting the original crystallinity of TiO_2) is the most promising option, since it directly influences the surface electronic characteristics of TiO_2. Dopants can act as systematic electron taps, upgrade the electron-hole transfer/migration/separation, red shift the bandgap absorption to visible light, provide additional active sites for the photochemical reactions (especially $H^·$ combination) at the surface and minimize the over-potential required for H_2 evolution reaction. The outer shell electronic configuration, distribution and concentration of the dopants are very important in amplification of the H_2 production efficiency of TiO_2. Both anionic (e.g: C, N, S, F) [63–74] and cationic dopants (transition and inner transition metals, noble metals, rare earths) [61,69,75–100] have been used to tune the optical and electrical properties of pristine TiO_2. Fig. 5 shows the list of dopants studied to enhance the H_2 production efficiency of TiO_2. Pt [101–108], Au [59,109–116], Cu [117–128], and N [63,64,67–71] are the most widely studied dopants because of their high work function.

Table 1 summarizes the key findings of metal-doped TiO_2 developed in recent years for H_2 production [62,67,68,86,87,129–146]. The results showed that maximum H_2 production is achieved when Cu, Au and Pt are used as dopants in the range of 1% - 5%. Xenon (Xe) arc and high-pressure mercury (Hg) lamps were commonly used as light irradiation sources for visible/simulated solar light and UV light irradiation respectively. It is also noted that the efficiency of TiO_2 is significantly enhanced when more than one dopant is used.

Most of the review articles in photocatalysis highlight the applications of TiO_2 for environmental remediation (air pollution, water pollution, and self-cleaning surfaces) and microbial disinfection [152–164]. Some insightful review articles have been published for photocatalytic water splitting in numerous aspects such as fundamental concepts, theoretical principles, nature of photocatalyst (composition, shape, dimension, surface features and light absorption capacity), role

of co-catalyst, role of sacrificial agents, photocatalysis mechanism, etc [50,165–179]. There are no comprehensive review articles on metal-doped TiO_2 for H_2 production. The main aim of this article is to review the recent advancements, key findings, and photocatalytic mechanisms of metal-doped TiO_2 for H_2 production.

2. Mechanism of metal doped TiO_2 photocatalysts for H_2 generation

A schematic illustration of H_2 production *via* TiO_2 water splitting is shown in Fig. 6. H_2 production is accomplished through three important steps: (i) Under light irradiation, TiO_2 absorbs light with energy equal to, or greater than, the bandgap energy and the electrons are excited from the VB to the CB [8,158,159,180]. Consequently, electron and hole pairs are created in the CB and VB, respectively. (ii) The photo-excited electron and hole can easily migrate to the surface of TiO_2 (iii) hydrogen (H^+) ions are reduced into molecular hydrogen (H_2) by the electrons in the CB; H_2O is oxidized into oxygen (O_2) by the holes in the VB.

Owing to the less positive oxidation potential, the sacrificial agents can react more quickly with holes than H_2O. This would lead to the accumulation of electrons on the TiO_2 surface for the photo-reduction. The metal dopants are generally acting in the following ways to enhance the charge carrier separation and spectral response of TiO_2 (Fig. 7):

- Electron trap mechanism
- Surface plasmon resonance (SPR) effect
- Incorporation of new energy levels
- Generation of gap states by interaction with TiO_2 VB states

2.1. Electron traps mechanism

The electron trap mechanism is organized through the Schottky barrier formation [167,173,175]. The photo-generated electrons from the CB of TiO_2 can easily migrate to the metal *via* Schottky barrier (*i.e.* a barrier formed at the semiconductor-metal interface, Fig. 8) [26] and the metal can as an electron sink.

Table 1

A summary of the key findings of metal-doped TiO_2 photocatalysts reported in the recent years for H_2 production.

Photocatalyst	Dopant concentration	Light Source	H_2 production efficiency	Quantum efficiency	Reference
Ag/TiO$_2$	–	UV and visible	1.34 µmol cm^{-2} h^{-1}	–	[129]
W-TiO$_2$/Au hybrid	Au-1.93 wt % W- 0.83 wt %	300 W Xe	24000 µmol h^{-1} g^{-1}	–	[62]
Au-Pt/Ti^{3+} io-TiO$_2$	–	200 W Hg/Xe with 1.5 A M filter	181770 µmol h^{-1} g^{-1}	–	[130]
Ni/TiO$_2$	1 wt %	UV (450 W Hg)	3390 µmol h^{-1} g^{-1}	2.8 %	[131]
Fe/Ni-TiO$_2$	Fe- 5 wt % Ni- 4 wt %	UV and visible light	361.64 µmol h^{-1} g^{-1}	–	[132]
Fe/TiO$_2$	1.1 wt %	Visible light (250 W tungsten halogen lamp)	15.5 µmol h^{-1}	–	[133]
Pt/TiO$_2$	1 wt %	AM 1.5 G solar simulator	11200 µmol h^{-1} g^{-1}	–	[134]
N–TiO$_2$/ Pt	–	300 W Xe	300 µmol h^{-1}	–	[67]
N–TiO$_2$/ Pt	Pt- 0.2 wt %	500 W Xe	570 µmol h^{-1} g^{-1}	–	[135]
N/Pt-TiO$_2$	4.6 wt %	Visible light	11.34 µmol h^{-1}	–	[68]
Ni/N-TiO$_2$	Ni – 10 µmol	400 W Hg	490 µmol h^{-1} g^{-1}	–	[136]
N-TiO$_2$	–	UV and visible (500 W Xe)	6.0 µmol h^{-1}	–	[137]
S- TiO$_2$	–	AM 1.5 solar simulator	163.9 µmol h^{-1} g^{-1}	–	[138]
F-TiO$_2$	6.9 wt %	300 W Xe	18270 µmol h^{-1} g^{-1}	21.6 %	[139]
Fe-Ni/Ag/TiO$_2$	–	500 W Xe	793.86 µmol h^{-1} g^{-1}	0.25 %	[140]
Cu/TiO$_2$	1 wt %	UV (450 W Hg)	8470 µmol h^{-1} g^{-1}	7.0 %	[131]
Cu/N - TiO$_2$	–	Visible light (500 W halogen lamp)	283 µmol h^{-1} g^{-1}	–	[87]
		UV (400 W medium pressure halide lamp)	27400 µmol h^{-1} g^{-1}	–	
Co-TiO$_2$	Co-1 wt %	Solar and UV (400 W Hg vapour lamp)	11,021 µmol h^{-1} g^{-1}	–	[86]
Ag/Ce-TiO$_2$	0.2 mM Ag 0.3 mM Ce	Visible light (Xe lamp with optical filter), UV (high pressure Hg lamp)	1.47 µmol /cm^2.h	–	[141]
Cu/S-TiO$_2$	Cu- 5 wt %	500 W Xe lamp with UV cut off filter	7500 µmol h^{-1} g^{-1}	–	[142]
Ga/N - TiO$_2$	Ga - 0.48 mol	125 W Hg lamp with a 400 nm cut-off filter	5.32 µmol h^{-1}	–	[143]
Pt/Ga-TiO$_2$	Ga -3.125 wt % Pt- 0.5 wt %	150 W Xe	5722 µmol h^{-1} g^{-1}	–	[144]
Gd/N-TiO$_2$	Gd – 2 wt %	150 W Xe	10764 µmol h^{-1} g^{-1}	–	[145]
Rh/Nb-TiO$_2$	Rh – 0.2 wt % Nb – 0.2 wt %	300 W Xe	7850 µmol h^{-1} g^{-1}	–	[146]
Pt-TiO$_2$	Pt- 1 wt%	–	383 mmol h^{-1} g^{-1}	7.8 %	[147]
Pt-TiO$_2$	Pt- 2.5 wt%	Near-UV light irradiation spectrum (BLB lamp)	0.117 mol H$_2$/cm^{3}h	22.6 %	[21]
Ru-TiO$_2$	Ru- 3 wt %	500 W Xe lamp With a light cut-off filter UV light: (280–400 nm)	4.7 mmol h^{-1} g^{-1}	3.1 %	[36]
		500 W Xe lamp With a light cut-off filter Visible light: (420–680 nm).	0.85 mmol h^{-1} g^{-1}	0.6 %	
Cu-mpTiO$_2$	3 wt%	Sunlight irradiation	1000 µmol h^{-1} g^{-1}	11.39 %	[148]
Pt-TiO$_2$	Pt - 0.5 wt%	500 W Hg-Xe lamp with dichroic filter (280 – 400 nm)	27.6 mmol g^{-1} h^{-1}	5.6 %	[37]
TiO$_2$/Pt/rGO	Pt - 0.5 wt%	9 W 4 Philips PL-S lamp (315 - 400 nm)	2411 mmol g^{-1} h^{-5}	1.41 %	[149]
NY TiO$_2$-Pt	Pt – 0.188 wt%	Visible light and UV (PLSSXE- 300C Xe lamp)	20.88 mmol h^{-1} g^{-1}	–	[150]
Ni$_1$-Pd$_{10}$/TiO$_2$	Ni- 1 wt% Atomic ratio 1:10 (Ni : Pd)	UV- vis light (400 W mercury arc)	200 µmol h^{-1}	–	[151]
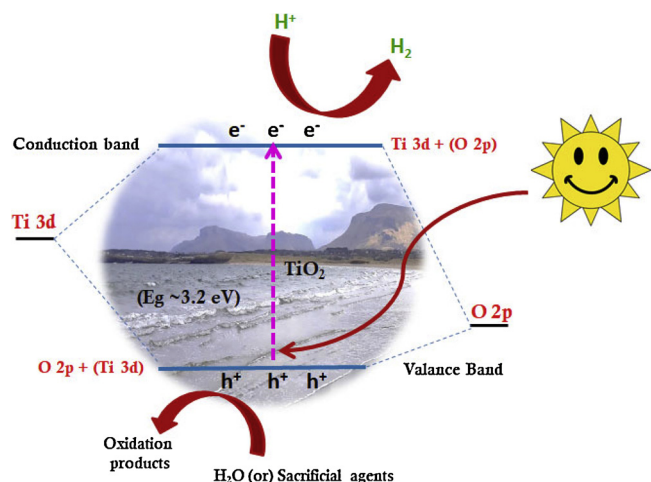
Fig. 6. Schematic illustration of H_2 formation *via* photocatalytic water splitting on the TiO$_2$ surface.

The surface band bending can occur *via* electron transfer when the semiconductor contacts with the metal [181]. Band bending is called as the shifting of energy band edges of a semiconductor due to the electric field/charge transfer between the semiconductor and the metal [182]. Electrons are generally transferred from the material with high Fermi level to that of low Fermi level until the thermodynamic equilibrium is achieved between the two (Fig. 9). Fermi level of metal is lower than the *n*-type semiconductor. Therefore, the electrons could transfer from n-type semiconductor to metal. This causes the development of an electron depletion region, suggesting the surface upward-bent band in *n*-type semiconductor. Conversely, the Fermi level of metal is higher than the *p*-type semiconductor. Hence, the electrons could transfer from metal to *p*-type semiconductor. This results the creation of hole depletion region, indicating the surface downward-bent band in *p*-type semiconductor.

V_S or built in electric field is positive for *p*-type semiconductor and it is negative for the n-type semiconductor. Consequently, the surface has an upward-bent band for *n*- type semiconductor and it has a downward-bent band for *p*-type semiconductor. The band bending also relies on the work function of metal and semiconductor. Fig. 10 shows the band bending of an *n*-type semiconductor (*i.e.* TiO$_2$) and metal with different work function. An upward-bent band occurs toward the metal-
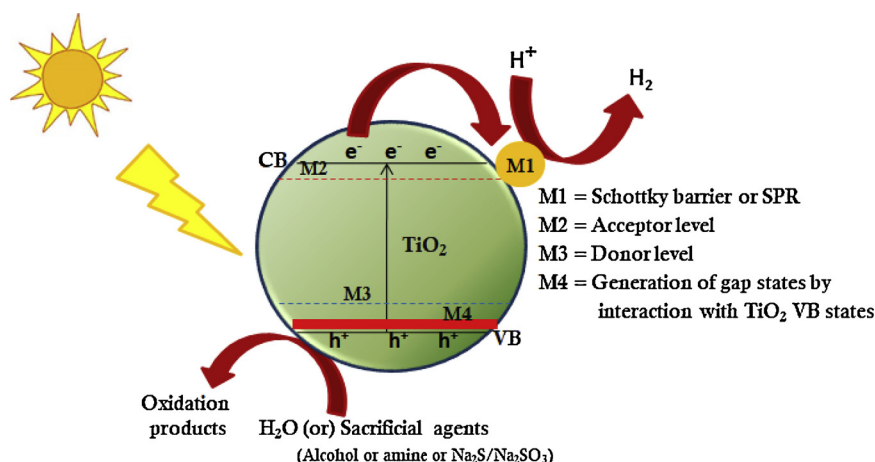
Fig. 7. The plausible mechanistic pathways of metal dopants for the enhancement of charge carrier separation and light absorption capacity of TiO_2.
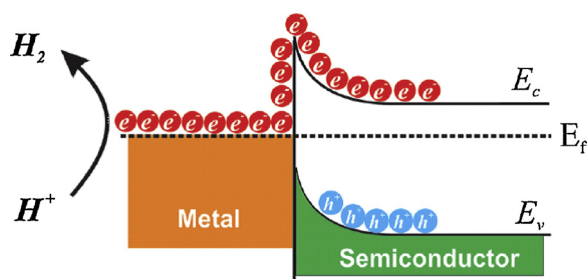

Fig. 8. Schematic representation of electron transfer *via* Schottky barrier formation [26]. Reproduced with permission from ref. [26]. Copyright (2015), Royal Society of Chemistry.
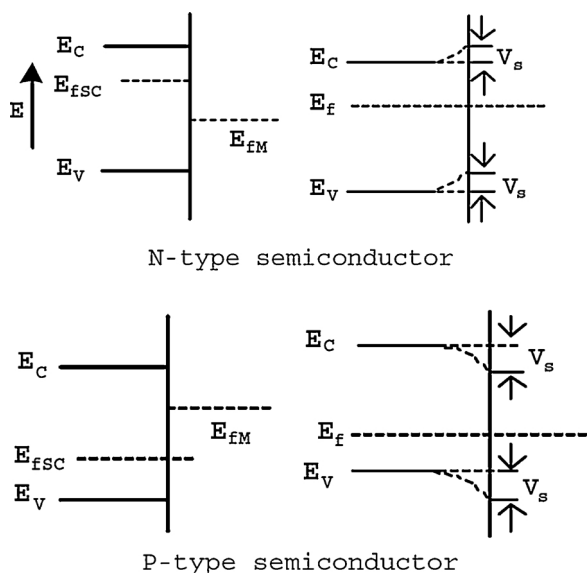

Fig. 9. Plots of surface band bending when a semiconductor contacts with the metal (E_C – energy of CB minimum; E_V- energy of VB maximum; *SC*- semiconductor; E_F- Fermi level; *M*- metal and V_S- surface barrier or built in electric field at the surface) [181]. Reproduced with permission from ref. [181]. Copyrights (2003), Elsevier.

semiconductor interface when the work function of metal is higher than that of semiconductor. Likewise, a downward-bent band occurs, as the work function of metal is lower than that of semiconductor [182].

The energetics of a metal-semiconductor system could be improved by shifting the Fermi level closer to the CB. The Fermi level shift is influenced by the degree of electron accumulation and the particle size of the metal nanoparticles [183,184]. Subramanian et al. [183] studied the Fermi level shift of TiO_2/Au nanocomposites. The experiments were carried out with Au of different particle sizes. The Fermi level of a semiconductor is calculated by the following equation [183]:

$$E_F = E_{CB} + kT \ln n_c/N_c \qquad (18)$$

Where n_c is the accumulated electrons density and Nc is the charge carrier density of the semiconductor. The Fermi level of TiO_2 is shifted to a more negative position if more electrons are accumulated in the TiO_2/Au nanocomposites. Fermi levels values were found to be $-230\,mV$, -250, -270, and $-290\,mV$ for pure TiO_2, TiO_2/Au (8 nm), TiO_2/Au (5 nm), and TiO_2/Au (3 nm), respectively. The negative shift of Fermi level is an indication of high degree of electron accumulation, which also suggests a high charge carrier separation and reductive power of TiO_2/Au nanocomposites [183,184].

Fermi level shift also depends on the metal work function, which is more significant in facilitation of the electron transfer from metal to H^+ to produce H_2. Generally, a metal with a high work function is preferable to achieve maximum charge carrier separation. When the work function of a metal is higher than that of TiO_2, the Schottky barrier can be formed between CB of TiO_2 and fermi level of the metal. In this case, the injected electrons are unable to flow back to TiO_2. The work function of Ag, Cu, Rh, Au, Pd, and Pt are 4.26, 4.65, 4.98, 5.10, 5.60, and 5.93, respectively [177]. Owing to its high work function, Pt can serve as an effective electron trap to suppress the charge-carrier recombination process.

A schematic representation of the charge carrier separation and transfer *via* Schottky junction using Pt/TiO_2 photocatalyst is shown in Fig. 11 [185]. When Pt and TiO_2 are in direct contact with each other, the electrons are diffused from TiO_2 to Pt to create an equilibrium state between fermi level of TiO_2 ($E_f TiO_2$) and Pt ($E_f Pt$). This charge diffusion process would create an internal electric field and cause upward band bending (from TiO_2 to Pt). Therefore, the Schottky barrier is established between the TiO_2 CB and $E_f Pt$. Consequently, the electron-hole recombination process is minimized and the H_2 production efficiency is increased.

The surface of TiO_2 is not an active site for atomic hydrogen ($H^•$) absorption, leading to H_2 production. The metal can also function as an active catalyst site to reduce the over-potential of H_2 evolution. In the recent years, most of the water splitting research studies have been carried out using Pt (Fig. 12) or Au (Fig. 13) as a co-catalyst or metal dopant [186–191].
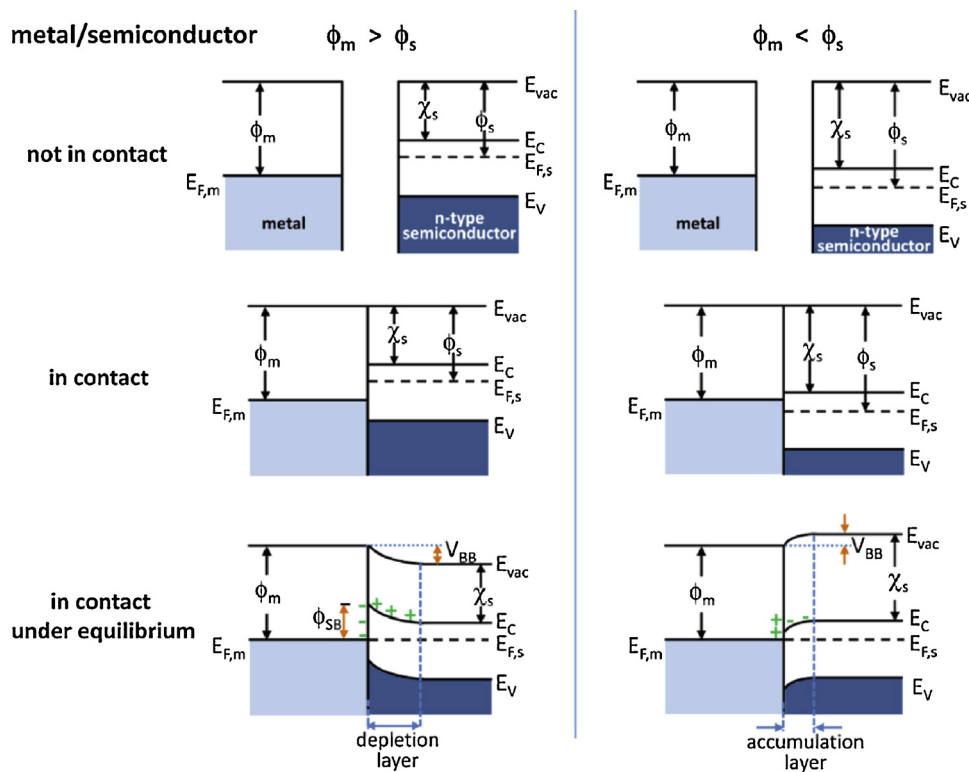
metal/semiconductor

2.2. SPR effect

Surface plasmons are the collective oscillations of free electrons confined to a surface in a conducting material [196]. It can interact strongly with light. SPR occurs when the frequency of incident light is equal to that of surface free electrons oscillating against the restoring force of the nuclei. The photonic energy can be transferred into thermal or electronic energy *via* radiative (converting plasmons into photons) and non-radiative decay (creates electron-hole excitation) of surface plasmons. The frequency of the SPR can be modified by the size, morphology, proximity and nature of the metal nanoparticles. An intense local electric field (called as "hot spot") is created near the metal surface when the metal nanoparticles are irradiated near its plasmon resonance frequency. The electron-hole generation rate in the hot spot region is 1000 times higher than the incident electromagnetic field. Consequently, a higher amount of photo-induced charge carriers is generated locally in TiO_2 by the plasmonic metal nanoparticles [197,198].

The relationship between the spectroscopy and dynamics of metal nanoparticles for plasmon induced photocatalysis was comprehensively described a recent study [199]. The results showed that the hot electron (high energy electron) generation and coupling of plasmon-molecular interactions are controlled by the nature of the material and shape of the nanocrystal. The relaxation process in metal nanoparticles and its influence in the photocatalytic process were reviewed in detail. Two mechanisms such as (i) a sequential excitation − charge-transfer and (ii) direct excitation of an interfacial charge-transfer were used to explain the charge transfer mechanism from a metal to the semiconductor in a plasmon induced photocatalytic process. An efficient photocatalysis process is generally occurred *via* the direct excitation of interfacial charge-transfer transitions, which can be studied by perceiving how localized surface plasmon resonance (LSPR) line width varies in the presence of surface bound molecules. Rayleigh light-scattering and elegant single-particle absorption techniques could be used to measure the LSPR line width.

The total LSPR line width (Γ) can be written as follows:
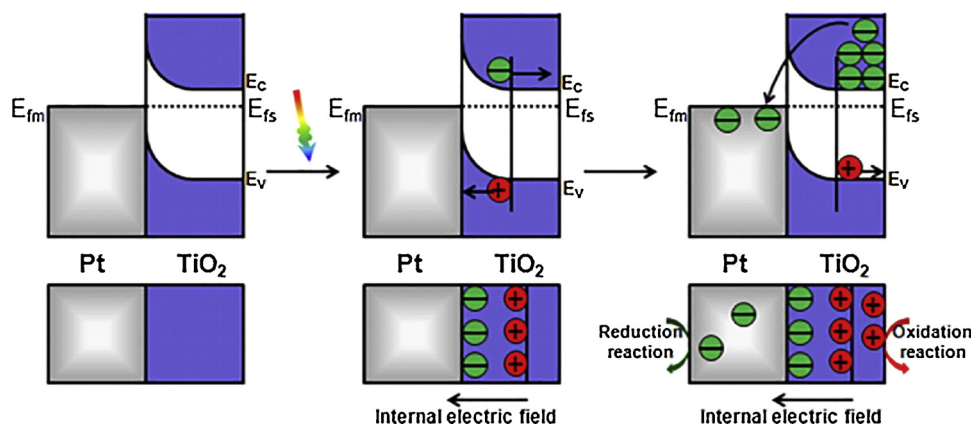
Fig. 11. Schematic representation of the charge carrier separation and transfer *via* Schottky junction using Pt/TiO_2 photocatalyst [185]. Reproduced with permission from ref. [185]. Copyright (2018), Elsevier.
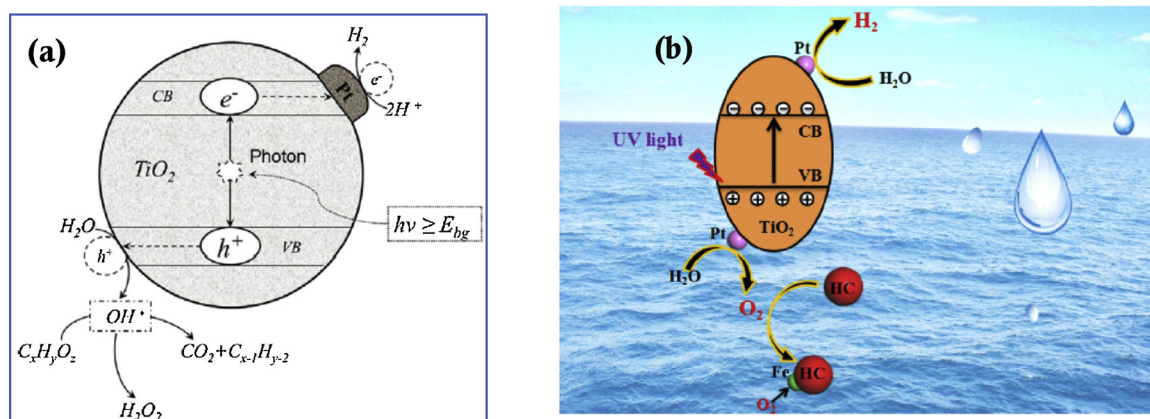
Fig. 12. Schematic illustration of electron hole separation on Pt doped TiO_2 [192,193]. Reproduced with permission from ref. [192,193]. Copyright (2017, 2016). Elsevier.

$$\Gamma = \Gamma_b + \Gamma_{rad} + \Gamma_{surf} = \Gamma_b + 2\,\hbar kV + A\,(v_F/l_{eff}) \qquad (19)$$

Where Γ_b denotes the direct bulk-like decay of LSPR into electronic and phononic excitations; Γ_{rad} describes the radiation damping (energy loss through scattering a photon); Γ_{surf} represents the damping by electron surface collisions; $\hbar$, k and A are the constants; V is the volume; v_F is the Fermi velocity; l_{eff} is the effective path length of electrons.

Γ_b has contributions from the inter-band and intra-band ("Drude model") transitions

$$\Gamma_b = \Gamma_{Drude} + \Gamma_{interband} \qquad (20)$$

The key findings of this study are: hot electrons and holes are created through the quantum optical transitions near the surfaces; particles with small size can produce highly excited electrons (essential for photocatalysis *via* sequential mechanism) in large amounts; hot electron generation requires two major components (intensification of the magnitude of electric field in the hot spot and breaking of linear momentum of electron in the hot spot); and chemical interface damping could facilitate the establishment of productive plasmon-enhanced molecular photocatalysis reactions.

Commonly, Ag, Au and Cu are used as dopants to induce the SPR effect. It is probably organized through two mechanisms, direct electron transfer (DET) and resonance energy transfer (RET) from metal to TiO_2 [200]. If the photocatalyst is a physical mixture or the metal and TiO_2 are not in direct contact with each other, RET mechanism occurs. DET mechanism takes place when the metal and TiO_2 are in direct contact with each other. For example, the life-time of plasmon excited electrons on Au can be extended up to 1.5 ns *via* DET from Au to TiO_2 when Au and TiO_2 are in direct contact with each other [201]. Upon visible light irradiation, the electrons are photo-excited in Au or Ag *via* SPR absorption. The energetic electrons are then easily migrated from Au to TiO_2. The electron transfer process from TiO_2 to metal, or metal to TiO_2, relies on the nature of light irradiation source. For example, the following electron transfer mechanisms are possible for Au-TiO_2 under different light sources: TiO_2 to Au (UV light); Au to TiO_2 (visible light); Both, TiO_2 to Au and Au to TiO_2 (UV–vis light) [177].

To validate this, the H_2 production efficiency of mesoporous Au-TiO_2 was evaluated under visible/UV–vis light irradiation [201]. The photocatalyst was synthesized in the presence of a co-polymer to induce crystal defects or impurities in TiO_2. The proposed photocatalytic mechanism of mesoporous Au-TiO_2 is shown in Fig. 14(a). The results revealed that the H_2 production efficiency of Pt-TiO_2 (300.63 µmol h^{-1} g^{-1}) was much higher than Au-TiO_2 (57.02 µmol h^{-1} g^{-1}) under UV–vis light irradiation. The high efficiency of Pt-TiO_2 is ascribed to the low over-potential and high work function of Pt as compared to Au. TiO_2 can be easily excited by UV light and the photo-excited electrons are migrated from the CB to Pt or Au. Therefore, the charge carrier separation process and H_2 production rate are enhanced on the catalyst surface. Nevertheless, the efficiencies of Au-TiO_2 (7 µmol h^{-1} g^{-1}) and Pt-TiO_2 (2.3 µmol h^{-1} g^{-1}) were reversed under visible light irradiation
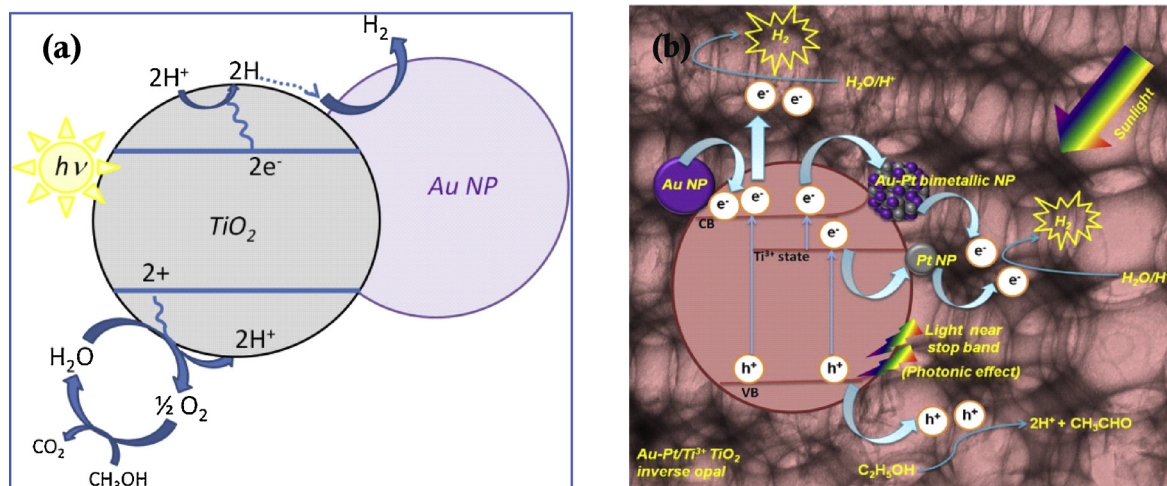

Fig. 13. Schematic illustration of electron hole separation on Au doped TiO_2 [194,195]. Reproduced with permission from ref. [194]. Copyright (2017), Elsevier. Reproduced with permission from ref. [195]. Copyright (2018), American Chemical Society.
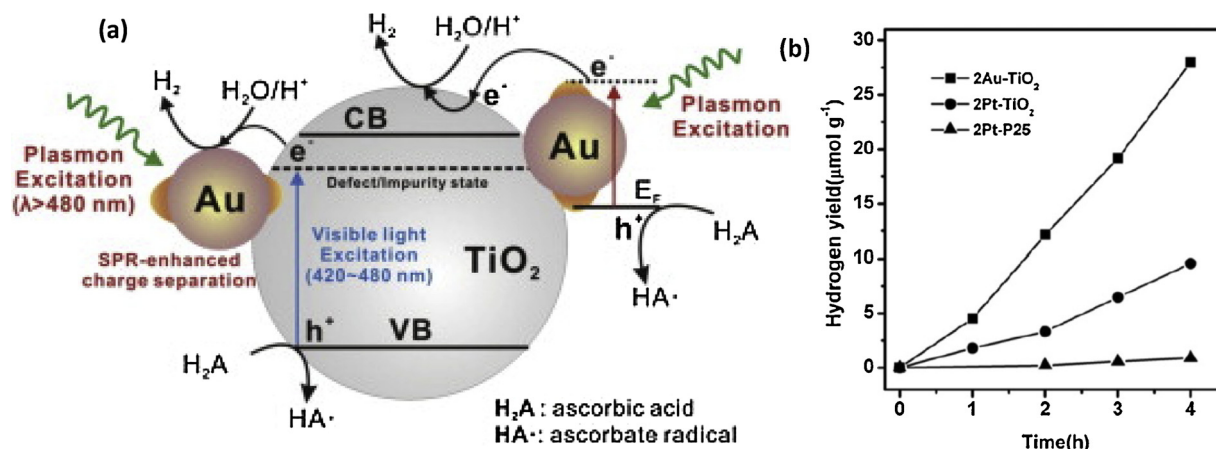
Fig. 14. (a) A proposed photocatalytic mechanism of meso-porous Au-TiO$_2$ under UV–vis light (b) H$_2$ production efficiencies of TiO$_2$, Pt-TiO$_2$ and Au-TiO$_2$ under visible light irradiation [201]. Reproduced with permission from ref. [201]. Copyright (2012), Elsevier.

($\lambda > 420$ nm) (Fig. 14 (b)). The efficiency of Au-TiO$_2$ is nearly three times higher than that of Pt-TiO$_2$. This might be attributed to the following reasons: enrichment of visible light excitation of TiO$_2$ by the strong localized electric field *via* the plasmon excitation of Au; the transfer of more energetic electrons from the plasmon-excited Au to TiO$_2$ [202].

In another study, it was found that the H$_2$ yield of Ag-TiO$_2$ (8.1 µmol cm^{-2}) under UV–vis light irradiation was higher than the sum of H$_2$ yield of Ag-TiO$_2$ (5.8 µmol cm^{-2}) under separate UV (4.2 µmol cm^{-2}) and visible light (3.9 µmol cm^{-2}) irradiation [203]. H$_2$ yield of Ag-TiO$_2$ under UV light irradiation was almost doubled when the visible light was added. The enhancement in efficiency is attributed to the synergistic effect of Schottky barrier formation and SPR. Upon UV light irradiation, a Schottky barrier is formed between Ag and TiO$_2$ to promote the migration of photo-excited electrons from TiO$_2$ and Ag. Concurrently, SPR effect is introduced by the visible light, indicating the photo-excitation of electrons in Ag. A strong local electric field is also formed to enhance the energy of trapped electrons, suggesting the electron transfer and photo-reduction process (H$^+$ to H$_2$) occurs more easily.

Most of the previous studies suggest the importance of Cu reduced states for the photocatalytic activity. Recently, MuÇoz-Batista et al. [38] studied the phase-contact engineering in mono and bimetallic non-noble metal co-catalysts (Cu-Ni) for photocatalytic H$_2$ production using TiO$_2$. They examined the variations in oxidation state, size and structure of the photocatalyst under operando conditions (measurements under working conditions). The new perspectives (light-matter interaction) of mono and bimetallic photocatalysts were unveiled by a combination of micro X-ray absorption near edge structure (XANES) and extended X-ray absorption fine structure (EXAFS) studies at appropriate X-ray beam/light probe length (Fig. 15). The results testified that Cu showed a high response as compared Ni in the bimetallic photocatalyst under operando conditions. Moreover, the photocatalytic activity was facilitated by a core shell structure of Cu (Cu0 in the core and Cu^{II} in the outer surface (Fig. 15)).The electron handling property was enabled by Cu0 and the surface chemical role was facilitated by the oxidized Cu phase. The photocatalytic efficiency was further improved by the secondary chemical role of Ni in the bimetallic catalysts. XANES and EXAFS studies revealed that Cu0 is finely dispersed in the copper oxide matrix. Ni played a key role to shape the phase contact between the Cu rich phases and to govern the electronic or structural properties of Cu phases.

Like noble metals, transition metal nitrides (TMN's) such as titanium nitride and zirconium nitride nanomaterials have also been recently used as plasmonic materials for photocatalytic applications [204,205]. The optical properties of TMN are almost similar to that of noble metals. The plasmon resonance, stability (chemical and thermal), durability, and corrosion resistance of TMN are higher than that of noble metals [206–208]. TMN nanomaterials can inject more hot electrons into the CB of TiO$_2$ as compared to Au nanoparticles. The cost of TMN are significantly cheaper when compared to Au or Pt nanoparticles. Naldoni et al. [204] reported the broadband hot-electron collection for solar water splitting using plasmonic TiN. The photocurrent response of TiO$_2$/titanium nitride system is higher than that of TiO$_2$/Au system for water splitting. This is ascribed to the following reasons: titanium nitride nanoparticles offer a broadband absorption over the wavelength range 500 nm–1200 nm and titanium nitride creates an Ohmic junction with TiO$_2$ to facilitate the electron collection. This kind of Ohmic junction is beneficial for high conversion efficiencies through "downhill" hot electron collection into TiO$_2$.

2.3. Incorporation of new energy levels

The charge carrier recombination process is suppressed by the metal dopants *via* introducing new energy levels in TiO$_2$. Doping of metal cations can generate donor (above the VB of TiO$_2$) or acceptor (below the CB of TiO$_2$) energy levels (Fig. 16) levels [209]. Cation doping also influences the crystallinity and creates crystal defects in TiO$_2$.

Non-metal or anion doping (*e.g.* I, N, C, F) is commonly employed to increase the photocatalytic activity of TiO$_2$ under visible light [102,210–213]. It is predicted that non-metal doping is more beneficial than metal doping, because it will avoid the formation of charge carrier recombination centers when compared to cation doping [209]. In most of the recent studies, N was used as a non-metal dopant to improve the water splitting efficiency of TiO$_2$ [145,214–216]. The bandgap energy of TiO$_2$ is narrowed through the generation of gap states by the interaction of N *2p* and O *2p* states [217]. The mixing up of orbitals uplifts the VB level of TiO$_2$ while the CB remains unaffected (Fig. 17). Consequently, the photo-reduction ability of TiO$_2$ is unchanged; however, its oxidation capability is decreased.

Co-doping (metal/metal [40,218] or metal/non-metal [97,219]) of TiO$_2$ with two metals is also a promising way to narrow the bandgap energy, suppress the charge carrier recombination and maintain the charge balance. The photocatalytic mechanism of metal doped TiO$_2$ from some of the recent research studies are highlighted briefly in the following section. We also identified that most of the recent water splitting studies have been performed with bimetallic dopants.

The impact of Cu oxidation species on the H$_2$ production efficiency of TiO$_2$ was evaluated under UV–vis light irradiation [220]. It was found that the proportion of Cu/Cu$_2$O/CuO species was mainly influenced by the differences in calcination temperature, time and atmosphere during synthesis. Cu/TiO$_2$ was synthesized by impregnation
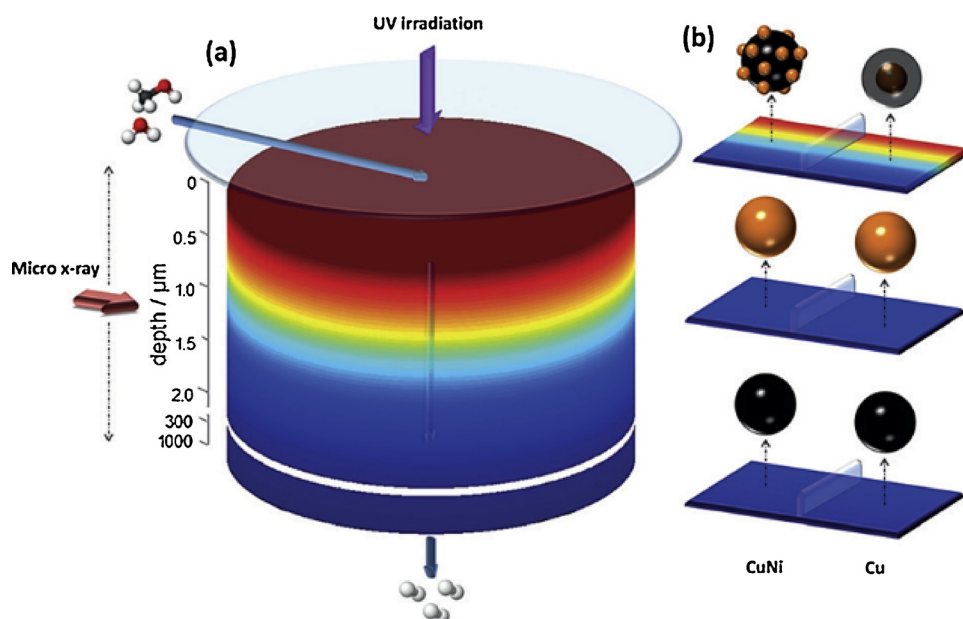
Fig. 15. (a) Schematic view of the samples (mono and bimetallic) at different depths of light intensity received. The sample is enclosed in a cell, which enables the simultaneous gas-phase treatment and light irradiation from the top side. X-ray micro-beam probes the chemical states and structure of metals as a function of depth from the surface (b) the most relevant Cu phases (Cu° brown colour as core, Cu^{II} black colour as outer surface) at different depths of light intensity received [38]. Reproduced with permission from ref. [38]. Copyrights (2018), John Wiley and Sons.

method. The synthesized samples were initially dried at 110 °C overnight. Then, the dried samples were calcined separately in air and hydrogen atmospheres. The samples were further calcined at 300 °C for 0.5 h. Hydrogen treated samples were synthesized by the further calcination of the air treated samples using 10% of H_2 in Ar atmosphere at 300 °C for 1 h, 2 h and 3 h. The colour of Cu/TiO_2 samples was identified as dark grey and indigo for air and hydrogen treated samples respectively. XPS results (Fig. 18(g) and (h)) revealed that Cu mainly existed in the form of CuO (Cu^{2+} state) with some Cu_2O (Cu$^+$ state) for air calcined samples, while it presented as a stable metallic copper (Cu° state) for the hydrogen treated samples.

H_2 production rate of hydrogen-treated $Cu-TiO_2$ was 2.4 times faster than that of air calcined sample. DFT calculations of TiO_2 anatase (101) slab with CuO, Cu_2O and Cu° is show in Fig. 18 (a–e). The results testified that the reduction of Cu^{2+} or Cu$^+$ is thermodynamically more favorable when compared to H$^+$ (Fig. 19(a)) reduction. Based on the experimental and DFT results, two different charge transfer mechanisms were proposed for the photocatalytic activity of CuO/TiO_2 (Fig. 19 (b)) and $Cu°/TiO_2$ samples (Fig. 19 (c)). For CuO/TiO_2 samples, H_2 is produced through the following steps: (i) At first, CuO is reduced to Cu_2O using photo-generated electrons. This is further supported by an initial lag in H_2 production efficiency from the reaction mixture. The samples were also analysed by XPS after the photo-reaction to confirm the oxidation states. The further reduction of Cu_2O to Cu0 is
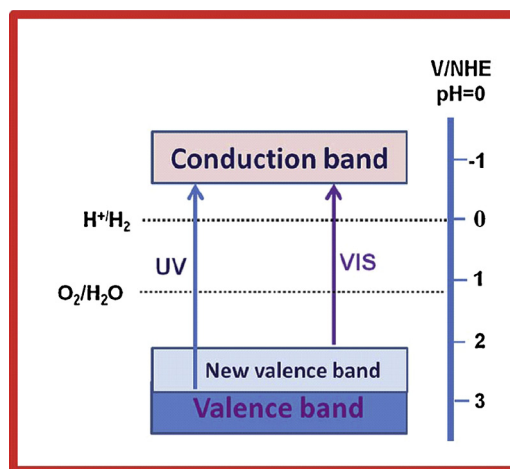
Fig. 17. Schematic representation of the generation of gap states by non-metal doping [209]. Reproduced with permission from ref. [209]. Copyright (2015), Royal Chemical Society.
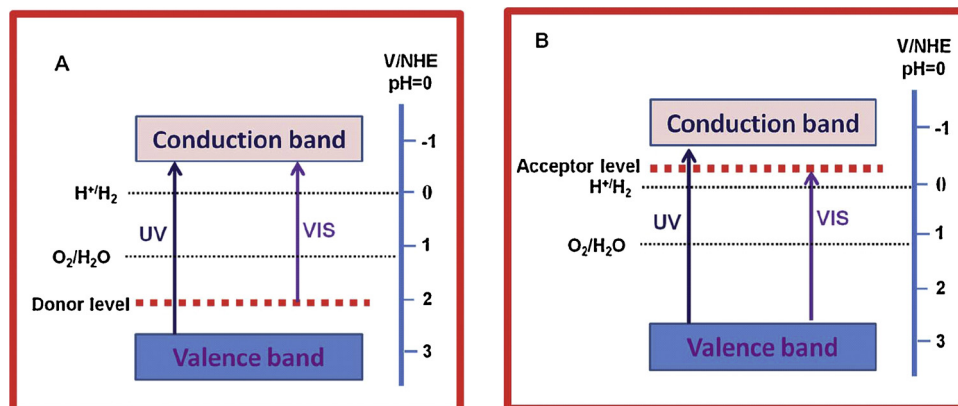
Fig. 16. Schematic representation of (a) Donor and (b) Acceptor energy level formation by metal cation doping [209]. Reproduced with permission from ref. [209]. Copyright (2015), Royal Chemical Society.
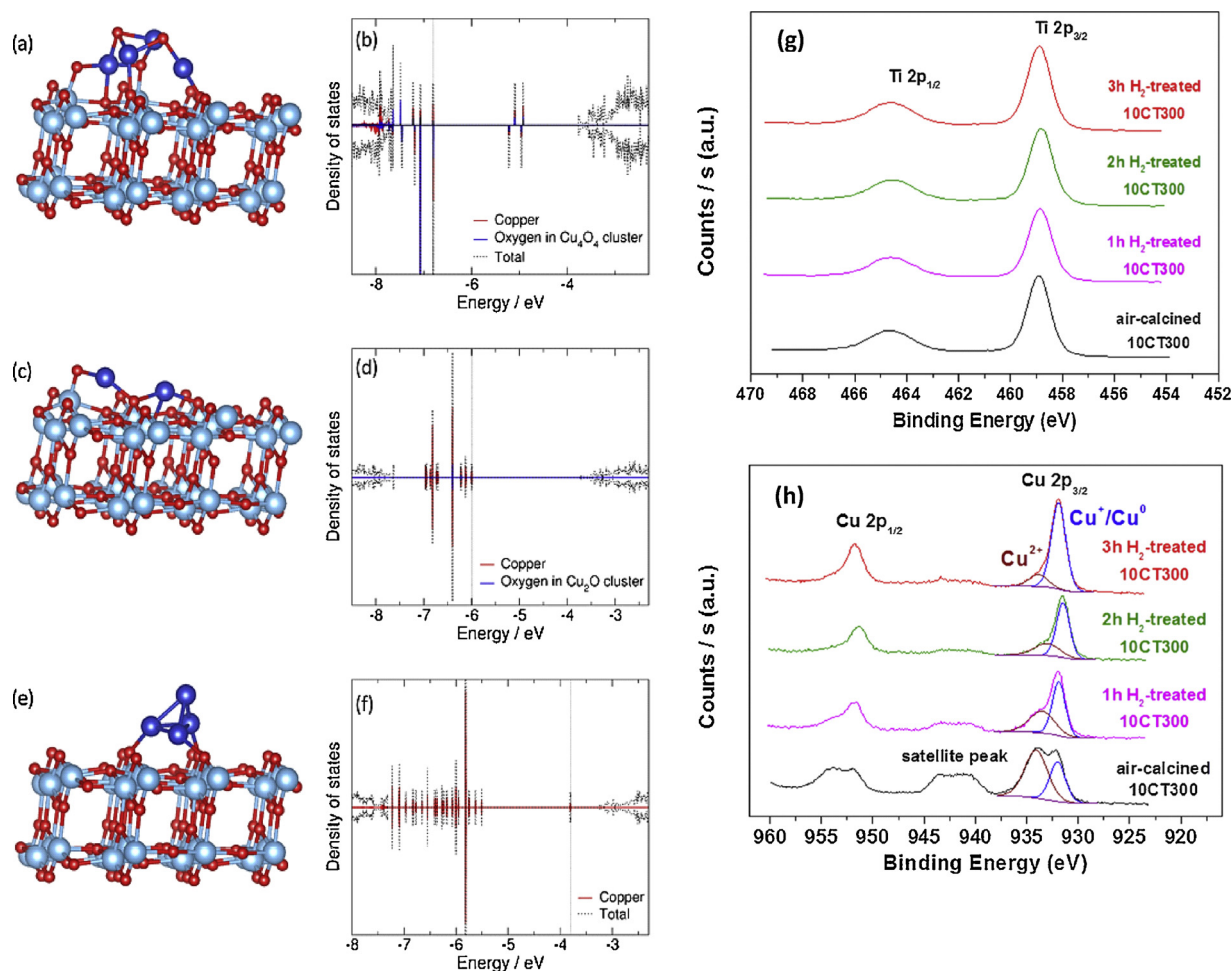
Fig. 18. TiO_2 slab models (Ti, O and Cu atoms are indicated by light blue, red and dark blue spheres, respectively) used for DFT calculations and the total and projected electron density of states in the energy region of the bandgap for CuO/TiO_2 ((a) and (b)), Cu_2O/TiO_2 ((c) and (d)) and Cu/TiO_2 ((e) and (f)). Ti 2p (g) and Cu 2p (h) core level XPS spectra of air and hydrogen treated Cu/TiO_2 samples [220]. Reproduced with permission from ref. [220]. Copyright (2016), Elsevier. (For interpretation of the references to colour in this figure legend, the reader is referred to the web version of this article).

considerably restricted by the band alignment of Cu_2O and TiO_2 (ii) Cu_2O itself could act as a semiconductor and therefore electron-hole pairs are produced on both TiO_2 and Cu_2O (iii) Because of the band alignment, the electrons are quickly migrated from the CB of Cu_2O into that of TiO_2 [221,222]; (iv) H_2 is produced by the electrons accumulated on the TiO_2 surface. For hydrogen treated samples, $Cu0$ acts as a co-catalyst like Pt [223]. DFT results revealed that a continuum of $Cu0$ states is formed within the TiO_2 bandgap. The photo-generated electrons from TiO_2 were easily attracted and collected on the surface of $Cu0$ to reduce H^+. Visible light-driven photocatalytic activity was also evaluated for CuO/TiO_2, Cu_2O/TiO_2 (CuO/TiO_2 after 0.5 h of UV light treatment) and $Cu0/TiO_2$ samples. There was no H_2 production from CuO/TiO_2, indicating the photo-generated electrons from TiO_2 are essential to reduce Cu^{2+} and display the photocatalytic activity. However, remarkable H_2 production efficiencies are exhibited by Cu_2O/TiO_2 and $Cu0/TiO_2$ after prolonged irradiation. The efficiency of Cu_2O/TiO_2 is ascribed to the band alignment of Cu_2O and TiO_2 for the effective charge separation. The efficiency of $Cu0/TiO_2$ is attributed to SPR effect of $Cu0$ [224].

In a similar study [225], H_2 production efficiency of bimetallic Cu-Pt TiO_2 was evaluated in glycerol –water mixture under UV–vis light irradiation. H_2 production rates were found to be in the following order: $Cu-Pt/TiO_2 > Pt/TiO_2 > Cu-Pt/TiO_2 >$ neat TiO_2. Experimental and DFT calculations revealed that the photo-reduction of $CuOx$–PtO_2 into metallic Cu and Pt deposits is thermodynamically more favorable when

compared to H^+ reduction. The schematic representation of charge transfer process in Cu-Pt/TiO_2 is shown in Fig. 20. H_2 is produced by the following three steps: (i) at first $CuOx$ and PtO_2 are initially reduced into Cu^0 and Pt^0, respectively by the photo-generated electrons. (ii) Electrons are then easily migrated from the CB of TiO_2 to the bimetallic surface (Cu-Pt). The suppression of electron-hole recombination is testified by the PL measurements of the photo-irradiated samples (Fig. 20 (d)) (iii) H^+ is reduced into H_2 on the Cu-Pt surface. The superior efficiency of Cu-Pt/TiO_2 is ascribed to high electron density on the bimetallic particles (by the interaction of Cu and Pt) when compared to the single metal (Cu or Pt) doped TiO_2. This was further evidenced by XPS, PL, Mulliken charges and DFT calculations.

Clarizia et al. [226] also suggested that $Cu°$ could absorb visible light and enhance the H_2 production efficiency of TiO_2 through SPR effect. H_2 production experiments were carried out by *in situ* photo-deposited $Cu°/TiO_2$ under UV–vis light irradiation. The photocatalytic activity was evaluated in the presence of different sacrificial agents such as methanol, ethanol, ethylene glycol, formic acid, glycerol, glucose, isopropyl alcohol and benzyl alcohol. Among them, glycerol showed the best performance. The plausible mechanism of electron-hole separation in Cu^0/TiO_2 is shown in Fig. 21 (a). During light irradiation, Cu^{2+} and Cu^+ were reduced first into metallic copper (Cu^0). This was further confirmed by XRD analysis of the Cu/TiO_2 after the photocatalysis reaction (Fig. 21 (b)). It was stated that both Cu^0 and TiO_2 are easily photo-excited under UV–vis light irradiation. The photo-
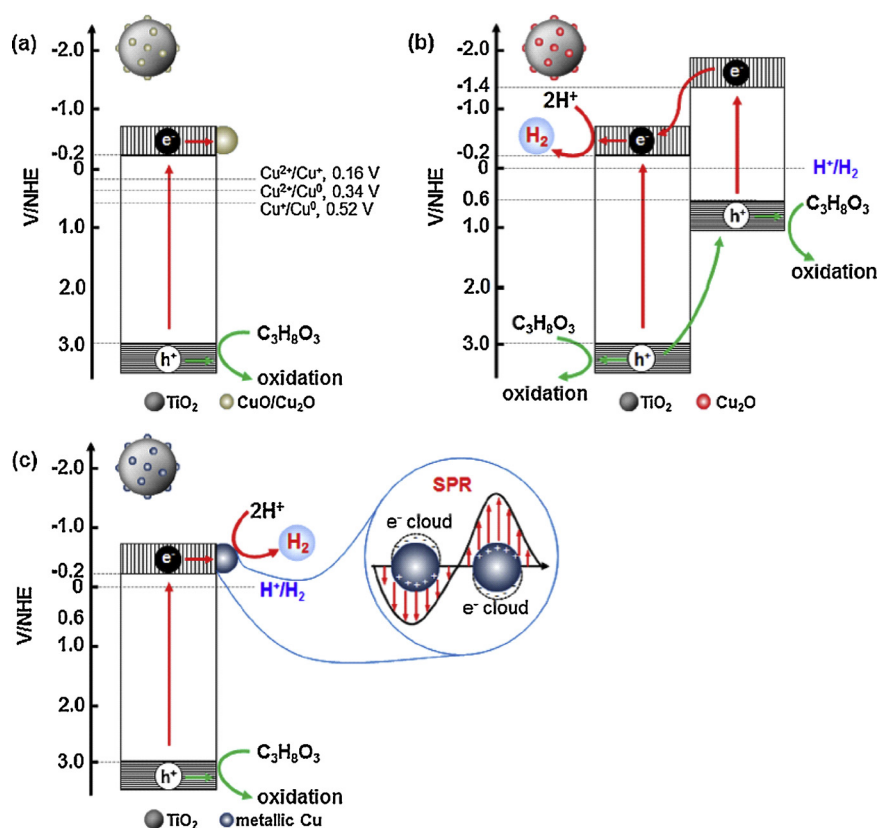
Fig. 19. The proposed photocatalytic mechanism of (a) The redox potentials of Cu species on the air calcined Cu/TiO₂ under UV–vis light (b) H₂ formation from Cu₂O/TiO₂ under UV–vis light (c) H₂ formation from Cu°/TiO₂ under visible light irradiation [220]. Reproduced with permission from ref. [220]. Copyright (2016), Elsevier.
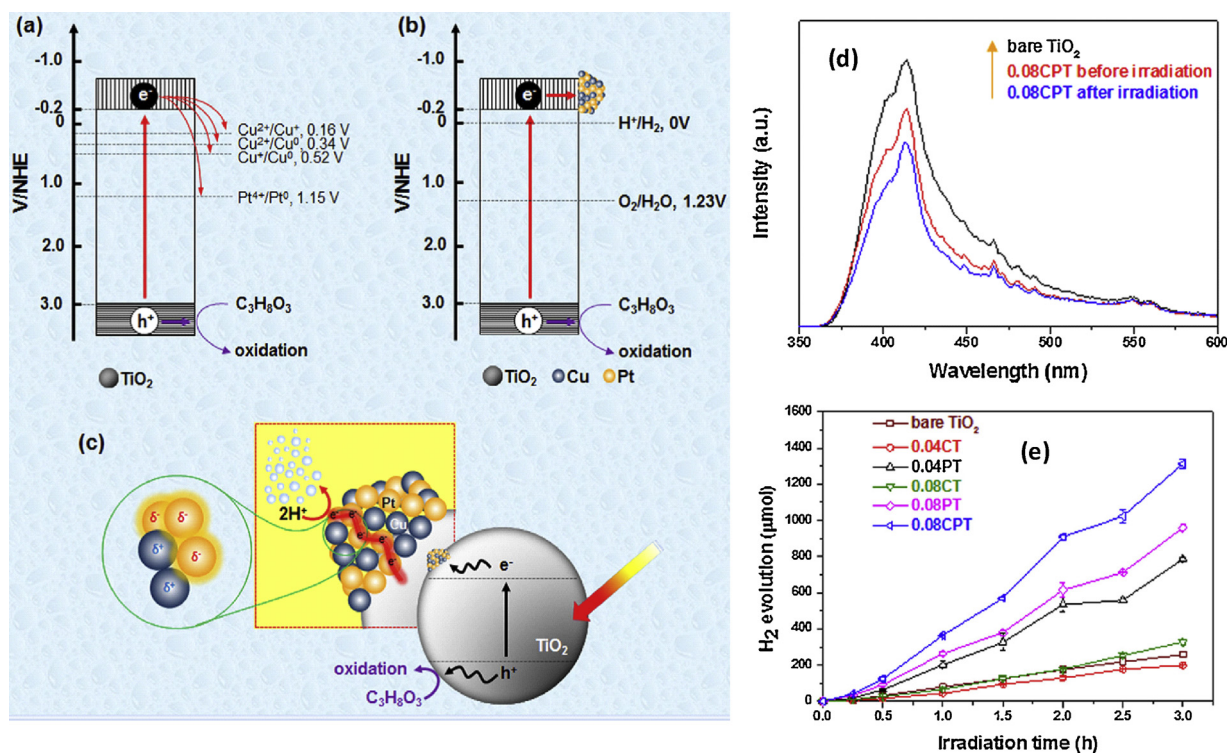
Fig. 20. The proposed charge transfer photocatalytic mechanism of (a) Energy diagram and redox potentials of Cu and Pt on CuOₓ-PtO₂/TiO₂ under light irradiation (b) Formation of bimetallic Cu-Pt/TiO₂ by the photo-generated electrons (c) H₂ evaluation form Cu-Pt/TiO₂ (d) PL spectra of Cu-Pt/TiO₂ before and after photocatalysis experiments (e) H₂ production efficiencies of pure TiO₂ and Cu-Pt/TiO₂ [225]. Reproduced with permission from ref. [225]. Copyright (2016), Elsevier.
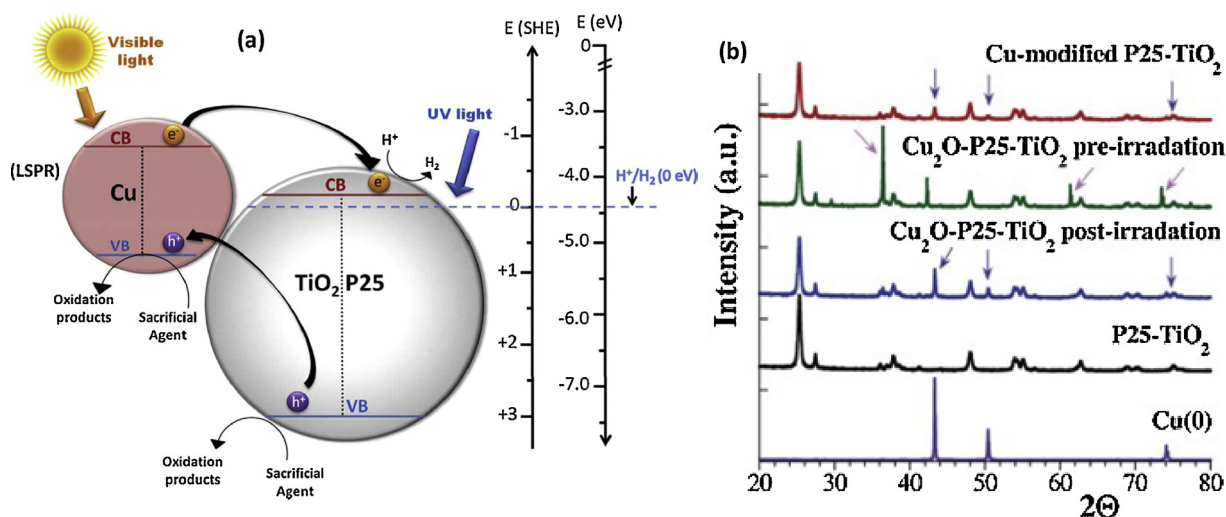
Fig. 21. (a) A plausible electron transfer mechanism of $Cu°/TiO_2$ for H_2 production under UV–vis light irradiation (b) XRD patterns of Cu/TiO_2 before and after the photo-reaction [226]. Reproduced with permission from ref. [226]. Copyright (2016), Elsevier.
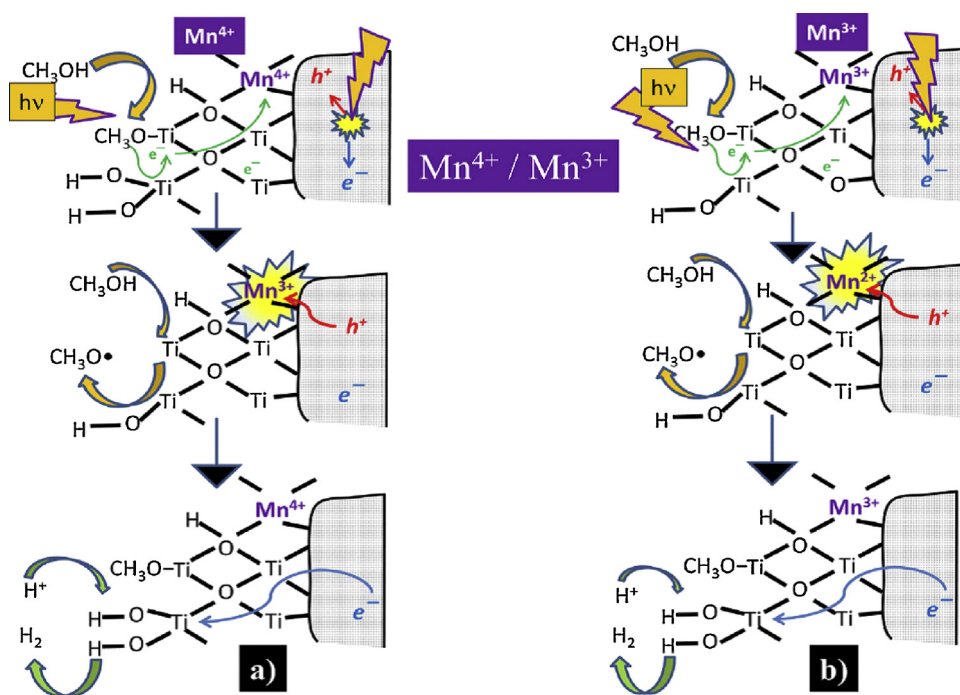
Fig. 22. A proposed electron trapping mechanism of Mn^{4+}/Mn^{3+} in TiO_2 during UV light irradiation [227]. Reproduced with permission from ref. [227]. Copyright (2016), Elsevier.

excited electrons from Cu^0 are quickly injected into the CB of TiO_2, leading to H_2 formation with H^+. Hence, the photo-generated charge carriers are highly separated on the catalyst surface.

Pérez-Larios et al. [227] evaluated the synergistic effect of Mn oxidation states on the H_2 production efficiency of TiO_2 using methanol-water system and UV light irradiation. It was found that the H_2 efficiency of 5 wt% $Mn-TiO_2$ (1736 µmol h^{-1} g^{-1}) was ~6.5 times higher than that of pristine TiO_2 (264 µmol h^{-1} g^{-1}). This is attributed to the high charge separation efficiency of Mn dopant with various oxidation states. The ionic radius of Ti^{4+}, Mn^{2+}, Mn^{3+} and Mn^{4+} are 0.68 Å, 0.80 Å, 0.66 Å and 0.60, respectively [228]. Therefore, Mn^{3+} and Mn^{4+} ions are interstitially incorporated into TiO_2. The proposed charge separation mechanism of Mn^{2+}, Mn^{3+} and Mn^{4+} doped TiO_2 is shown in Figs. 22 and 23. Mn dopant could act as an electron trap in the Mn^{4+}/Mn^{3+} oxidation state or a hole trap in Mn^{2+}/Mn^{3+} oxidation

state. The electron trap mechanism of Mn^{4+}/Mn^{3+} can be explained as follows (Fig. 22): The photo-excitation of methanol (sacrificial agent) under UV light irradiation [229,230] promotes an electron transfer from methanol to Mn^{4+} or Mn^{3+} on the catalyst surface. Hence, Mn^{4+} or Mn^{3+} ions are momentarily oxidized into Mn^{3+} or Mn^{2+} ions. The photo-generated holes from TiO_2 can induce the recovery of Mn^{4+} or Mn^{3+} ions via oxidation reaction with Mn^{3+} or Mn^{2+} [231,232]. These reactions will avoid the charge carrier recombination process and the photo-generated electrons are easily accumulated on the catalyst surface to increase H_2 production. The electron trap mechanism of Mn^{3+}/Mn^{2+} can be explained as follows (Fig. 23): It was believed that oxidation state of Mn^{3+}/Mn^{2+} ions into the TiO_2 lattice are momentarily changed into Mn^{4+}/Mn^{3+} through the reaction with photo-generated holes. In the meantime, the electrons from photo-excited methanol can induce the recovery of Mn^{3+}/Mn^{2+} ions [233,234]. Therefore, the
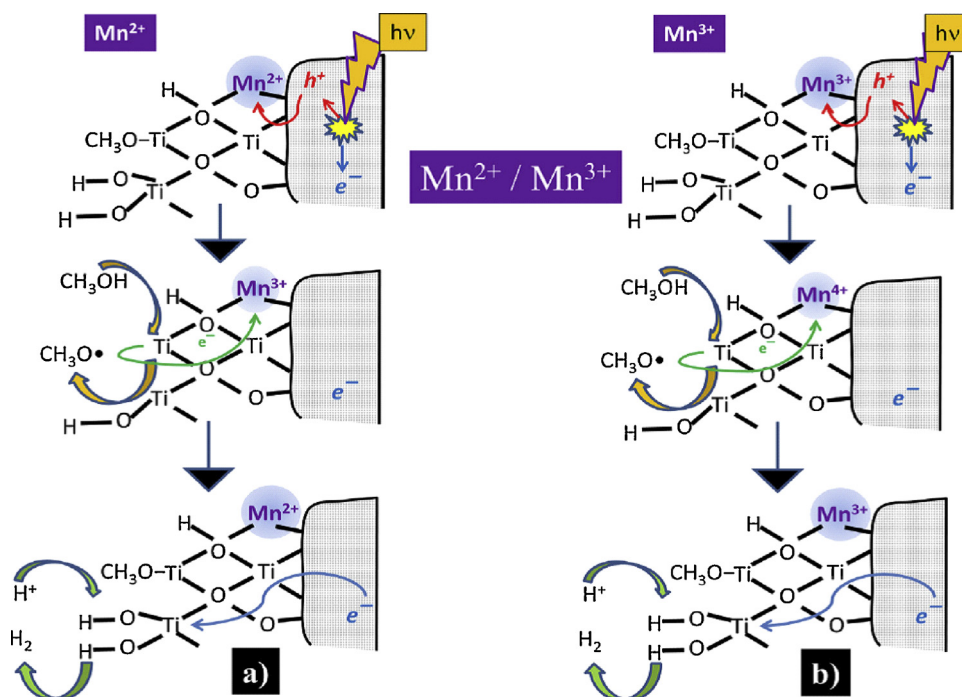
Fig. 23. A proposed hole trapping mechanism of Mn^{3+}/Mn^{2+} in TiO_2 during UV light irradiation [227]. Reproduced with permission from ref. [227]. Copyright (2016), Elsevier.

photo-generated electrons are quickly migrated to the catalyst surface to enhance H_2 formation.

The photocatalytic activity of 3D ordered macro-porous (3DOM) Fe^{3+} doped TiO_2 was studied under visible light irradiation [235]. The photocatalyst was synthesized using PMMA as a template. It should be noted that the ionic radius of Fe^{3+} (0.64 Å) and Ti^{4+} (0.68 Å) are almost identical. Therefore, some of the Ti^{4+} ions in the crystal lattice of TiO_2 can be easily substituted by Fe^{3+} ions during calcination [236,237]. They also found that the photocatalytic activity of 3DOM Fe^{3+} doped TiO_2 was higher than that of Fe^{3+} doped TiO_2 (Fig. 24 (a)).
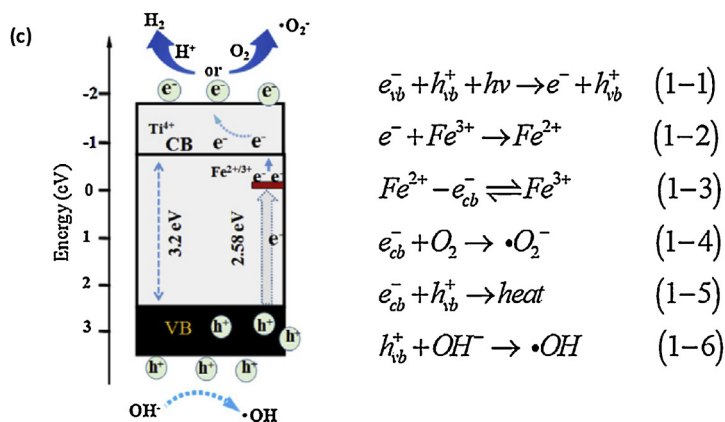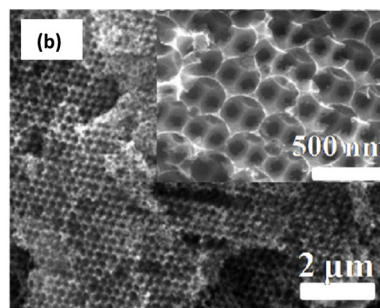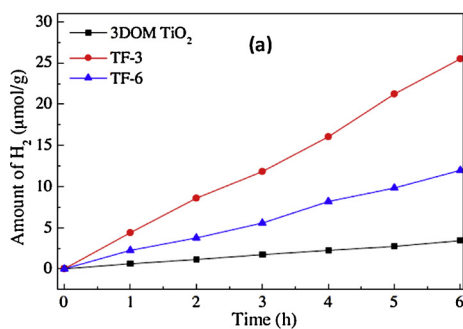
Fig. 24. (a) H_2 production efficiencies of bare and Fe^{3+} doped 3DOM TiO_2 (b) TEM image of 3DOM-Fe^{3+} doped TiO_2 (c) Schematic illustration for the photocatalysis mechanism of 3DOM Fe^{3+} doped TiO_2 under visible light irradiation [235]. Reproduced with permission from ref. [235]. Copyright (2017), Elsevier.
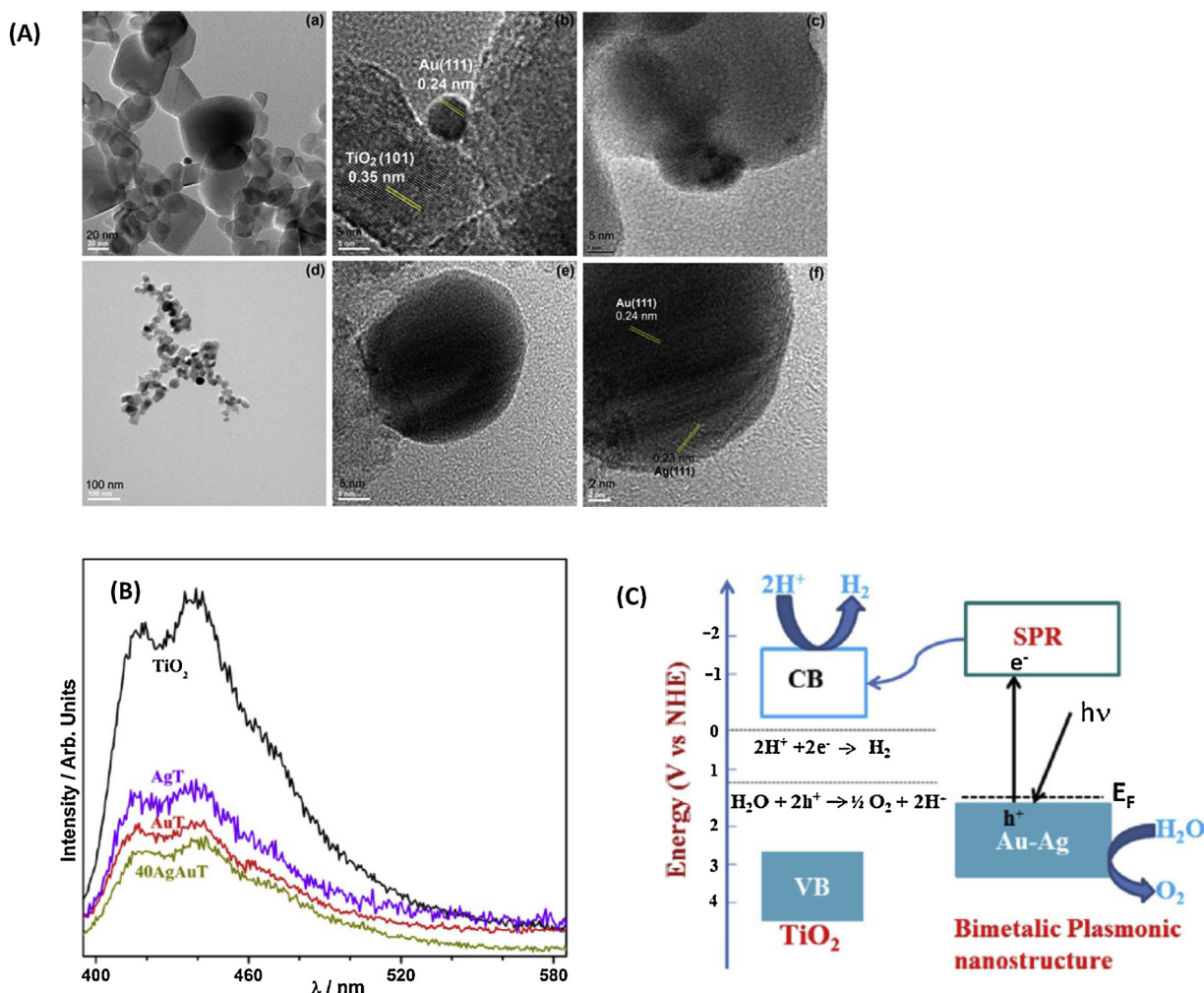
Fig. 25. (A) TEM and HR-TEM images of TiO_2 and Au-Ag-TiO_2 (B) PL spectra of TiO_2, Ag-TiO_2, Au-TiO_2, Au-Ag-TiO_2 (C) A proposed mechanism of SPR-induced electron/hole transfer for Au-Ag-TiO_2 composite [200]. Reproduced with permission from ref. [200]. Copyright (2016), John Wiley and Sons.

This is attributed to the readiness of additional optical absorption active sites for photon trapping and bandgap narrowing. The closely packed 3D morphology (Fig. 24 (b)) enhances the visible light absorption by extending the path length of light. Also, the high active surface area of 3D network can provide more interfacial active sites to simplify the mass transfer.

The electron-hole separation process is promoted by the creation of an impurity level below the CB of TiO_2 via $Fe^{3+/2+}$ doping (Fig. 24 (c)). It is believed that Fe^{3+} and Fe^{2+} ions located below the CB of TiO_2 can act as photo-generated electron acceptor ($e^- + Fe^{3+} \rightarrow Fe^{2+}$) and electron donor ($Fe^{2+} \leftrightarrow Fe^{3+} + e^-$), respectively to promote the electron-hole separation process. Fe^{2+} ions are typically not stable, and they obviously release free electrons to yield Fe^{3+} (Eq. (1)–(3), Fig. 24 (c)). The excess electrons can directly migrate into the CB of TiO_2. Therefore, the H_2 production efficiency is enhanced through the availability of more electrons and the superior electron hole separation process.

Recently, Patra et al. [200] studied the H_2 production efficiency of plasmonic Ag-Au bimetallic TiO_2 photocatalyst. Au and Ag were utilized to expand the visible light absorption through plasmonic nano-antenna (SPR effect). Moreover, both Au and Ag have similar lattice constants (2.3 Å for the Ag (111) facet and 2.4 Å for the Au (111) facet) [238]. Because of this identical lattice constant, they can easily interact with each other to form bimetallic nano-composites. HRTEM (Fig. 25 (A)) and PL (Fig. 25 (B)) results revealed that the Au-Ag and TiO_2 are in direct contact with each other, supporting the direct electron transfer

(DET) mechanism from metal to TiO_2. Ag is deposited on the surface of Au, indicating core shell morphology. Au (111) facet is determined as 0.24 nm at the center of the nanoparticle while Ag (111) facet is calculated as 0.23 nm at the edges. The low PL intensity of Ag-Au/TiO_2 is ascribed to high charge carrier separation on the photocatalyst surface through the Schottky junction.

The detailed photocatalysis mechanism is shown in Fig. 25 (C). The plasmonic metal nanoparticles are excited to its SPR state during visible light irradiation. DET occurs from the metal SPR state to the CB of TiO_2, when the energy level of CB is lower than that of metal SPR state. Moreover, the electron transfer process of Ag-Au-TiO_2 is higher as compared to Au-TiO_2 or Ag-TiO_2. The photo-reduction and oxidation reactions occurred at the CB of TiO_2 and Au-Ag surfaces, respectively.

In another study, the synergistic effect of SPR and Schottky barrier was examined using Ag-Pd/TiO_2 photocatalyst in water-ethylene glycol mixture [239]. It was found that Ag doping did not induce any colour change, however the catalysts were grey in colour after adding Pd. The electron-hole transfer process in Ag-Pd/TiO_2 is shown in Fig. 26. An increase in the electric field and electron injection into the TiO_2 are achieved via the partial overlap of SPR (Ag) with the bandgap of TiO_2. It was expected that the bimetallic nanoparticles could improve the efficiency through DET [240], RET [241] and field effect [242,243]. Among the different bimetallic compositions, only two catalysts (0.6Ag-0.4Pd/TiO_2 and 0.2Ag-0.8Pd/TiO_2) showed high efficiency. The results indicated that a balance between SPR effect (due to Ag) and Schottky barrier mechanism (due to Pd) are required to achieve maximum
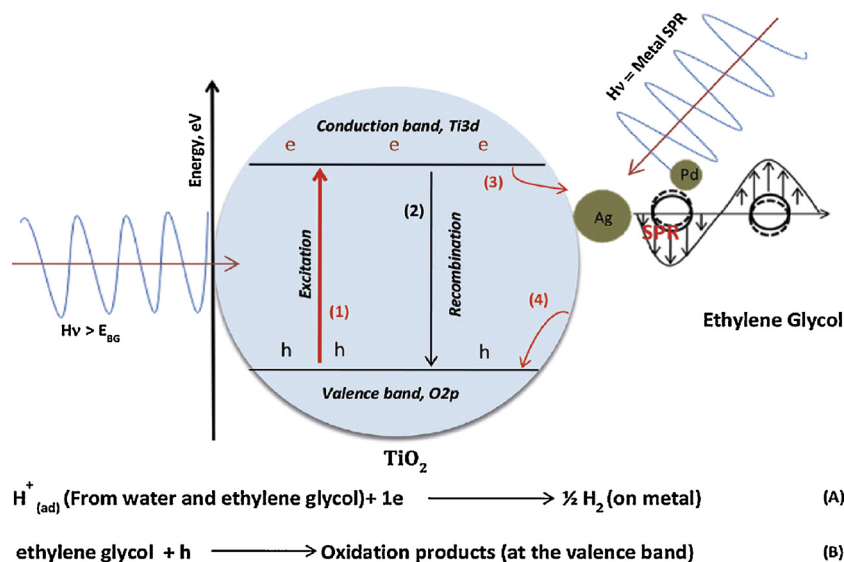
Fig. 26. Schematic representation of H_2 production using Ag-Pd/TiO_2 photocatalyst [239]. Reproduced with permission from ref. [239]. Copyright (2017), John Wiley and Sons.

efficiency.

Similarly, the synergistic effect of Ni and Au nanoparticles on the photocatalytic efficiency of TiO_2 was evaluated [244]. The H_2 production efficiency of x-Ni/TiO_2, x-Au/TiO_2 and x-Ni-Au/TiO_2 were $31\,\mu mol\,h^{-1}$, $58\,\mu mol\,h^{-1}$ and $157\,\mu mol\,h^{-1}$, respectively. The efficiency of x-Ni/TiO_2 is increased five times in the presence of a small quantity of Au (the atomic ratio of Au: Ni was 1:5 in Ni-Au/TiO_2). This is attributed to the electronic and geometric effects of both dopants. The apparent quantum efficiency (AQE) of the photocatalysts is in the following order: Ni-Au-TiO_2 > Ni/TiO_2 > Au/TiO_2 > TiO_2 (Fig. 27 (a)). The high AQE of Ni-Au/TiO_2 is attributed to the low charge carrier recombination (time resolved microwave conductivity (TRMC) signal) rate.

A proposed photocatalytic mechanism is shown in Fig. 27 (b) and (c). Ni is distributed in the form of NiO clusters and metallic nickel (Ni (0)). An ohmic junction is formed by Ni(0) between the interphase of TiO_2 and NiO. TRMC results suggested that both NiO and TiO_2 are photo-excited simultaneously under UV-light irradiation. A small amount of photo-generated electron from the CB of TiO_2 is recombined with the holes in the VB of NiO *via* the ohmic junction. Nevertheless, TRMC results revealed that the availability of photo-generated electrons in TiO_2 and Ni-TiO_2 is identical. Therefore, the ohmic contact is beneficial to avoid the photo-generated electron-hole recombination. Finally, H_2 is formed on the surfaces of Au and NiO *via* H· recombination. The bimetallic nanoparticles acted as superior H· bonding sites when compared to monometallic nanoparticles.

Metal (Sn) and non-metal (N) dopants were utilized to substantially raise the visible light absorption and charge separation efficiency of TiO_2 [245]. UV-DRS results (Fig. 28 (i)) affirmed that the absorption edge of TiO_2 is completely extended into the visible region after doping with Sn and N. This is attributed to the construction of O2p–N2p and O2p–Sn5s energy states (*i.e.* new VB edge) near the VB edge of TiO_2 (Fig. 28(iii)). XPS results also indicated that the electronic structure of TiO_2 is altered significantly *via* Ti−O−Sn and Ti−O−N linkages [246,247] (Fig. 28(ii)). The mobility, transfer and consumption ratio of photo-generated charge carriers are greatly improved by the incorporation of new energy levels. The H_2 production efficiency of Sn-N-TiO_2 ($2.81\,\mu\,mol\,h^{-1}\,g^{-1}$) was higher than the sum of N-TiO_2 and Sn-TiO_2 efficiencies under simulated solar light (*i.e.* UV–vis light) irradiation.

In another study [248], the effect of Mg doping on the inter-band defect states (formed by oxygen vacancies) of anatase TiO_2 was examined under UV light irradiation. The photocatalytic experiments were carried out in the presence of Pt as co-catalyst and methanol as sacrificial agent. For photocatalysis, the defects play a major role in the formation of charge carrier recombination centers. Two different kinds of defects, shallow (below the CB minimum) and deep (above the VB maximum) defect states, were identified for TiO_2 (Fig. 29 (i)) by the transient IR absorption excitation energy scanning spectroscopy (TIR-AEESS). The results revealed that the shallow defect states are minimized, and the deep defect states are eliminated by Mg doping (0.5%) (Fig. 29 (ii)). The photocatalytic efficiency of Mg/TiO_2 was also compared with Ni/TiO_2 and Cr/TiO_2 to evaluate the role of *d*-orbital. Mg/TiO_2 displayed the highest H_2 production efficiency and there was no H_2 production using transition metal doped TiO_2. This is attributed to the formation of new defect states in the bandgap of TiO_2 by the *d* orbital of Ni or Cr. The ionic radii of Mg^{2+} (65 pm) and Ti^{4+} (68 pm) are almost identical. The calculated total density of states (DOS) of pure TiO_2, Mg-TiO_2 and Ni-TiO_2 is shown in Fig. 29 (iii). The results clearly showed that there are no defects introduced by Mg doping (Mg do not have d orbital) in the bandgap of TiO_2. Moreover, the intrinsic defects of TiO_2 are quenched by Mg doping. Because, the Mg 2p orbit is far away from the CB and VB of TiO_2. However, new defect states are created in TiO_2 and the intrinsic defects are strengthened by the Ni dopant (due to the interaction of d orbital of with oxygen vacancies).

3. Kinetics of H_2 production using metal doped TiO_2

Published reports on the kinetics of H_2 production rate using metal-doped TiO_2 are limited. Langmuir-Hinshelwood (LH) was the model used by most of the researchers to express the rate of H_2 production with respect to sacrificial agent concentration or photocatalyst loading [249–253]. In a recent study, Clarizia et al. [250] investigated the kinetic model for H_2 generation on Cu/TiO_2 *via* photo-reforming of methanol and glycerol. The mass balance equations of the main reactive species were considered to develop the kinetic model. The model was verified to establish the H_2 production rates for experiments with various concentrations of methanol and glycerol. Five important photocatalytic steps were considered to develop the kinetic model for H_2 generation:

Step-1: Light absorption and charge-carrier generation

$$C_{u_{(s)}}/TiO_2 \overset{h\nu}{\rightarrow} e^- + h^+ \tag{21}$$
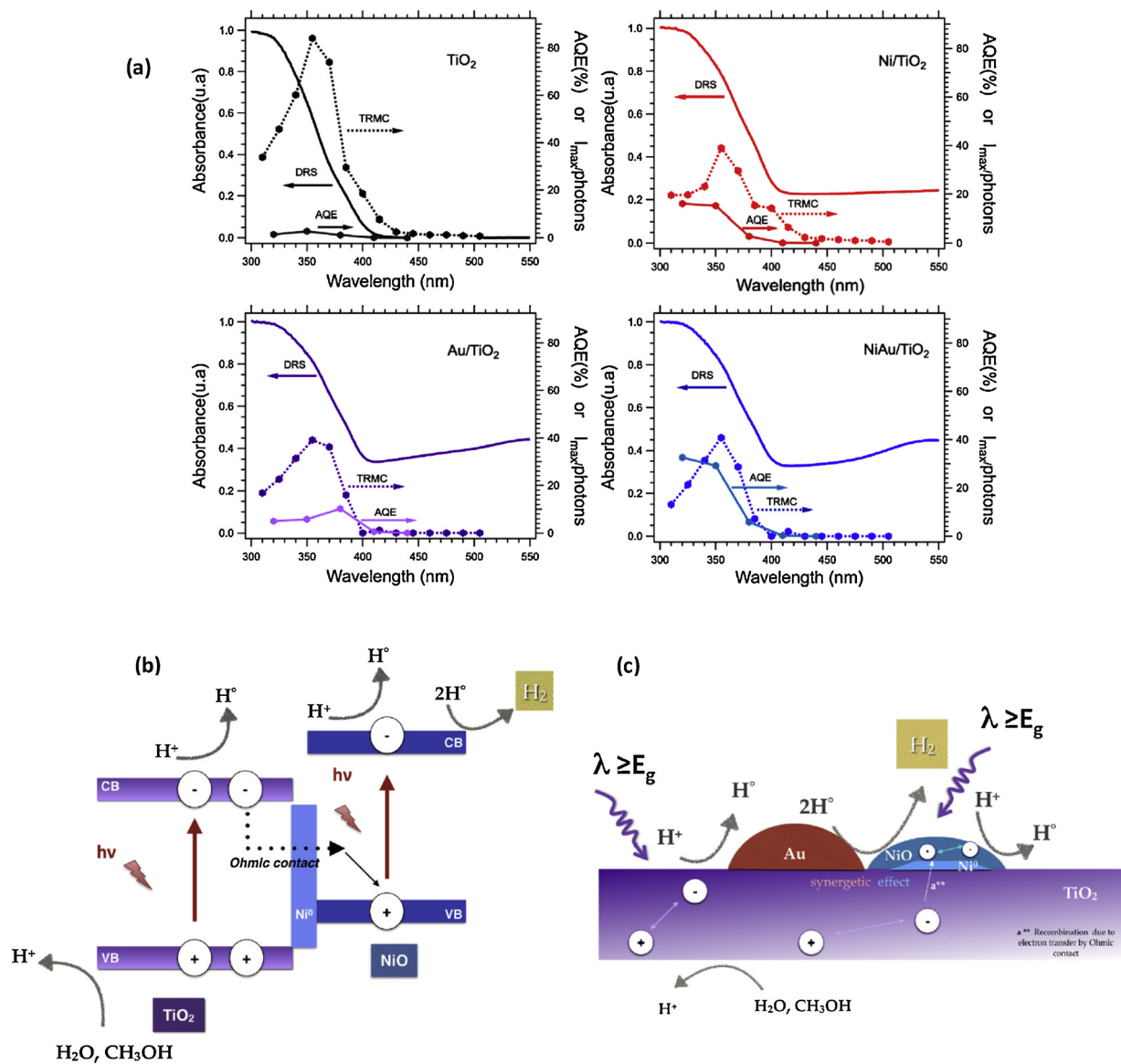
Fig. 27. (a) UV–vis-DRS, AQE and TRMC of TiO_2, Ni/TiO_2, Au/TiO_2 and $Ni-Au/TiO_2$ (b) The proposed photocatalytic mechanism of H_2 production on $Ni-TiO_2$ (c) The proposed photocatalytic mechanism of H_2 production on $Ni-Au/TiO_2$ [244]. Reproduced with permission from ref. [244]. Copyright (2016), Elsevier.

Rate of the reaction: $G = \dfrac{\phi_{UV}}{V} \cdot Q_{a,UV} + \dfrac{\phi_{VIS}}{V} \cdot Q_{a,VIS}$ (22)

The rate of the charge carrier reaction is mainly governed by the quantum yield (ϕ) and average volumetric rate of photon absorption (Q_a). The total volume of photo-irradiated solution is expressed as V.

Step-2: Charge carrier recombination

$e^- + h^+ \xrightarrow{k_r} Heat\ and\ light$ (23)

Rate of the reaction: $k_r.[h^+].[e^-]$ (24)

The charge carrier recombination reaction is ruled by the second order kinetics and k_r is the electron-hole recombination constant [251].

Step-3: *Adsorption of sacrificial agent on the catalyst surface*

$S + \because^* \overset{\longleftarrow}{\rightarrow} S^*$ (25)

$[S^*] = \dfrac{C_T\,K_{ads}\,[S]}{1 + K_{ads}[S]}$ (26)

[S^*] is the concentration of adsorbed sacrificial agent, [S] is the concentration of sacrificial agent and C_T is total concentration of active sites on the photocatalyst surface.

Step-4: Reaction of sacrificial agent with holes

$S^* + h^+ \xrightarrow{k_{h^+}} S^{\bullet*} + H^+$ (27)

Rate of the reaction: $k_{h^+}.[h^+].[S^*]$ (28)

$S^{\bullet*} + H^+ \xrightarrow{H^\bullet/fast} \because^* + S_{ox} + 2H^+$ (29)

The direct (or) indirect reaction of sacrificial agents is ruled by its adsorption behaviour on the photocatalyst surface [4].

Step-5: Photo-reduction of H^+ with e

$H^+ + e^- \xrightarrow{fast} H^\bullet \xrightarrow{H^\bullet/fast} H_2$ (30)

These five chemical reactions were used to develop the mathematical model

$\dfrac{d[S]}{dt} = -k_{h^+}.[h^+].[S^*]$ (31)

$\dfrac{d[h^+]}{dt} = G - k_r.[h^+].[e^-] - 2k_{h^+}.[h^+].[S^*]$ (32)
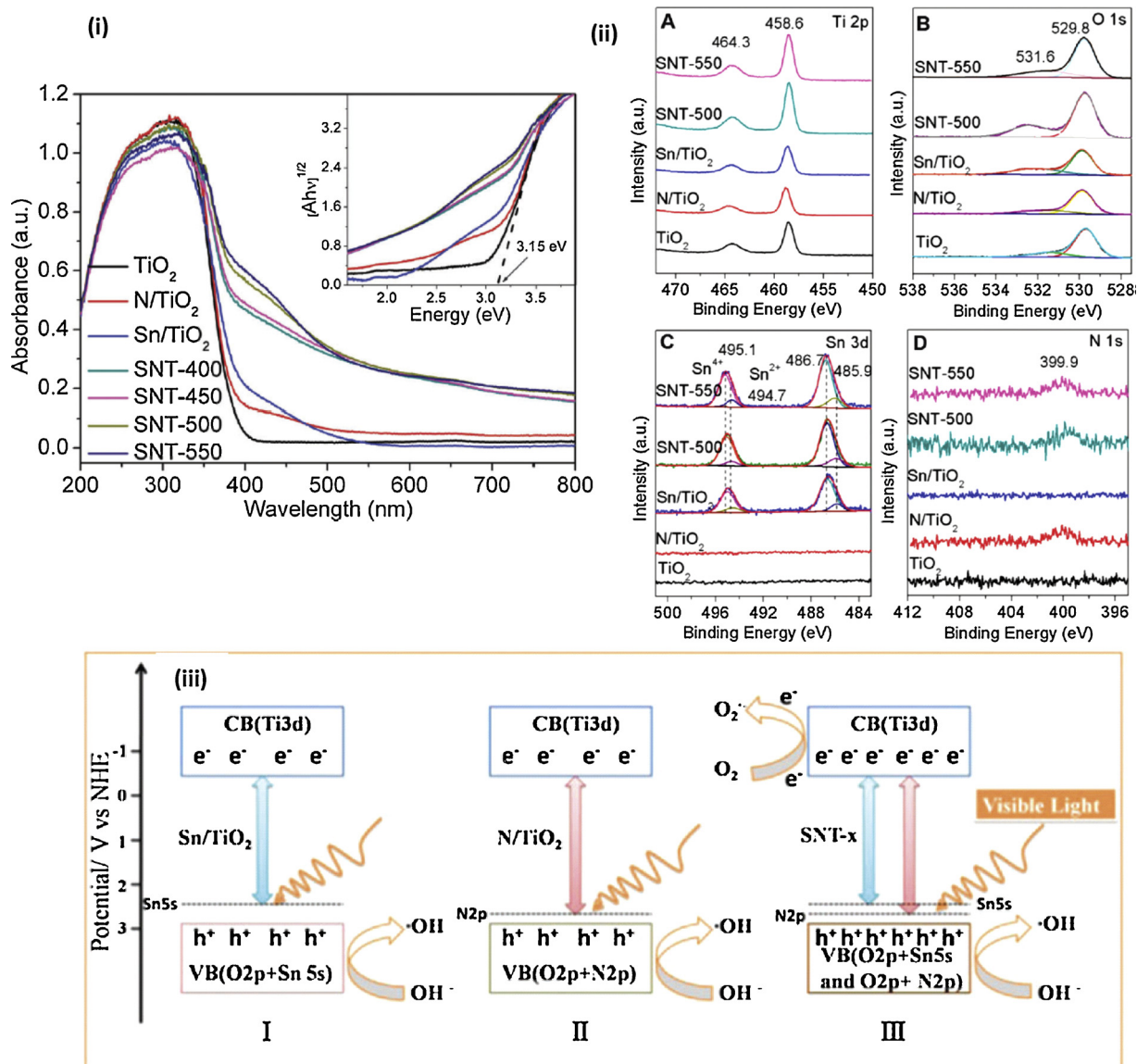
Fig. 28. (i) UV–vis-DRS of TiO_2, Sn-TiO_2, N-TiO_2, Sn-N-TiO_2 (ii) XPS of TiO_2, Sn-TiO_2, N-TiO_2, Sn-N-TiO_2 (iii) A proposed energy diagram with the formation of new energy levels in Sn/TiO_2, N/TiO_2 and Sn-N/TiO_2 [245]. Reproduced with permission from ref. [245]. Copyright (2016), Royal Society of Chemistry.

$$\frac{d[e^-]}{dt} = G - k_{r.}[h^+].[e^-] - 2k_{h^+}[h^+].[S^*] \tag{33}$$

$$\frac{d[H_2]}{dt} = k_h + \cdot[h^+]\cdot[S^*] \tag{34}$$

$$G = G_{UV} + G_{VIS} \tag{35}$$

G_{UV} and G_{VIS} values were calculated from the irradiance of the lamp and extinction co-efficient of photocatalyst under UV and visible light. The possibility of using this kinetic model is a result of the availability of parameters such as ϕ_{UV}, ϕ_{VIS}, k_r, k_{h+} and K_{ads}. Among these parameters, K_{ads} was directly determined from the experiments using LH model. K_{ads} values were calculated from the plot of $1/r_{H2}$ vs $1/[S]$ (Fig. 30).

$$r_{H_2} = \frac{k' K_{ads} [S]}{1 + K_{ads} [S]} \tag{36}$$

The results showed that the electron hole recombination rate (k_r) of Cu/TiO_2 is four times lower than that of TiO_2 P25, confirming the suppression of electron-hole recombination through Cu doping. The quantum efficiency of Cu/TiO_2 is higher than that of TiO_2 P25,

suggesting the effective utilization of adsorbed energy. Moreover, the equilibrium adsorption constant of glycerol is higher than that of methanol. C_T of TiO_2 is not significantly affected by Cu doping.

In another study, the rate of H_2 production rate of Au/TiO_2 and Pd/TiO_2 was explained using LH model [252] (Fig. 31). The effect of initial glucose concentration (sacrificial agent) was studied on the H_2 production rate using Au/TiO_2 and Pd/TiO_2 under visible light irradiation. The rate of the reaction can be expressed as:

$$Rate = \frac{\ell K [sacrifical\ agent]}{1 + K [sacrifical\ agent]} \tag{37}$$

Where K is the adsorption coefficient of sacrificial agent on the photocatalyst surface and ℓ is the pseudo first order rate constant. It was found that the rate of H_2 production is constant (Rate $\approx \ell$; K[glucose] $> > 1$) at high glucose concentration, indicating zero order kinetics. At low glucose concentration, the rate of H_2 production is directly proportional to the concentration of glucose (Rate $\approx \ell$ K [glucose]; K[glucose] $< < 1$), resulting in first order kinetics.

In a similar study [254], the effect of Cu and Cu-Pt nanoparticles on the H_2 production rate of TiO_2 was investigated using methanol (20 vol %) photo-steam reforming. It was found that the H_2 production rate was
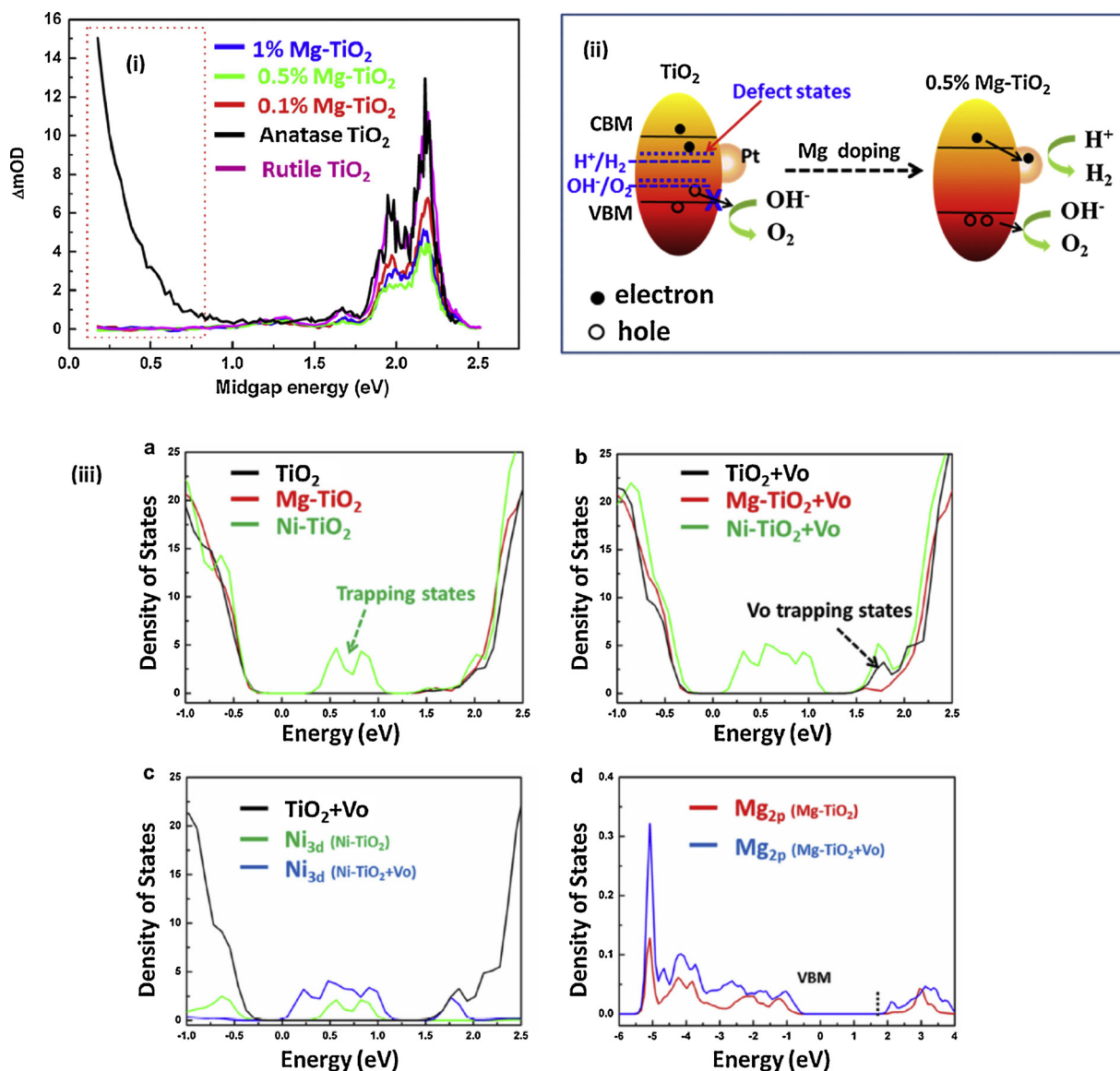
Fig. 29. (i) TIRAEESS results of Mg-TiO$_2$ (ii) Schematic representation of defect states in TiO$_2$ before and after Mg doping (iii) Calculated total DOS of pure TiO$_2$, Mg-TiO$_2$ and Ni-TiO$_2$ with/without oxygen vacancies (Vo) [248]. Reproduced with permission from ref. [248]. Copyright (2017), Elsevier.

constant and the reaction followed pseudo zero order kinetics.

The reaction intermediates and kinetics for the vapour-phase photocatalytic methanol reforming was studied using noble metal (Au) modified TiO$_2$ [255]. The oxidation path of methanol photo-reforming proceeds through the following ways: (i) indirect ˙OH –mediated route (ii) direct h$_{VB}^+$ -mediated route (iii) water assisted direct way. The proposed mechanisms were evidenced by H$_2$O/D$_2$O isotopic exchange experiments. In this reaction, methanol and water can act as electron donor (ED) species whereas the proton acts as electron acceptor (EA) species. The important steps after the generation of electron-hole pairs are the following:

(i) Adsorption of ED and EA species on the cathodic and anodic active sites of the photocatalyst

$$EA_g \leftrightarrows EA_{ads} \tag{38}$$

$$ED_g \leftrightarrows ED_{ads} \tag{39}$$

(ii) The reaction of photo-generated electrons and holes with EA and

ED at the catalyst surface

$$EA_{ads} + e_{CB}^- \rightarrow P_{1,ads} \tag{40}$$

$$ED_{ads} + h_{VB}^+ \rightarrow P_{2,ads} \tag{41}$$

Release of heat (Q) from the electron-hole recombination process

$$e_{CB}^- + h_{VB}^+ \overset{k_{recomb}}{\rightarrow} TiO_2 + Q \tag{42}$$

(iii) Desorption of products from the photocatalyst surface

$$P_{1,ads} \leftrightarrows P_{1,g} \ and \ P_{2,ads} \leftrightarrows P_{2,g} \tag{43}$$

The reactions involved in the photocatalytic vapour phase oxidation of methanol under steady state conditions is schematically shown in Fig. 32.

The intermediates and products generated from the stepwise oxidation of surface adsorbed water and methanol are given as follows:
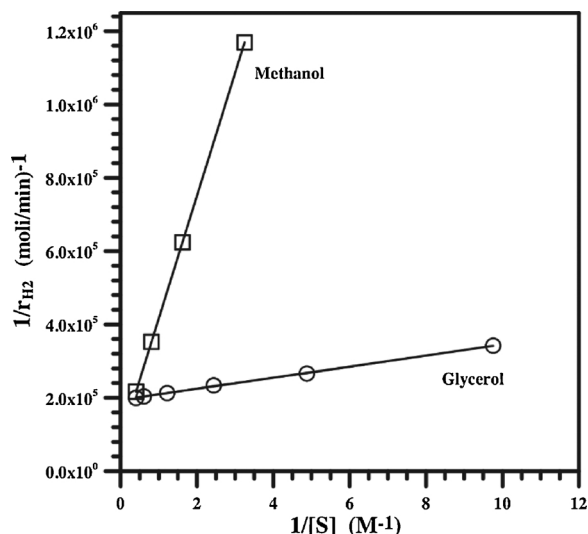
Fig. 30. The effect of glycerol and methanol concentration on the H_2 production rate of Cu/TiO$_2$ [250]. Reproduced with permission from ref. [250]. Copyright (2017), Elsevier.
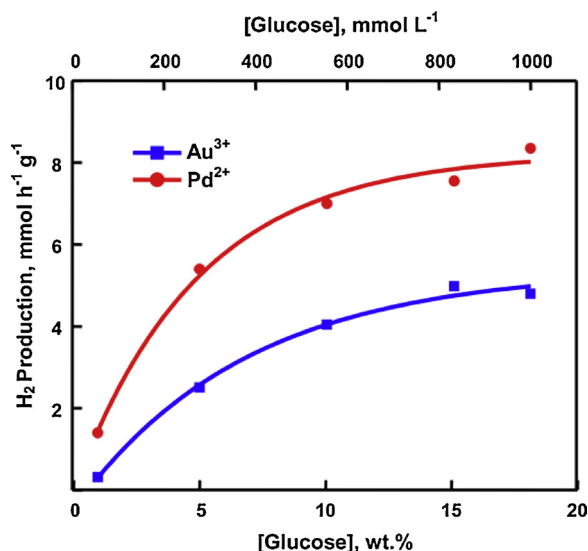
Fig. 31. The effect of glucose concentration on the H_2 production rate of Au/TiO$_2$ and Pd/TiO$_2$ [253]. Reproduced with permission from ref. [253]. Copyright (2013), Elsevier.

$$H_2O_g \overset{k_w}{\underset{k_{-w}}{\rightleftarrows}} H_2O_{ads} \tag{44}$$

$$CH_3OH_g \overset{k_m}{\underset{k_{-m}}{\rightleftarrows}} CH_3OH_{ads} \tag{45}$$

$$H_2O_{ads} + h_{VB}^+ \overset{k_1}{\rightarrow} \bullet OH_{ads} + H_{ads}^+ \tag{46}$$

$$CH_3OH_{ads} + \bullet OH_{ads} \, (or \, h_{VB}^+) \overset{k_2}{\rightarrow} CH_3O_{ads}^\bullet + H_2O \, (or \, H_{ads}^+) \tag{47}$$

$$CH_3O_{ads}^\bullet + \bullet OH_{ads} \, (or \, h_{VB}^+) \overset{k_2'}{\rightarrow} H_2CO_{ads} + H_2O \, (or \, H_{ads}^+) \tag{48}$$

$$H_2CO_{ads} \overset{k_{des,H_2CO}}{\rightarrow} H_2CO_g \tag{49}$$

$$H_2CO_{ads} + \bullet OH_{ads} \, (or \, h_{VB}^+) \overset{k_3}{\rightarrow} HCO_{ads}^\bullet + H_2O \, (or \, H_{ads}^+) \tag{50}$$

$$HCO_{ads}^\bullet + \bullet OH_{ads} \overset{k_3'}{\rightarrow} HCOOH_{ads} \tag{51}$$

$$HCOOH_{ads} \overset{k_{des,HCOOH}}{\rightarrow} HCOOH_g \tag{52}$$

$$HCOOH_{ads} + \bullet OH_{ads} \, (or \, h_{VB}^+) \overset{k_4}{\rightarrow} \bullet COOH_{ads} + H_2O \, (or \, H_{ads}^+) \tag{53}$$

$$\bullet COOH_{ads} + \bullet OH_{ads} \, (or \, h_{VB}^+) \overset{k_4'}{\rightarrow} CO_{2,ads} + H_2O \, (or \, H_{ads}^+) \tag{54}$$

$$CO_{2,ads} \overset{k_{des,CO_2}}{\rightarrow} CO_{2,g} \tag{55}$$

$$2H_{ads}^+ + 2e_{CB}^- \overset{k_{red}}{\rightarrow} H_2 \tag{56}$$

Methanol (CH_3OH) is oxidized into carbon dioxide (CO_2) *via* formaldehyde (H_2CO) and formic acid ($HCOOH$) intermediates. Each oxidation step may progress through the direct reaction of surface adsorbed species with holes (h_{VB}^+) or indirect reaction with hydroxyl radicals ($\bullet OH$). The concentration of the adsorbed species on the photocatalyst surface is constant under steady state conditions. The kinetic rate expression for the products or intermediates are given as follows:

$$\frac{d[CH_3O_{ads}^\bullet]}{dt} = r_2 - r_2' = 0 \tag{57}$$

$$\frac{d[H_2CO_{ads}]}{dt} = r_2' - r_3 - r_{des,H_2CO} = 0 \tag{58}$$

$$\frac{d[CHO_{ads}^\bullet]}{dt} = r_3 - r_3' = 0 \tag{59}$$

$$\frac{d[HCOOH_{ads}]}{dt} = r_3' - r_4 - r_{des,HCOOH} = 0 \tag{60}$$

$$\frac{d[HCOO_{ads}^\bullet]}{dt} = r_4 - r_4' = 0 \tag{61}$$
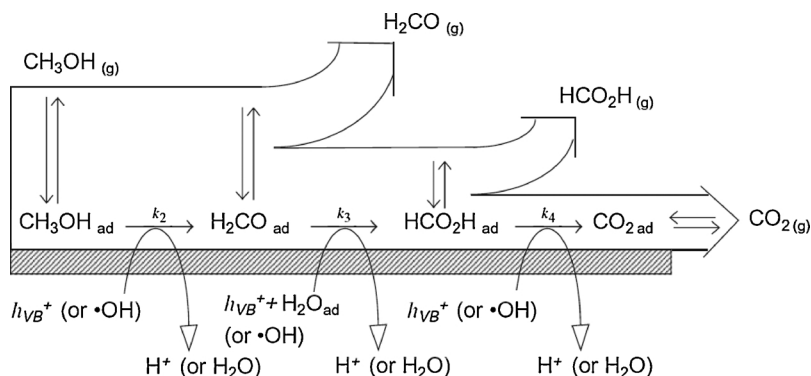
Fig. 32. Schematic of the reactions involved in the photocatalytic vapour phase oxidation of methanol under steady state conditions [255]. Reproduced with permission from ref. [255]. Copyrights (2011), Elsevier.

$$\frac{d[CO_{2,ads}]}{dt} = r_4' - r_{des,CO_2} = 0 \tag{62}$$

The overall rate of CH_3OH conversion is equal to the sum of the rates of H_2CO, $HCOOH$ and CO_2 formation.

$$r_{des,H_2CO} + r_{des,HCOOH} + r_{des,CO_2} = r_2 \tag{63}$$

The rates of H_2CO, $HCOOH$, and CO_2 production are equal to:

$$r_{des,H_2CO} = r_2' - r_3 = r_2 - r_3 \tag{64}$$

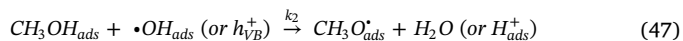$$r_{des,HCOOH} = r_3' - r_4 = r_3 - r_4' \tag{65}$$

$$r_{des,CO_2} = r_4' = r_4 \tag{66}$$

Based on the proposed scheme, the rate of each oxidation step is the sum of the rates of direct and indirect reactions by h_{VB}^+ and $\cdot OH$, respectively.

$$r_2 = k_2^{OH}\theta_{OH}\theta_{CH_3OH} + k_2^h[h_{VB}^+]\theta_{CH_3OH} \tag{67}$$

Where k_2^{OH} and k_2^h are the rate constants of the $\cdot OH$ -mediated and h_{VB}^+ -mediated reactions, respectively. The surface concentration of holes is denoted as $[h_{VB}^+]$. θ is the fraction of surface active sites enclosed by the respective adsorbed intermediate species. k_2^{OH} and k_2^h can be calculated from the sum of rate constants of the three products such as H_2CO, $HCOOH$ and CO_2 formation.

$$k_2^{OH} = k_{H_2CO}^{OH} + k_{HCOOH}^{OH} + k_{CO_2}^{OH} = \sum k_i^{OH} \tag{68}$$

$$k_2^h = k_{H_2CO}^h + k_{HCOOH}^h + k_{CO_2}^h = \sum k_i^h \tag{69}$$

θ_{OH} and $[h_{VB}^+]$ under steady state conditions can be calculated as follows:

$$\frac{d[OH_{ads}]}{dt} = k_1[h_{VB}^+]\theta_{H_2O} - \theta_{OH}(k_2^{OH}\theta_{CH_3OH} + \sum k_j^{OH}\theta_i) = 0 \tag{70}$$

$$\theta_{OH} = \frac{k_1[h_{VB}^+]\theta_{H_2O}}{k_2^{OH}\theta_{CH_3OH} + \sum k_j^{OH}\theta_i} \tag{71}$$

$[h_{VB}^+]$ depends on the light irradiation conditions (I_a) and the photocatalyst intrinsic properties (k_{recomb} and Φ).

$$\frac{d[h_{VB}^+]}{dt} = I_a\phi - k_{recomb}[h_{VB}^+][e_{CB}^-] - [h_{VB}^+](k_1\theta_{H_2O} + \sum k_j^h\theta_i) = 0 \tag{72}$$

The charge recombination process in TiO_2 is much faster than the electron/hole transfer process.

$$I_a\phi \cong k_{recomb}[h_{VB}^+][e_{CB}^-] \tag{73}$$

Under steady state conditions photogenerated electrons are equals to that of holes ($[h_{VB}^+] \approx [e_{CB}^-]$). Therefore,

$$[h_{VB}^+] = \sqrt{\frac{I_a\phi}{k_{recomb}}} \tag{74}$$

By substituting the values of $[h_{VB}^+]$ and θ_{OH}

$$r_i = \sqrt{\frac{I_a\phi}{k_{recomb}}}\left\{\frac{k_i^{OH}k_1\theta_{H_2O}\theta_{CH_3OH}}{k_2^{OH}\theta_{CH_3OH} + \sum k_j^{OH}\theta_i} + k_i^h\theta_{CH_3OH}\right\} \tag{75}$$

According to the Langmuir model: $\theta_i = K_ip_i / (1 + \Sigma_iK_ip_i)$. K_i and p_i are the adsorption equilibrium constant and partial pressure of the "ith" product under light irradiation.

$$r_i = \frac{k_i'^{OH}K_{H_2O}p_{H_2O}K_{CH_3OH}p_{CH_3OH}}{(k_2^{OH}K_{CH_3OH}p_{CH_3OH} + \sum k_j^{OH}K_ip_i)(1 + K_{H_2O}p_{H_2O} + K_{CH_3OH}p_{CH_3OH} + \sum K_ip_i)} + \frac{k_i'^h K_{CH_3OH}p_{CH_3OH}}{(1 + K_{H_2O}p_{H_2O} + K_{CH_3OH}p_{CH_3OH} + \sum K_ip_i)} \tag{76}$$

Where $k_i'^{OH}$ and $k_i'^h$ are the constants. K_{H_2O} and K_{CH_3OH} are the adsorption equilibrium constants of H_2O, CH_3OH on the photocatalyst surface. "i" is the intermediate species. p_{H_2O} and p_{CH_3OH} (partial pressures of H_2O and CH_3OH) values are negligible with respect to their vapour pressure. Thus, $\Sigma k_jK_jp_i$ and ΣK_ip_i term can be neglected. According to the non-ideal behaviour of liquids

$$p_{H_2O} = \gamma_{H_2O}(1 - x)p_{H_2O}°, x \tag{77}$$

$$p_{CH_3OH} = \gamma_{CH_3OH} xp_{CH_3OH}° \tag{78}$$

Where $p°$ is the vapour pressure and x is the mole fraction of the liquid. The equation for r_i can be modified by substituting the activity coefficients (γ) of H_2O and CH_3OH.

$$r_i = k_i'^{OH}\frac{\gamma_{H_2O}A(1 - x)}{1 + \gamma_{H_2O}A + x(\gamma_{CH_3OH}B - \gamma_{H_2O}A)} + k_i'^h \times \frac{\gamma_{CH_3OH}Bx}{1 + \gamma_{H_2O}A + x(\gamma_{CH_3OH}B - \gamma_{H_2O}A)} \tag{79}$$

Where

$$A = K_{H_2O}p_{H_2O}°, \quad B = K_{CH_3OH}p_{CH_3OH}°, \quad k_i'^{OH} = \frac{k_i^{OH}k_1}{k_2}\sqrt{\frac{I_a\phi}{k_{recomb}}} \tag{80}$$

$$k_i'^h = k_i^h\sqrt{\frac{I_a\phi}{k_{recomb}}} \tag{81}$$

The rate of the reaction is equal to zero (0) when x becomes 0 (*i.e.* $p_{CH_3OH} = 0$). The contribution of $\cdot OH$ –mediated reaction quickly increases with increasing of x until it reaches a maximum and then decreases. The contribution is faster when B is higher than A. The contribution of h_{VB}^+–mediated reaction increases with increasing of x and it reaches the maximum value when $x = 1$ ($B/(1 + B)$). Nevertheless, H_2CO was detected as the only product as the reactant was pure CH_3OH. The overall formation rate of $HCOOH$ and CO_2 was decreased to 0 when $x = 1$. Therefore, k_{HCOOH}^h and k_{CO2}^h are 0. $k_2^h = k_{H2CO}^h$. Besides as the source of $\cdot OH$, water can act as a reactant to provide an oxygen atom during the oxidation of H_2CO to $HCOOH$. Another significant role of water is a diffusion medium for protons (H^+) formed during each oxidation step at the photocatalyst surface towards the noble metal. Reaction sites situated at the TiO_2-noble metal interface (site 1) are different from that of TiO_2 surface far from the noble metal (site 2). CH_3OH adsorbed on site 1 can directly transfer H^+ to the noble metal during the oxidation reaction to H_2CO *via* reaction with h_{VB}^+. CH_3OH adsorbed on site 2 can transfer H^+ to the noble metal through the water assisted path, suggesting the transfer H^+ with the help of nearest $\cdot OH$. Consequently, the rate-determining step of any h_{VB}^+ – mediated oxidation reaction on the TiO_2 surface sites far from the noble metals is envisaged to involve with H_2O molecules. The kinetics of water assisted path ($r_{i,wa}$) relies on the concentration of H_2O and CH_3OH adsorbed on the TiO_2 surface.

$$r_{i,wa} = k_{i,wa}[h_{VB}^+]\theta_{CH_3OH}\theta_{H_2O} \tag{82}$$

The equation for a bell shaped curve as a function of x ($r_{i,wa} = 0$ when $x = 1$ or $x = 0$ and a maximum) can be written as follows:

$$r_{i,wa} = k_{i,wa}'\frac{\gamma_{H_2O}A\gamma_{CH_3OH}Bx(1 - x)}{[1 + \gamma_{H_2O}A + x(\gamma_{CH_3OH}B - \gamma_{H_2O}A)]^2} \tag{83}$$
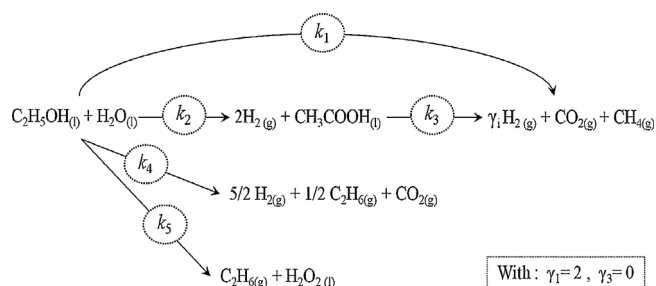
Fig. 33. The proposed mechanism of an "In Series–Parallel" reaction network for the ethanol conversion during photocatalytic H_2 production [193]. Reproduced with permission from ref. [193]. Copyright (2016), Elsevier.

$$k'_{i,wa} = k_{i,wa} \sqrt{\frac{I_a \phi}{k_{recomb}}} \tag{84}$$

In a recent study, Escobedo et al. [193] established a kinetic model for the photocatalytic H_2 production using Pt/TiO_2 and ethanol (as a sacrificial agent) in a photo-reactor with H_2 collection tank (Photo-CREC water II Reactor). The experiments were carried out with acidic pH, near UV irradiation and optimum Pt/TiO_2 loading. An "In series parallel" kinetic model was used to describe the conversion of ethanol during photocatalytic H_2 production. LH equation for the photocatalytic conversion of ethanol is given by:

$$r_i = LVRPA\, f\,[H^+] \frac{k_i^I K_i^A C_i}{1 + \sum_{j=1}^n K_j^A C_j} = \frac{k_i^* K_i^A C_i}{1 + \sum_{j=1}^n K_j^A C_j} \tag{85}$$

Here, the local volumetric rate of photon absorption is denoted as LVRPA (it can be experimentally measured *via* the irradiation light intensity macroscopic balance inside the photo-reactor), the effect of pH on photocatalytic reaction is described as $f[H^+]$, the adsorption constant (L/mol) is represented as K_i^A, the apparent reaction kinetic constant (mol/g$_{cat}$h) is represented as k_i^*, and the concentration of chemical species (mol/L) is indicated as C_i. The rate of electron-hole generation highly relies on the LVRPA. Moreover, LVRPA could be used to determine the optimum photocatalyst loading required for a photo-reactor. The average local volumetric rate of photon absorption (e^a) can be calculated by the radiative transfer equation (RTE) [36,37,40,256–258].

$$\frac{dI_{\lambda,\Omega}\,(\underline{x})}{ds} = -\kappa_\lambda I_{\lambda,\Omega}\,(\underline{x}) - \sigma_\lambda I_{\lambda,\Omega}\,(\underline{x}) + \frac{\sigma_\lambda}{4\pi} \int_{\Omega'=4\pi} p(\underline{\Omega}' \to \underline{\Omega})\, I_{\lambda,\Omega'} \tag{86}$$

Where κ_λ (spectral absorption of coefficient), σ_λ (spectral scattering coefficient) and $p(\Omega' \to \Omega)$ (scattering phase) are the optical properties of the photocatalyst suspension. κ_λ and σ_λ can be calculated using extinction efficient (β_λ – it can be measured by a standard liner regression to the plots of β_λ *versus* photocatalyst loading) and albedo function (ω_λ – the amount of light scattered by the suspension).

$$\sigma_\lambda = \beta_\lambda * \omega_\lambda \tag{87}$$

$$\kappa_\lambda = \beta_\lambda - \sigma_\lambda \tag{88}$$

The scattering phase for TiO_2 based photocatalysts can be determined by the Henyey and Greenstein phase function [256,258].

$$p(\underline{\Omega}' \to \underline{\Omega}) = \frac{1 - g_\lambda^2}{(1 + g_\lambda^2 - 2g_\lambda u_0)^{3/2}} \tag{89}$$

Here, g_λ^2 is the asymmetry factor and u_0 is the director cosine between incoming and outgoing radiation at each point of the space. RTE can be solved with the help of discrete ordinate method (MOD) in a rectangular spectrophotometer cell (the detailed calculations are given in the original literature [36,37,40]). e^a could be calculated after measuring the optical properties of the photocatalyst as follows:

$$e^a = \int_\lambda \kappa_\lambda \cdot \int_{\Omega=4\pi} I_{\lambda,\Omega}\,(\underline{x})\, d\Omega d\lambda \tag{90}$$

The Photo-CREC water II Reactor was operated in the batch mode. Accordingly, the rate of the reaction can be written as follows:

$$r_i = \frac{1}{W_{irr,cat}} \frac{dN_i}{dt} = \frac{V}{W_{irr,cat}} \frac{\frac{dN_i}{V}}{dt} = \frac{V}{W_{irr,cat}} \frac{dC_i}{dt} \tag{91}$$

where $W_{irr,cat}$ describes the weight of irradiated photocatalyst in grams, V denotes the total volume of reactor in litres, N_i represents the moles of "i" species and t indicates the irradiation time in minutes.

$$r_i = \frac{dC_i}{dt} = \frac{\frac{W_{irr}}{V} k_i^* K_i^A C_i}{1 + \sum_{j=1}^n K_j^A C_j} \tag{92}$$

The above can be expressed further using an apparent rate constant

$$k_i = \frac{W_{irr}}{V} k_i^* K_i^A \tag{93}$$

$$\frac{dC_i}{dt} = \frac{k_i C_i}{1 + \sum_{j=1}^n K_j^A C_j} \tag{94}$$

Langmuir adsorption isotherm for the chemisorption of chemical species/intermediates can be described as follows:

$$\theta_A = \frac{Q_{eq,ads}}{Q_{eq,max}} = \frac{K_{eq}^A C_{eq}}{(1 + K_{eq}^A C_{eq})} \tag{95}$$

Here, θ_A is the dimensionless surface species concentration, $Q_{eq,ads}$ is the current equilibrium adsorption surface concentration (mol/g$_{cat}$), $Q_{eq,max}$ is the maximum equilibrium adsorption surface concentration (mol/g$_{cat}$), K_{eq}^A indicates the adsorption equilibrium constant (L/mol) and C_{eq} represents the gas phase concentration of the species at equilibrium (mol/L)

The linear representation of Langmuir adsorption isotherm is

$$\frac{1}{Q_{eq,ads}} = \frac{1}{Q_{eq,max} K_{eq}^A C_{eq}} + \frac{1}{Q_{eq,max}} \tag{96}$$

There is no remarkable change of adsorption constants with respect to light irradiation. Hence, it is concluded that the adsorption parameters established without light irradiation (dark) are sufficient for the kinetic modelling during the light irradiation experiment. The results revealed that equimolar concentration of hydrogen (H˙) and hydroxyl (˙OH) radicals were produced during the photocatalytic hydrogen production (a detailed analysis and calculation is given in the original literature [193]). The proposed mechanism of "In Series–Parallel" reaction network for the ethanol conversion during photocatalytic H_2 production is schematically shown in Fig. 33. The main assumptions for the kinetic model are (a) ethanol and other intermediate species could be adsorbed on the photocatalyst surface (b) ethanol and other intermediate species are not influenced by photolysis, and (c) adsorption is a dynamic equilibrium process. The following conditions are also considered to develop an "In Series–Parallel" kinetic model: (d) 0.15 g/L of 1 wt % $Pt-TiO_2$ (Degussa P25) as photocatalyst in the slurry phase (e) pH 4 (f) utilization of near-UV photons (λ < 410 nm) to promote the oxidation/reduction at the photocatalyst surface (g) ethanol initial concentration 2 v/v %, and (h) h^+ reacts with –OH to produce ˙OH radicals and e– favours the formation of H˙ radicals. The photo-conversion of ethanol through ˙OH radicals leads to the formation of H_2, methane (CH_4), ethane (C_2H_4), carbon dioxide (CO_2) and acetic acid (CH_3COOH) (i) the formation of acetaldehyde (CH_3CHO) intermediate is neglected (j) formation of H_2 *via* steps 2, 3 and 4 (Fig. 33), and (k) formation of hydrogen peroxide (H_2O_2) through step 5.

LH rate equation for the ethanol conversion during the photocatalytic H_2 production can be described as:
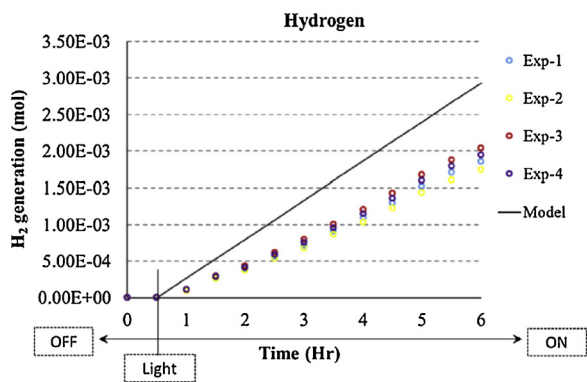
Fig. 34. Experimental and model predictions (without α = 0.65) of H_2 production under light irradiation [193]. Reproduced with permission from ref. [193]. Copyright (2016), Elsevier.

$$r_{EtOH} V_L = \frac{dN_{EtOH}}{dt} = \frac{-V_L C_{EtOH}(k_1 + k_2 + k_4 + k_5)}{1 + K_{EtOH}^A C_{EtOH} + K_{AA}^A C_{AA} + K_{EtOH}^A C_{EtOH} + K_{H_2}^A C_{H_2} + K_{CO_2}^A C_{CO_2} + K_E^A C_E + K_M^A C_M}$$

(97)

Where C_{AA}, C_E and C_M are the concentration of acetic acid, ethane and methane, respectively. The above Eq. (13) can be considered, as the concentration of ethanol is higher with respect to other intermediates in the liquid phase. The experiments revealed that ethanol is the superior adsorbed species as compared to other intermediates. Therefore, $K_{EtOH}^A C_{EtOH} >> K_{H_2}^A C_{H2} + K_{CO_2}^A C_{CO2} + K_E^A C_E + K_M^A C_M$. The ordinary differential equations for the changes in concentration of the intermediates can be described as follows:

For CH_3COOH (AA)

$$\frac{dN_{AA}}{dt} = \frac{V_L(k_2 C_{EtOH} - k_3 C_{AA})}{1 + K_{EtOH}^A C_{EtOH}}$$

(98)

For CO_2

$$\frac{dN_{CO_2}}{dt} = \frac{V_L[(k_1 + k_4)C_{EtOH} + k_3 C_{AA}]}{1 + K_{EtOH}^A C_{EtOH}}$$

(99)

For C_2H_6 (E)

$$\frac{dN_E}{dt} = \frac{V_L C_{EtOH}(1/2 k_4 + k_5)}{1 + K_{EtOH}^A C_{EtOH}}$$

(100)

For CH_4 (M)

$$\frac{dN_M}{dt} = \frac{V_L(k_1 C_{EtOH} + k_3 C_{AA})}{1 + K_{EtOH}^A C_{EtOH}}$$
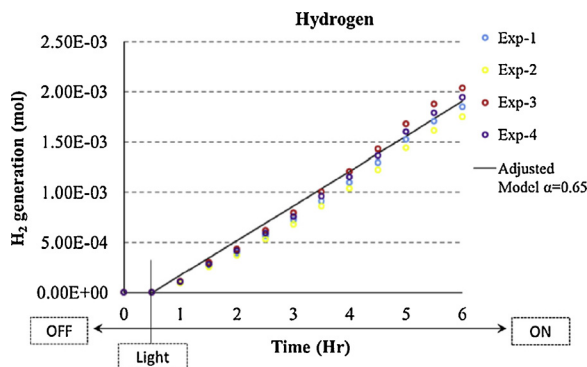
(101)

For H_2

Fig. 35. Experimental and model predictions (with α = 0.65) of H_2 production under light irradiation [193]. Reproduced with permission from ref. [193]. Copyright (2016), Elsevier.

$$\frac{dN_{H_2}}{dt} = \frac{V_L C_{EtOH}(2k_1 + 2k_2 + 2.5k_4)}{1 + K_{EtOH}^A C_{EtOH}}$$

(102)

The proposed kinetic model was predicted well the experimentally perceived quasi-linear trend of H_2 production under light irradiation (Fig. 34). Nevertheless, there was around 35% of difference between the model predictions and experimental results. This was ascribed to the following reasons: (a) reaction temperatures are higher than the supercritical temperature of CO_2 (29.14 °C), and (b) solubility of CO_2 at pH 4.

Therefore, the equation for the concentration of H_2 was revised with a term α (0.65). Fig. 35, clearly shows that the experimental data fits well with the revised kinetic model.

$$\frac{dN_{H_2}}{dt} = \alpha \frac{V_L C_{EtOH}(2k_1 + 2k_2 + 2.5k_4)}{1 + K_{EtOH}^A C_{EtOH}}$$

(103)

In a very recent study, novel concepts such as initial rate of photon absorption (IRPA) and boundary layer of photon absorption in dimensionless form were established to evaluate the impact of photocatalyst dosage on the total rate of photon absorption (TRPA- overall radiation absorbed in the entire photo-reactor volume) [259]. A six-flux absorption scattering model (SFM) [260,261] was utilized to study and model the solar/light radiation transport through the slurry photocatalyst suspension (TiO₂ P25 and goethite (α-FeOOH) were used as photocatalysts).

According to SFM approach, LVRPA can be calculated as follows:

$$e^a(x) = \frac{I_0 \tau_{app}}{\omega_{corr}(1-\gamma)L}[(\omega_{corr} - 1 + \sqrt{1 - \omega_{corr}^2})e^{-\frac{x\tau_{app}}{L}} + \gamma(\omega_{corr} - 1 - \sqrt{1 - \omega_{corr}^2})e^{\frac{x\tau_{app}}{L}}]$$

(104)

Where a, b, ω_{corr} and γ are SFM parameters. τ_{app} is the apparent thickness. L is the length of the extinction of light inside the photo-reactor.

$$a = 1 - \omega p_f - \frac{4\omega^2 p_s^2}{1 - \omega p_f - \omega p_b - 2\omega p_s}$$

(105)

$$b = \omega p_b + \frac{4\omega^2 p_s^2}{1 - \omega p_f - \omega p_b - 2\omega p_s}$$

(106)

$$\omega_{corr} = \frac{b}{a}$$

(107)

$$\gamma = \frac{1 - \sqrt{1 - \omega_{corr}^2}}{1 + \sqrt{1 - \omega_{corr}^2}} e^{-2\tau_{app}}$$

(108)

$$\tau_{app} = a\tau \sqrt{1 - \omega_{corr}^2}$$

(109)

For a planar geometry, $\tau = (\sigma^* + \kappa^*)C_{cat}L$ (110)
$IRPA = -[\frac{d}{dx}(e^a(x))]|_{x=0}$ (111) The following equation can be obtained by applying the values of ($e^a(x)$)

$$IRPA = -\frac{I_0}{\omega_{corr}(1-\gamma)}\left(\frac{\tau_{app}}{L}\right)^2 [\gamma(\omega_{corr} - 1 - \sqrt{1 - \omega_{corr}^2}) - (\omega_{corr} - 1 + \sqrt{1 - \omega_{corr}^2})]$$

(112)

By introducing the values of τ_{app} and τ, it was found that the IRPA was related to the photocatalyst concentration or loading (C_{cat})

$$IRPA = -I_0 C_{cat}^2 \psi$$

(113)

Where ψ is given by

$$\psi = (\beta^*)^2 \frac{a^2(1 - \omega_{corr}^2)}{\omega_{corr}(1-\gamma)} [\gamma(\omega_{corr} - 1 - \sqrt{1 - \omega_{corr}^2}) - (\omega_{corr} - 1 + \sqrt{1 - \omega_{corr}^2})]$$

(114)
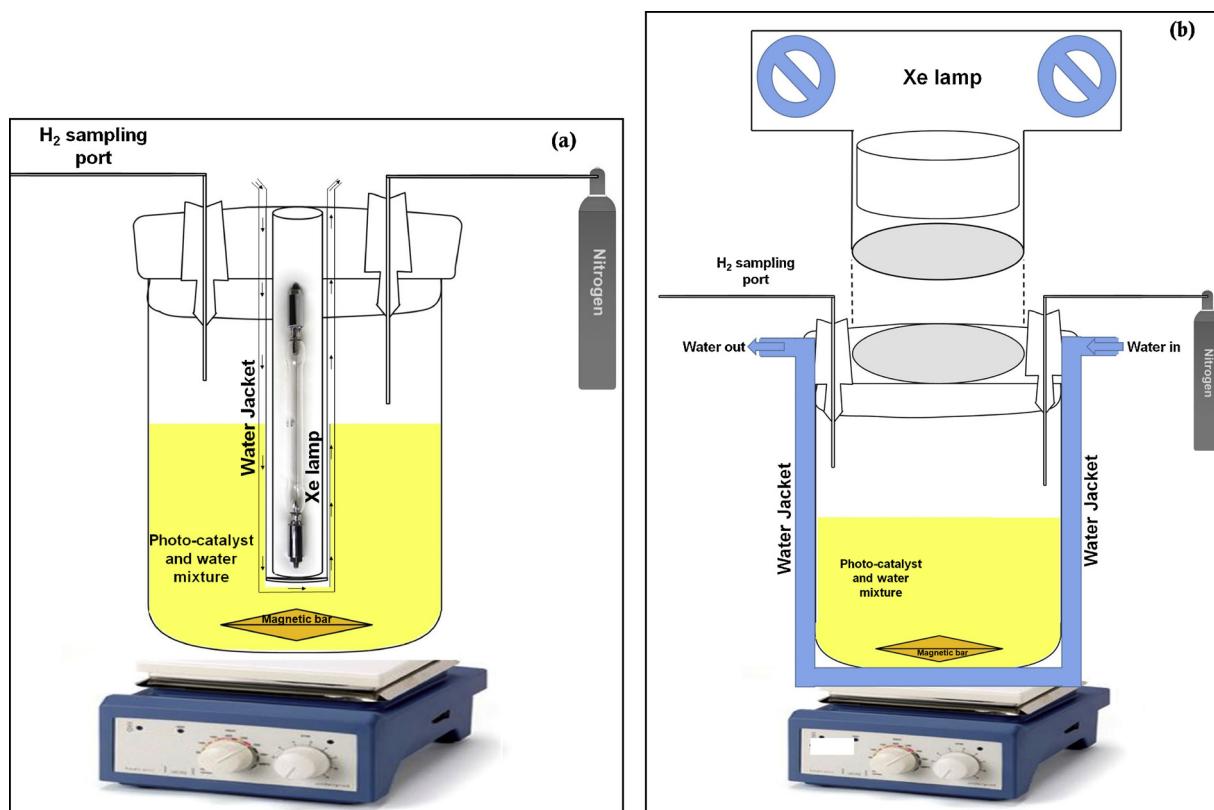
Fig. 36. Schematic of (a) Type I and (b) Type II photo-reactors for H_2 production.
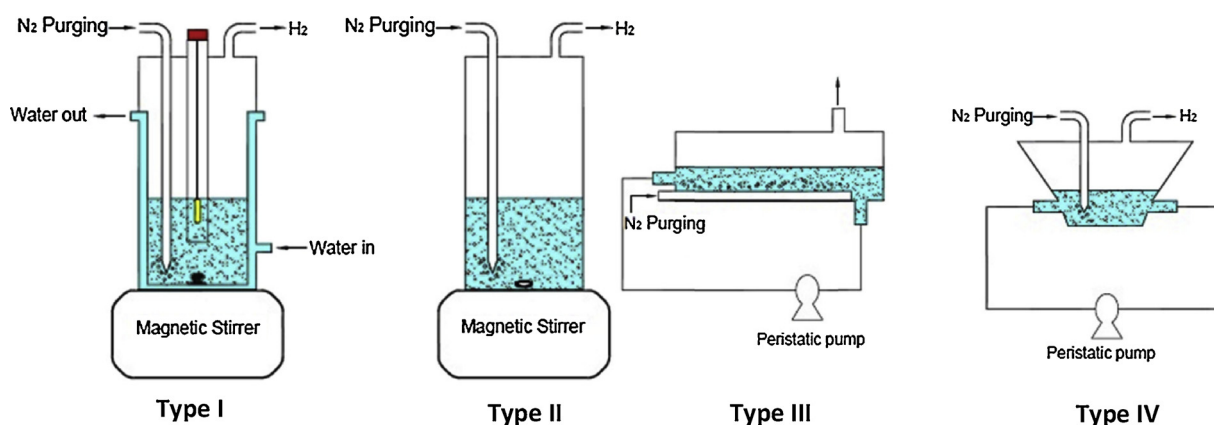
Fig. 37. Schematic of Type I, Type II, Type III and Type IV photo-reactors [265]. Reproduced with permission from ref. [265]. Copyright (2016), Elsevier.
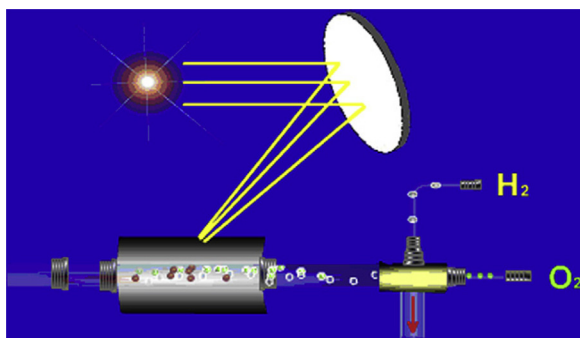
Fig. 38. Schematic of photocatalytic H_2 production reactor using natural solar light [267]. Reproduced with permission from ref. [267]. Copyright (2010), Elsevier.

$$\beta^* = \sigma^* + \kappa^* \tag{115}$$

The differences in the rate of photon absorption should be considered when comparing the efficiency of different photocatalytic materials in a slurry suspension. The results showed that the extinction of light follows a second order dependency on the photocatalyst loading. The findings of this study would be beneficial to design and scale up various types of photo-reactors (solar, slurry, planar, *etc.*) with improved optical properties.

4. Photo-reactors design for H_2 production

Researchers studying H_2 production most commonly use custom-made photo-reactors. The photoreactors are made up of quartz or pyrex with 50 ml–100 ml capacity. The reactions are carried out with 50 ml–70 ml of empty gas phase. The reactor should be a tightly closed setup to avoid any gas leakage during the photocatalysis reaction and it
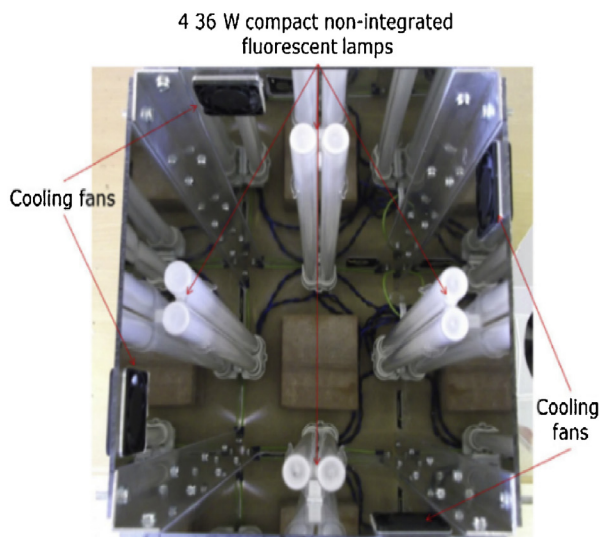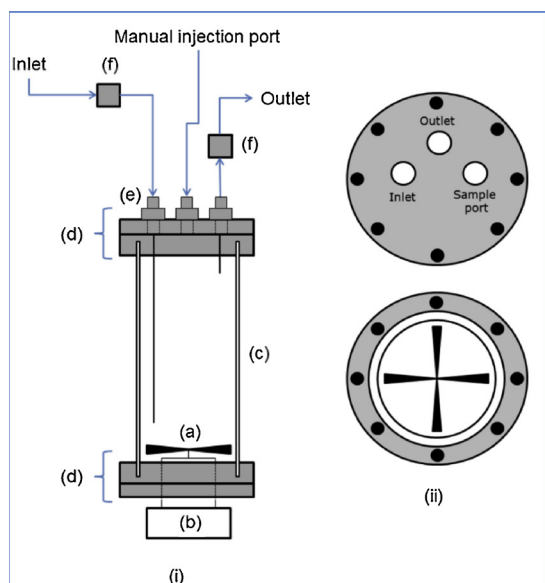
Fig. 39. Schematic of PFPR photo-reactor ((i) gas inlet, outlet, motor and flange arrangement (ii) top cap and bottom propeller view), photograph of the arrangement of UV lamps in the light box [268]. Reproduced with permission from ref. [268]. Copyright (2016), Elsevier.
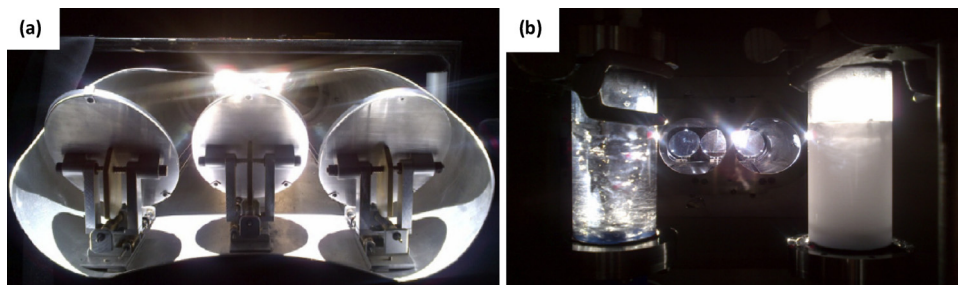
Fig. 40. Photographs of (a) series of light guiding mirrors (b) two PRPR units under solar light illumination from the telescope [268]. Reproduced with permission from ref. [268]. Copyright (2016), Elsevier.
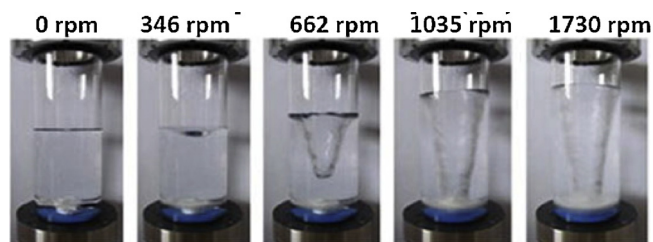
Fig. 41. Photographs of cavitation formation at various rpm [268]. Reproduced with permission from ref. [268]. Copyright (2016), Elsevier.

should also have the required gas inlet and outlet. A Xenon lamp with 300 W to 500 W is commonly used as light irradiation source. The activity of a photocatalyst is examined in the presence of either UV light or visible light or simulated solar light (without any optical filters). Visible light experiments are performed using appropriate UV light filters.

The light source may be placed on either inside (Type I) or outside (Type II) the glass reactor (Fig. 36). In type I photoreactors, a portable light irradiation source is placed inside at the centre of the reactor. While in type II, the light irradiation source is placed at a particular distance from the reactors. The distance between the light source and
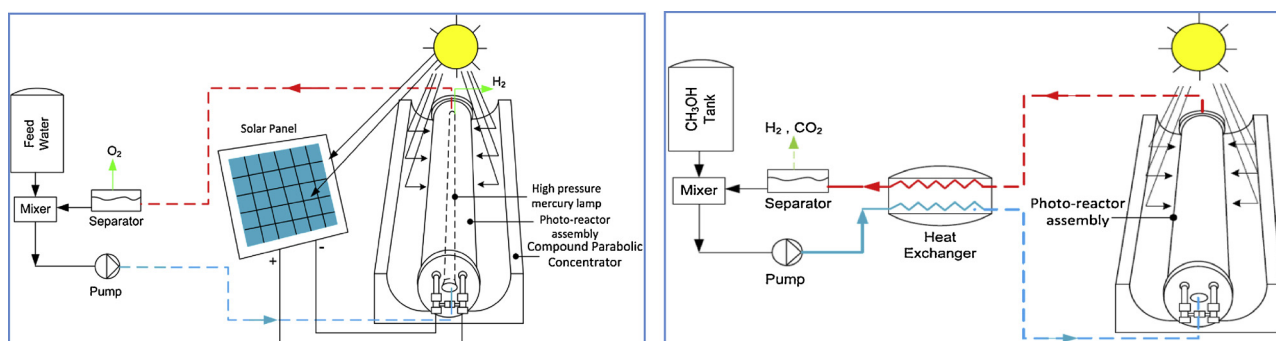
Fig. 42. Schematic of pilot scale photo-reactor for water splitting and methanol steam reforming reactions [269]. Reproduced with permission from ref. [269]. Copyright (2012), Elsevier.
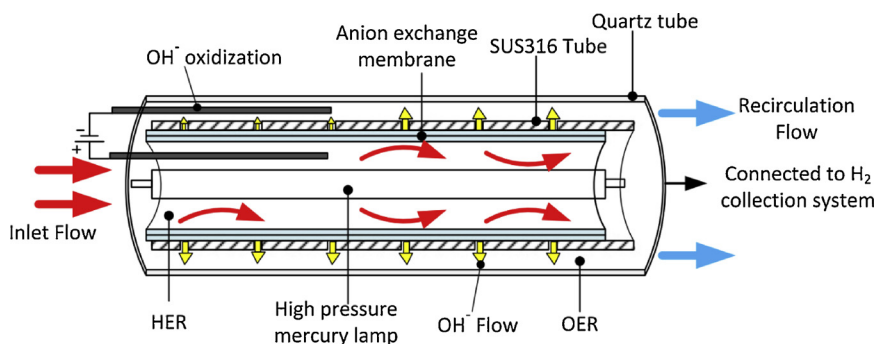
Fig. 43. Detailed schematic of the hybrid photo-reactor [269]. Reproduced with permission from ref. [269]. Copyright (2012), Elsevier.
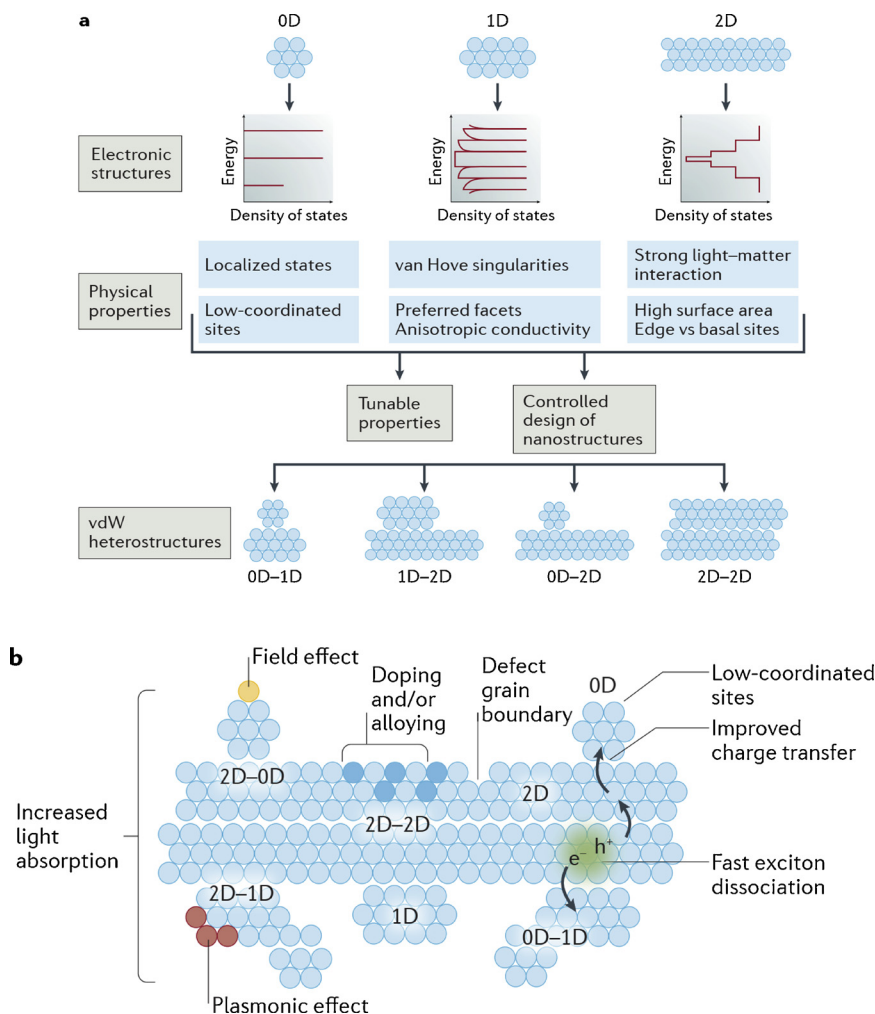
Fig. 44. (a) Schematic of the electronic and physical properties of 0D (*e.g.* nanoparticles), 1D (*e.g.* nanotubes or nanowires) and 2D (*e.g.* nanosheets) nanomaterials [277]. Reproduced with permission from ref. [277]. Copyright (2018), Springer Nature. (b) Schematic of the important features and phenomena that improve the light absorption of vdW hetero-structures [277]. Reproduced with permission from ref. [277]. Copyright (2018), Springer Nature.

the reactor is predicted by measuring the light intensity using a Lumen meter. Type I reactors are more convenient for the effective ultilization of photons because the light can spread to the reaction mixture from all the directions, hence more active surface area of the catalyst will be exposed to light.

The reactor should be vacuumized first to remove the air and the reaction mixture is purged with Ar or N$_2$ gas for 30 min–60 min before the light irradiation. A mass flow controller should be used in the purging process for the uniformity and repeatability of the experiments. In both cases, a magnetic stirrer is placed at the bottom of reactor to

continously stir the slurry to prevent the deposition or accumulation of photocatalyst. Under prolonged light irradiation, the temperature of the reaction mixture will raise. At high temperatures, the H$_2$ production efficiency is decreased because of the de-trapping of photo-generated carriers. The exothermic adsorption of reactants to the catalyst surface will also be hindered. Hence, it is very important to keep the temperature of the reaction mixture constant throughout the entire course of the photoreaction. This will be achieved through a proper water-cooling system and ventilation fans [262]. The reactions are carried out under prolonged light irradiation for 6 h – 10 h. The evolved H$_2$ gas is

Screening of 2D Materials
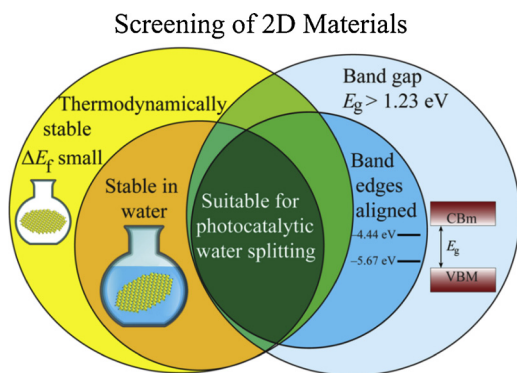
Fig. 45. Schematic for the four important conditions to screen a 2D material for photocatalytic water splitting [278]. Reproduced with permission from ref. [278]. Copyright (2015), American Chemical Society.

analyzed peroidically using gas chromatography (GC) with a thermal conductivity detector. A moleuclar seive or carbosphere packed column is used commonly to analyze the gas samples in GC. In most of the cases, the evolved H_2 was injected manually into the GC using a gas tight syringe. In recent times, some researchers are also using an online GC. However, it is very expensive when compared to the normal GC.

Muñoz-Batista et al. [263] suggested that the photo-physical events are particularly important to rule the photo-chemical activity of the system. A radiation model was studied for the lamp (both UV and visible) emission properties and the radiation field interaction with the catalyst inside the photo-reactor. The parameters such as radiation incidence efficiency (η_I) and radiation absorption efficiency (η_A) could be used to compare the configuration of photo-reactors and the photocatalytic activity of the samples in terms of its efficiency to utilize the light. η_I could be enhanced when the lamp is positioned at the central axis of the annular reactor [264]. Using of reflecting mirror is also beneficial to improve this parameter. η_A is related to the superficial rate of photon absorption ($e^{a,s}$) with the incident radiation flow at the photocatalyst surface/film. Moreover, η_I and η_A are independent of the operation conditions and reaction parameters.

η_I values can be calculated as follows

$$\eta_I = \frac{\int_A \int_\lambda q_\lambda \, d\lambda dA}{\sum_{L=1}^{L=7} \int_\lambda P_{\lambda,L} \, d\lambda} \times 100 \tag{116}$$

η_A values can be calculated as follows

$$\eta_A = \frac{\int_A \int_\lambda e_\lambda^{a,s} \, d\lambda dA}{\int_A \int_\lambda q_\lambda \, d\lambda dA} \times 100 \tag{117}$$

The photocatalytic activity under light irradiation can be calculated in terms of quantum (η_q) and photonic (η_p) efficiencies.

$$\eta_q = \frac{\langle r \rangle_A}{\langle e^{a,s} \rangle_A} \times 100 \tag{118}$$

$$\eta_p = \frac{\langle r \rangle_A}{\langle q \rangle_A} \times 100 \tag{119}$$

Where A is absorption, λ is wavelength, p is emission power, L is a factor relative to lamp, r is superficial reaction rate, $e^{a,s}$ is the local superficial rate of photon absorption (calculated from transmittance and reflectance spectra of the sample), and q is local net radiation flux.

Preethi and Kanmani [265] examined the performance of four different (Type I, Type II, tubular type with outer irradiation (Type III) and trapezoidal type with outer irradiation (Type IV)) photo-reactors for H_2 production using sulphide wastewater and (CdS + ZnS)/Fe_2O_3 photocatalyst. The schematic and photographs of the four photo-reactors are displayed in Fig. 37. All the photo-reactors have different dimensions, but the capacity of the reactor was fixed as 500 ml. Type I reactor was made of borosilicate and the other three types were made of acrylic. In each case, the experiments were carried out for 1 h and the suspension was purged with N_2 for 1 h before starting the light irradiation. The operating parameters such as light intensity, pH, photocatalyst loading and sulphide/sulphite concentrations were optimized. The achieved H_2 production rate of Type I photo-reactor is very high (7857 µmol/h) when compared to the other configurations (Type II = 938 µmol/h; Type III = 580 µmol/h; and Type IV = 1116 µmol/h).

Maximum H_2 production efficiency was attained in a reactor with an inner light irradiation source. This is ascribed to the photocatalyst being able directly absorb more photons in type I reactor, whereas, the distance between the light source and suspension was 30 cm in the reactors with outer light irradiation, and hence the photocatalyst could not absorb more photons. Among the three outer irradiation type reactors, Type IV with trapezoidal configuration showed good efficiency. This is attributed to the reactor with flat surface being able to absorb more light when compared to tubular and cylindrical reactors. The pilot scale studies will be conducted with Type IV reactor in the future because the cylindrical Type I reactors are considered not feasible for practical applications.

Even though, the direct water splitting reaction can be executed in a single reactor, one of the main disadvantages is the necessity of separating H_2/O_2 during the process. The continuous irradiation of the reaction mixture without removing the formed products can lead to a
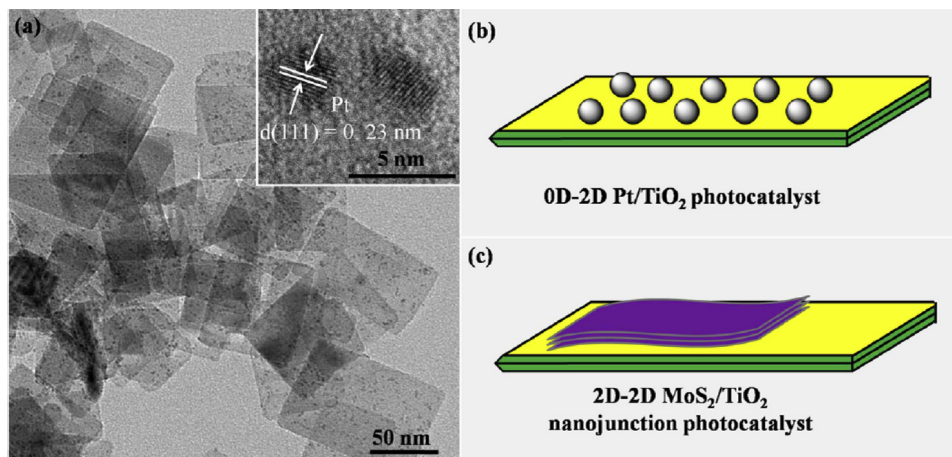
Fig. 46. (a) TEM image of 0D-2D Pt/TiO_2 (b) Schematic of 0D-2D Pt/TiO_2 (c) Schematic of 2D-2D MoS$_2$/TiO_2 [270]. Reproduced with permission from ref. [270]. Copyright (2016), American Chemical Society.
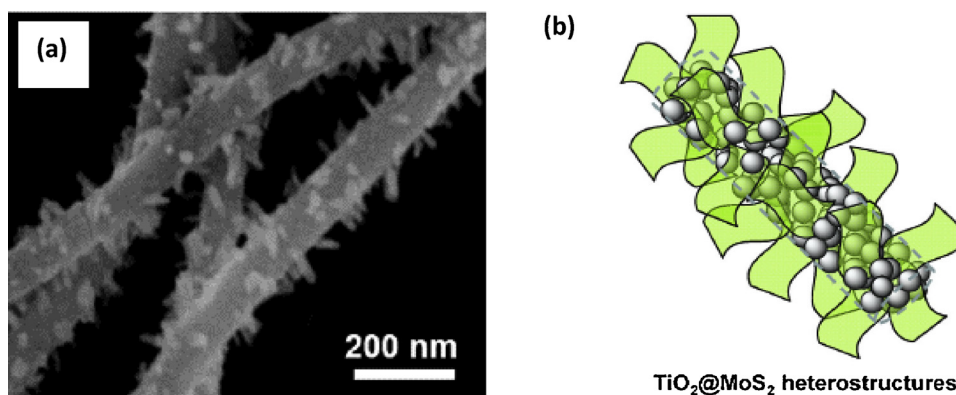
Fig. 47. (a) FE-SEM image of MoS_2 sheets on TiO_2 nanofiber (b) Schematic of $TiO_2@MoS_2$ hetero-structure [276]. Reproduced with permission from ref. [276]. Copyright (2015), Elsevier.
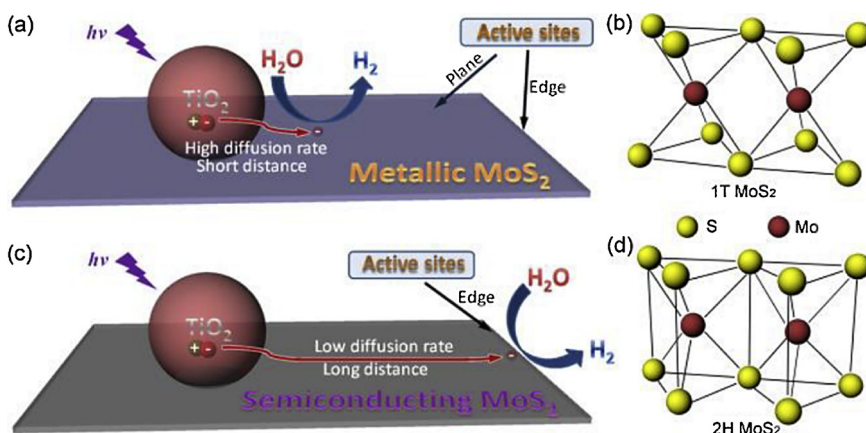
**Fig. 48.** (a) Schematic of charge transfer in TiO_2 with octahedral phase MoS_2 (b) crystal structure of octahedral MoS_2 sheets (c) Schematic of charge transfer in TiO_2 with trigonal prismatic phase MoS_2 (d) Crystal structure of trigonal prismatic MoS_2 sheets [286]. Reproduced with permission from ref. [286]. Copyright (2015), Springer Nature.
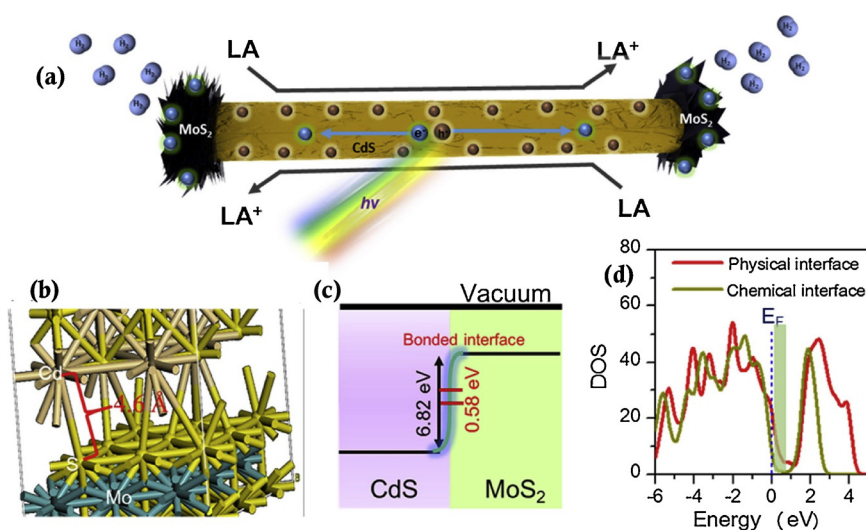
Fig. 49. (a) Schematic of photocatalytic H_2 production mechanism in 2D $MoS_2@1D$ CdS (b) chemical bonded interface of MoS_2 tipped CdS nanowires (c) Band diagram of 2D $MoS_2@1D$ CdS interface (d) The calculated DOS of chemical and physical 2D $MoS_2@1D$ CdS interface [274]. Reproduced with permission from ref. [274]. Copyright (2017), Elsevier.

photo-stationary state. In this state, the forward and backward reactions attain equilibrium because the catalyst for water splitting can also act as favorable catalyst for H_2 and O_2 recombination. This problem can be resolved *via* cycling the reaction mixture in a transparent semi-permeable polymer pipe which separates H_2 and O_2. The molecular sieving effect ($H_2 = 2.9$ Å; $O_2 = 3.5$ Å) of the polymer membrane is utilized for the effective separation of H_2 and O_2 gases [266]. H_2 can be easily diffused through the polymer membrane owing to its small atomic size. The formed H_2 and O_2 gases are stored in separate tanks.

The scale-up process of photocatalytic water splitting has many complications in terms of dispersion, separation and collection of photocatalyst. Highly active, stable and inexpensive materials are required to design a cost effective photo-reactor. Jing et al. demonstrated the feasibility of a natural solar light driven photo-reactor using the solar light concentrator (compound parabolic collector (CPC)) to receive maximum light intensity [267] (Fig. 38). It is a double bed photo-reactor where H_2 production occurs in one bed and the sacrificial agent is regenerated in another. This reactor is kept under direct sunlight and the aperture of CPC is placed perpendicular to the incident light. The reaction parameters (tube radius, flow velocity, photocatalyst loading
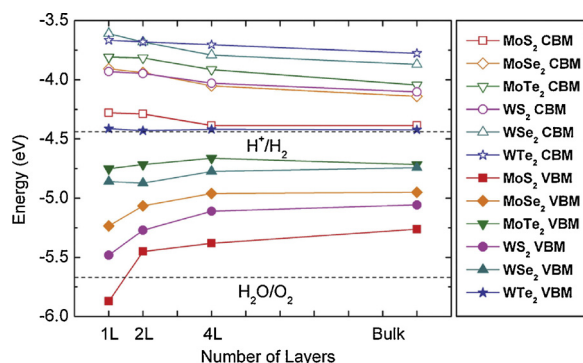
Fig. 50. The VBM and CBM positions of TMD with respect to the number of layers [287]. Reproduced with permission from ref. [287]. Copyright (2013), American Institute of Physics.
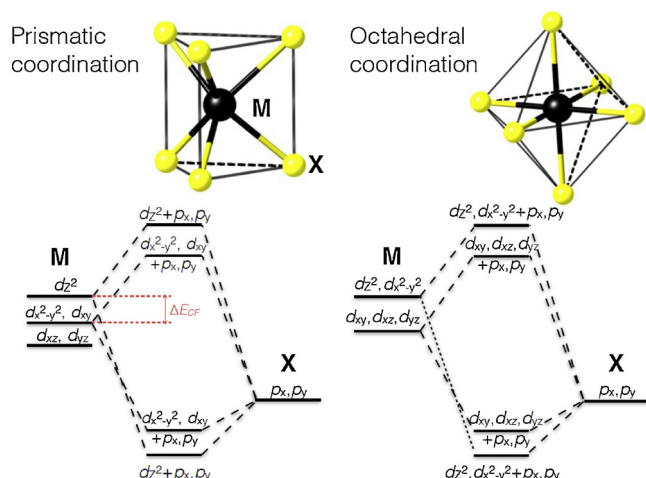
Fig. 51. Schematic representation of orbitals (*p*, *d*) hybridization and splitting in single layered TMD [288]. Reproduced with permission from ref. [288]. Copyright (2016), Royal society of Chemistry.
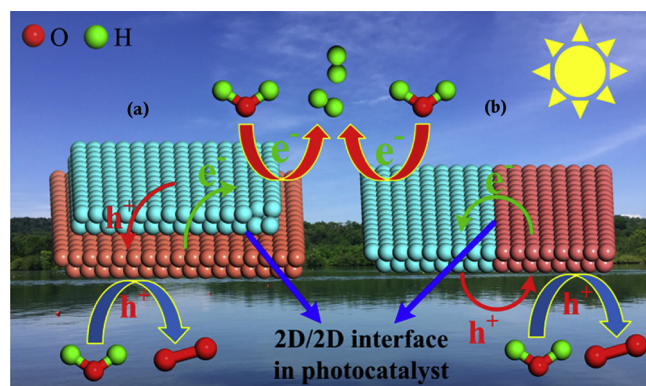
Fig. 52. Schematic illustration of 2D-2D (a) Inter-plane and (b) Intra-plane interfaces [289]. Reproduced with permission from ref. [289]. Copyright (2018), American Chemical Society.

and sacrificial agent concentration) were optimized. The flow of the slurry was adjusted to Reynolds number between 10000 and 50000 to avoid the sedimentation and accumulation of photocatalyst. The maximum hydrogen production rate was 1.88 L/h using 1 g/L of TiO_2. However, the achieved quantum efficiency of the reaction was very low (0.47%). This might be attributed to the difference in the slurry pressure gradient in the reactor. Moreover, it is found that the catalyst is deposited at the bottom of reactor tank. Due to the bed formation of the

catalyst, excess pressure is dropped in the system and it leads to a decrease in effective surface area for the photocatalysis reaction.

In another study, the photocatalytic H_2 production was investigated using a propeller-fluidized photo-reactor (PFPR) under UV and natural solar light irradiation [268]. A solar telescope was used as an alternative to CPC for solar light experiments. The reactor was made up of quartz with a stainless steel flange and a motor in the bottom. The total volume of the reactor is 210 ml. The photocatalytic H_2 production experiments were conducted using 100 ml of reaction mixture (0.025 M of oxalic acid in Milli-Q-water and 100 mg of photocatalyst) and 110 ml of gas headspace. Pt-C_3N_4 and $NaTaO_3$.La were used as photocatalysts for UV and solar light, respectively. The fluidization was achieved *via* the rotation of a 38 mm 4-blade SS 316 propeller placed at the bottom of the reactor. The propeller was operated by a 12 dcV motor to attain a rotation speed in the range of 0–1730 rpm. The reaction mixture was initially purged with Ar for 30 min at 289 rpm before the light irradiation. The rotation speed was increased to the desired level during the light irradiation. The reactions were carried out for 6 h and the H_2 production was analysed periodically using a GC-TCD. UV light irradiation was provided through four 36 W compact non-integrated fluorescent lamps with nine air blow fans. The schematic of the photoreactor and the photographs of UV lamp set up are displayed in Fig. 39.

The photo-reactor was placed at the centre. A George Ellery Hale solar telescope with a series of angled mirrors and illumination shafts (Fig. 40) was used to concentrate the natural solar light.

For UV light, the H_2 production rate is increased (at 0 rpm and at 1035 rpm) with increase of propeller speed from 0 rpm (24 μmol h^{-1} g^{-1}) to 1035 rpm (89 μmol h^{-1} g^{-1}) (Fig. 41). This is ascribed to high mass transfer, cavitation of the aqueous medium, strong light penetration and conversion of laminar to turbulent flow. The cavitation process was started at 289 rpm. The major limitation of this design is low levels of H_2 production under dark conditions because of stainless steel corrosion by oxalic acid.

$$Fe \rightarrow Fe^{2+} + 2e \tag{120}$$

$$2H^+ + 2e \rightarrow H_2 \tag{121}$$

H_2 production efficiency under natural solar light is lower (5 μmol h^{-1} g^{-1}) than the efficiency under artificial light. This is attributed to the weather, exposure of light to various contaminants (the light path length is approximately 40 ft) and variable nature of solar light.

Baniasadi et al. [269] reported the exergy (energy available to be used) and environmental impact assessment of solar photo-reactors. The schematic of photo-reactor setup for water splitting and methanol reforming systems is shown in Fig. 42. A detailed schematic of a hybrid photo-reactor is displayed in Fig. 43.

The continuous operation of photo-reactor was analysed for the water splitting and methanol steam reforming systems under large-scale process conditions. An exergy-environmental analysis was conducted to evaluate the performance of these two photoreactions based on the operational conditions. Electrodes were used to consume the photogenerated holes and transfer the photo-induced electrons for H_2 production. Both the solar light concentrator (CPC was used to concentre the natural sunlight) and UV–vis lamp (500 W high pressure Hg lamp) were placed at the reactor. An anion exchange membrane was used to separate H_2 and O_2 gases. The turbulent flow was fixed through the Reynolds number between 10,000 and 50,000 to avoid the sedimentation and accumulation of TiO_2 photocatalyst. 10 L of water was used to recirculate in the hydraulic loop. For water splitting, the photocatalyst was suspended in water and it was circulated through the hydraulic loop. For methanol steam reforming, the photocatalyst was immobilized in a packed tubular bed. The main findings of this study are described briefly. The exergy efficiency of water splitting system was increased nearly 15% by conducting the experiments at 15 °C as compared to 25 °C A maximum H_2 production rate (2 L h^{-1}) was

Fig. 53. Schematic representation of 2D-2D g-C$_3$N$_4$ nano-sheets/ZnIn$_2$S$_4$ nano-leaves synthesis and the contact interfaces of 2D-2D, 2D-0D [290]. Reproduced with permission from ref. [290]. Copyright (2018), Elsevier.

Fig. 54. Crystal structure of ABO$_3$ perovskite [293]. Reproduced with permission from ref. [293]. Copyright (2001), Elsevier.

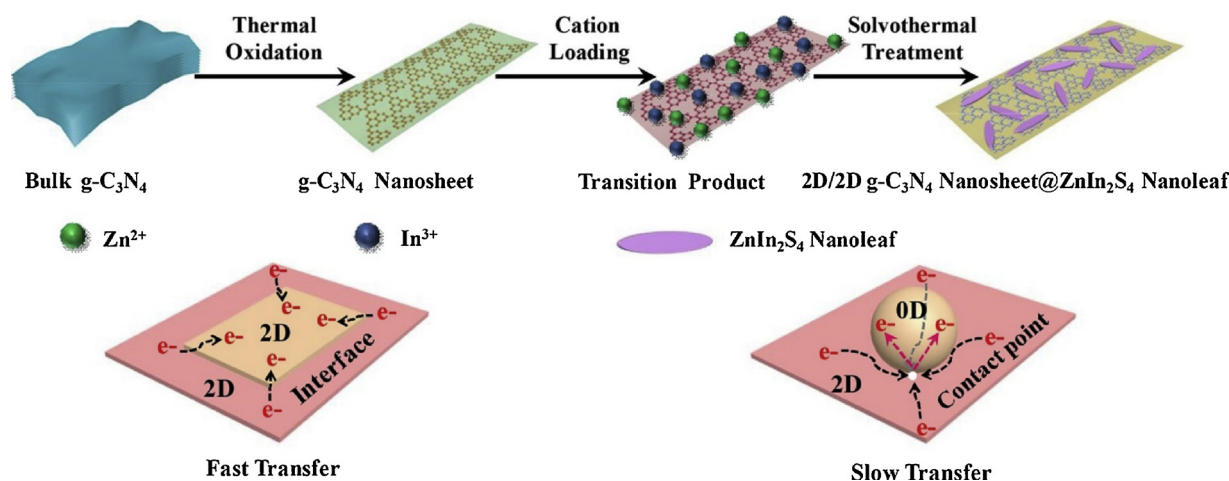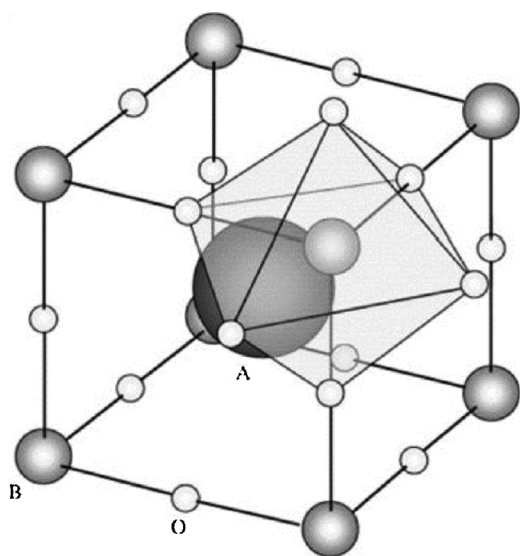attained at a flow rate of 6 L min^{-1} and the light intensity was the key parameter to influence the H$_2$ production efficiency. An optimum water-methanol mole ratio was 1.5–2 for methanol steam reforming. The exergy efficiency and CO$_2$ emission (nearly 1 kg kWh^{-1} of CO$_2$ emission at a solar intensity of 3000 W) of the methanol steam reforming system was increased by increasing the intensity of solar light. The physical and chemical exergy losses of methanol steam reforming system were higher than that of water splitting system. The optimum light intensity range of methanol steam reforming system was 530 W m^{-2} < J < 600 W m^{-2} to avoid high CO$_2$ emission.

5. Recent innovations in water splitting

5.1. 2D photocatalysts

When metal dopants are used to enrich H$_2$ production, the interfacial charge transfer process is restrained by the small area of point contact between the zero-dimensional (0D) metal dopants and TiO$_2$. To address this problem, two-dimensional (2D) photocatalysts have widely been employed with metal dopants in recent years [270–276]. The electronic and physical properties of 0D (*e.g.* nanoparticles), 1D (*e.g.* nanotubes or nanowires) and 2D (*e.g.* nanosheets) nanomaterials are

shown in Fig. 44(a) [277]. The low dimensional nanomaterials could be easily assembled into various hetero-structures (Fig. 44(b)) such as 0D–1D, 0D–2D, 1D–2D and 2D–2D *via* strong van der Waals (vdW) interactions. The light absorption capability of these hetero-structures is intensified through high charge transfer, field effect, metal doping, SPR, defect density and strain [277].

Among the various low dimensional materials, 2D materials possess some unique features, such as morphology with maximum photo-induced charge transfer, promising electronic/optical properties and high specific surface area with abundant active sites [278]. The schematic for the screening of 2D photocatalysts for H$_2$ production is displayed in Fig. 45. For effective water splitting, the 2D materials must satisfy significant characteristics such as thermodynamically stable, insoluble in water (materials with formation energy below 200 meV/atom), possess bandgap energy > 1.23 eV and appropriate band edge positions for water splitting.

The electronic properties of 2D materials are directly connected to its phases, edges and composition. Transition metal dichalcogenides (TMD) are commonly used 2D photocatalysts for water splitting because the crystalline phases and edges of TMD can be easily tuned [279,280]. The sulphur rich materials can preferentially absorb the reactants at the edges [281–283]. Moreover, 2D TMD absorbs photon in the range of 0.5–2 eV [284,285] whereas the bulk TMD only absorbs photon up to 1.4 eV. TMD are mainly composed of *d*-block (transition metal) and *p*-block (anion) elements. They are generally synthesized by sol-gel, physical vapour deposition, chemical vapour deposition, liquid phase exfoliation and atomic layer deposition techniques. MoS$_2$ is the most widely studied 2D TMD for TiO$_2$ in photocatalytic water splitting. A schematic of recently studied TiO$_2$/MoS$_2$ hetero-structures are shown in Figs. 46–48.

In all cases, H$_2$ production efficiencies of 2D TiO$_2$/MoS$_2$ hetero-structures are higher as compared to usual metal-doped TiO$_2$ and 0D TiO$_2$/MoS$_2$. This is ascribed to the availability of large contact area in the 2D hetero-structures. A higher number of transparent channels is provided by the large contact area for effective charge transfer and migration. Liu et al. [276] suggested that MoS$_2$ sheets could create a conductive superaerophobic surface to reduce gas bubble adhesion, offering a constant active surface area. H$_2$ production efficiency of TiO$_2$ with octahedral phase MoS$_2$ (TiO$_2$/1 T MoS$_2$) is 8 times higher than that of TiO$_2$ with trigonal prismatic phase MoS$_2$ (TiO$_2$/2H MoS$_2$). The high efficiency of TiO$_2$/1 T MoS$_2$ is ascribed to the availability of additional active sites on the basal plane. The probability of electron-hole recombination is minimized due to the short path length of the electron (Fig. 48).

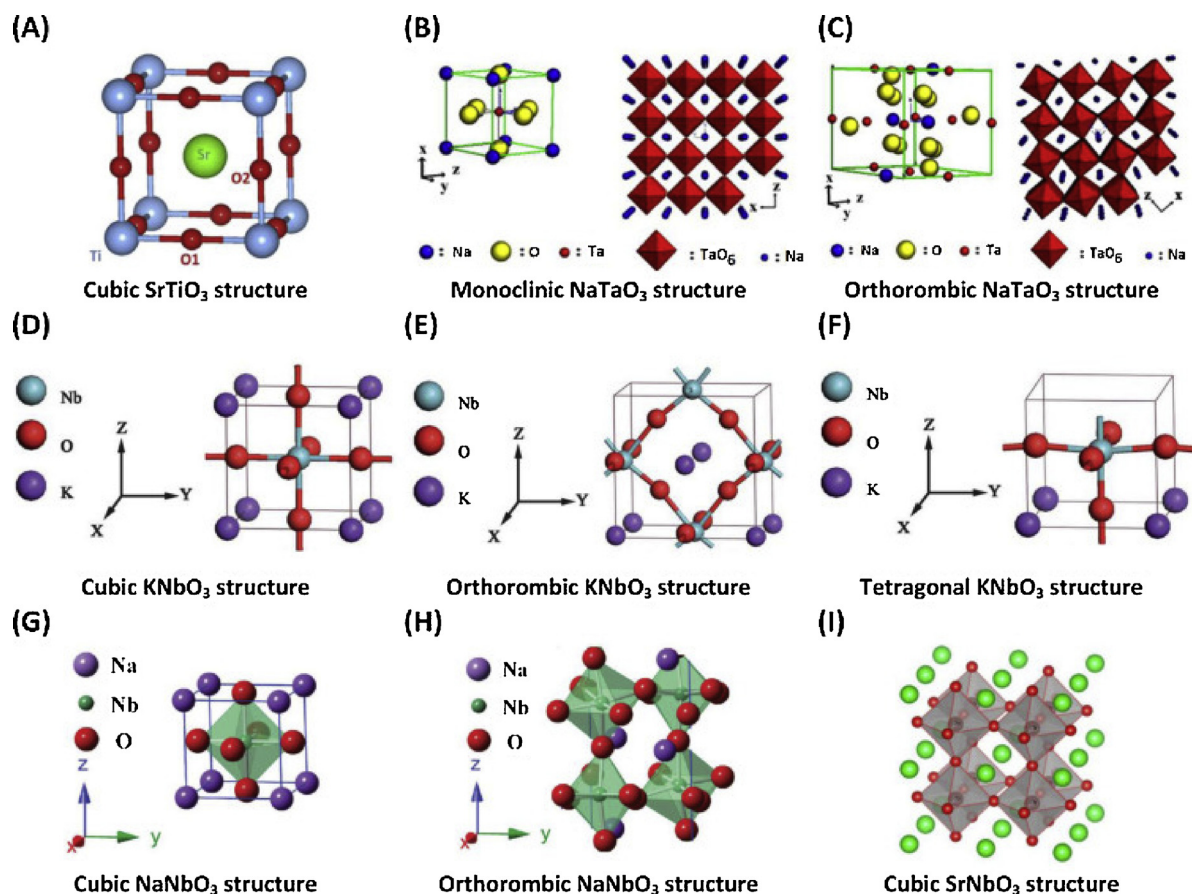The photocatalytic activity of symmetric MoS$_2$ tipped CdS

(A) Cubic SrTiO₃ structure

(B) Monoclinic NaTaO₃ structure
● : Na ○ : O ● : Ta ◆ : TaO₆ • : Na

(C) Orthorombic NaTaO₃ structure
● : Na ○ : O ● : Ta ◆ : TaO₆ • : Na

(D) Cubic KNbO₃ structure

(E) Orthorombic KNbO₃ structure

(F) Tetragonal KNbO₃ structure

(G) Cubic NaNbO₃ structure

(H) Orthorombic NaNbO₃ structure

(I) Cubic SrNbO₃ structure

Fig. 55. Perovskite oxides with various crystal geometries: (A) SrTiO₃ [296]. Reproduced with permission from ref. [296]. Copyright (2012), Elsevier. (B–C) NaTaO₃ [297]. Reproduced with permission from ref. [297]. Copyright (2007), Elsevier. (D–F) KNbO₃ [298]. Reproduced with permission from ref. [298]. Copyright (2013), Royal Society of Chemistry. (G–H) NaNbO₃ [299]. Reproduced with permission from ref. [299]. Copyright (2012), American Chemical Society (I) SrNbO₃ [300]. Reproduced with permission from ref. [300]. Copyright (2013), American Chemical Society.

nanowires (2D MoS₂@1D CdS) was studied for H₂ production under visible light irradiation [274]. The efficiency of 2D MoS₂@1D CdS (12.6 mmol h^{-1} g^{-1}) is superior as compared to Pt@CdS (2.6 mmol h^{-1} g^{-1}). This is ascribed to the availability of more catalytic active sites at the MoS₂ tip and CdS stem. (0001) crystal plane of CdS is tipped with (001) crystal plane of S through Cd-S-Mo chemical bond (Fig. 49(b)). The energy barrier (Fig. 49(c)) for the electron transfer from the chemically bonded 2D MoS₂@1D CdS interface is lower (0.58 eV) than that of the physical mixture (6.82 eV). DOS results (Fig. 49 (d)) revealed that the fermi level of 2D MoS₂@1D CdS is located above the Fermi level of MoS₂@CdS physical mixture. Hence, the electron injection form CdS into MoS₂ is progressed *via* the chemical bonds.

The light absorption property of TMD could be easily tuned by changing the number of layers [287]. The VB maximum (VBM) and CB minimum (CBM) of TMD with different layers were determined using Perdew–Burke–Ernzerhof (PBE) exchange-correlation function. The band edge positions of MoS₂ and other TMD are varied with respect to the number of layers (Fig. 50). For example, the bandgap energy of MoS₂ is increased from 0.9 eV to 1.6 eV when the number of layers are decreased from the bulk to monolayer. This might be attributed to the quantum confinement effect, *d*-orbital splitting and *p-d* orbital interaction.

The VBM and CBM positions of TMD are dominated by the *d* orbitals splitting [288]. The incompletely filled *d* orbitals of transition metals could be easily interacted with the *p* orbitals of anions. The CBM of TMD mainly originates from the antibonding states of M-$d_z{}^2$, P-p_x and P-p_y orbitals while the VBM is ruled by the bonding states of M-d_{x2-y2} and

M-d_{xy} orbitals (Fig. 51). The d-orbital splitting energy is higher when the electronegativity difference between transition metal and anion is higher. In addition to that, the d-orbital splitting is also changed when the co-ordination environment is different.

The H₂ production rate of 2D materials also relies on the interface area between the photocatalyst and co-catalyst [289]. An interface with high contact area could offer appropriate trapping and charge transfer channels for effective electron-hole separation. Using of 2D-2D interfaces could accelerate charge transfer and separation when compared to 0D-2D and 1D-2D interfaces. Two methods such as inter-plane and intra-plane are used to construct 2D-2D interfaces (Fig. 52). The photogenerated electron-hole separation process is promoted through Z-scheme and Schottky barrier mechanisms.

The photocatalytic H₂ production activity of 2D-2D g-C₃N₄ nano-sheets/ZnIn₂S₄ nano-leaves was examined under visible light irradiation [290]. The efficiency of g-C₃N₄ nano-sheets/ZnIn₂S₄ nano-leaves (2D-2D) is ~8.2 times higher than that of g-C₃N₄ nano-sheets/ZnIn₂S₄ micro-spheres (2D-0D). This is ascribed to the 2D-2D interface providing more contact area and high speed charge transfer channels as compared to 2D-0D interface (Fig. 53).

5.2. Perovskites for H₂ production

Perovskites are one of the most promising set of photocatalysts owing to their tolerance to defects, unique characteristics, compositional and structural diversity [291]. The physicochemical properties of perovskites can be easily tuned *via* replacing the cation or anion in the skeleton. Most of the perovskites are wide bandgap semiconductors and
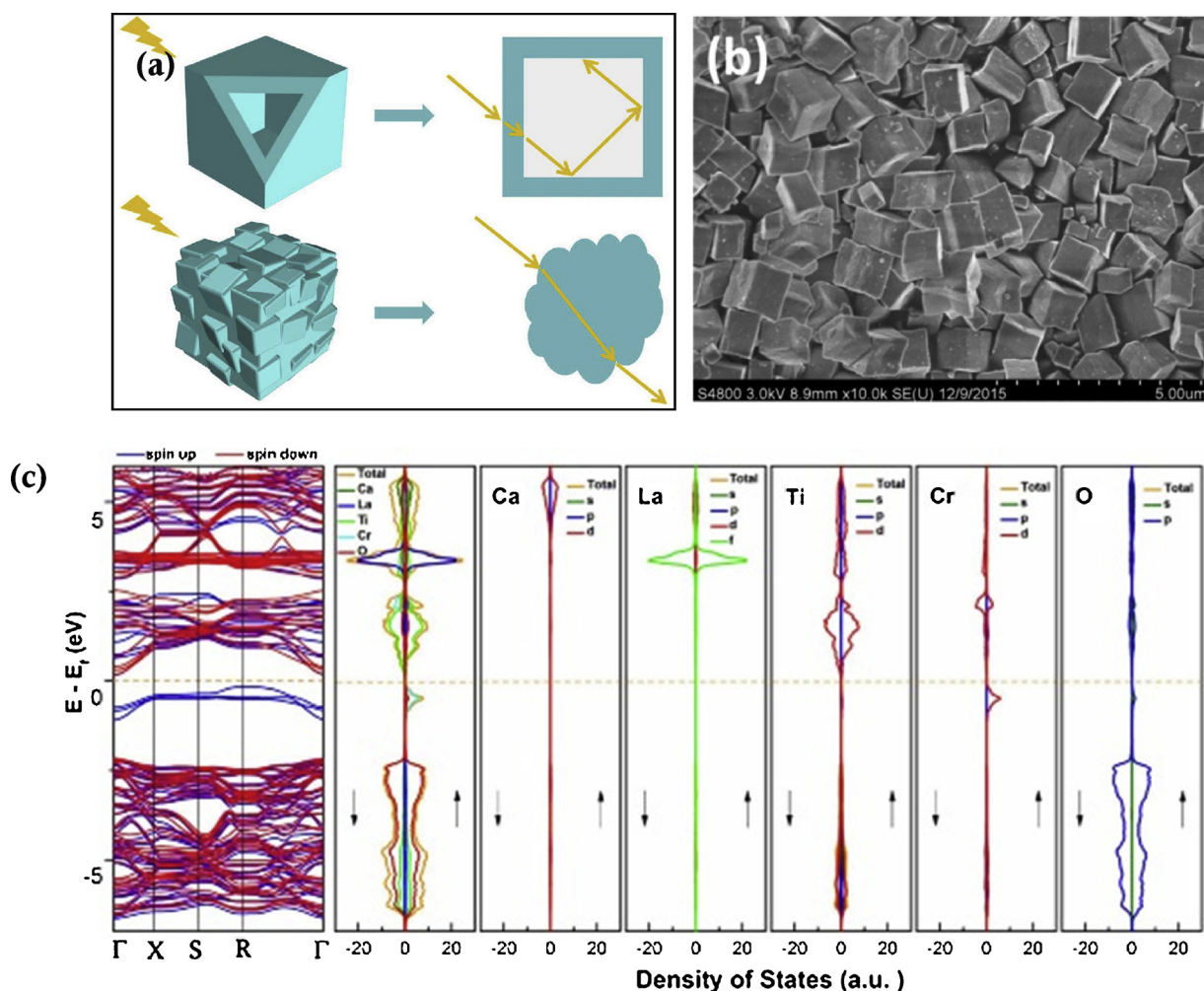
Fig. 56. (a) Schematic illustrations of light refractions and reflections in normal and cube morphology (b) SEM image of $Ca_{0.80}La_{0.20}Ti_{0.80}Cr_{0.20}O_3$ cubes (c) Calculated band structure, total density of states, and partial density of states of elements in $Ca_{0.80}La_{0.20}Ti_{0.80}Cr_{0.20}O_3$ (spin directions are specified by arrows ($\downarrow\uparrow$)) [[307]]. Reproduced with permission from ref. [[307]]. Copyright (2018), Elsevier.
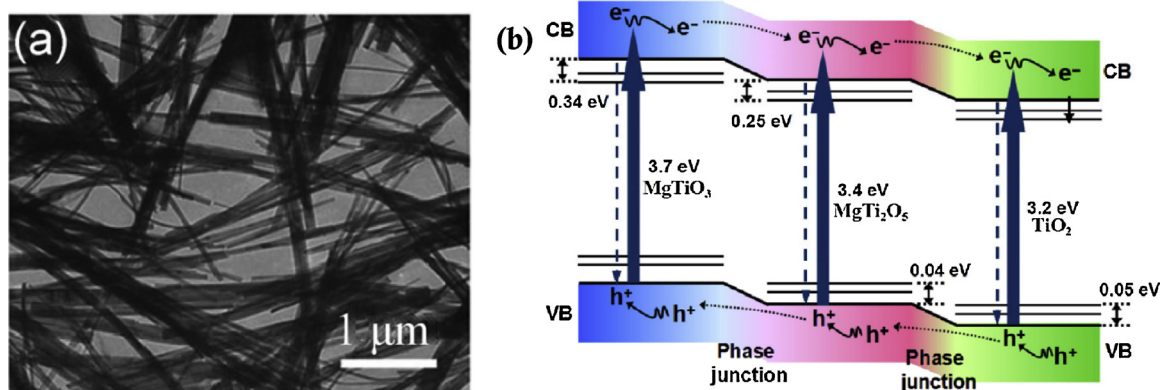
Fig. 57. (a) HRTEM images of $MgTiO_3/MgTi_2O_5/TiO_2$ nano-belts (b) Schematic of the photo-generated electron-hole separation process in the tri-phase heterojunction [308]. Reproduced with permission from ref. [308]. Copyright (2017), Springer Nature.

the general molecular formula of perovskites is ABO_3. Wherein, "A" (*e.g.* rare or alkaline earth metals) and "B" (*e.g.* first row transition metals) are occupied by the large and small cations, respectively. The photocatalytic properties of perovskites are mainly originated form their exceptional crystal structure [291]. Generally, perovskites have a cubic structure (Fig. 54) with a corner-connecting network of BO_6 octahedral ("B" is positioned in the centre) and 12 oxygen coordinated

"A" cations ("A" is located between eight BO_6 octahedral at the middle of the cube). "A" site is weakly bonded with oxygen while the "B" site is strongly bonded to oxygen. The lattice distortion (*via* tilting of octahedra) of ABO_3 relies on the ionic radii and electronegativity of "A" and "B" cations [292].

The crystal structure of various perovskite oxides are displayed in Fig. 55. Different crystalline phases such as rhombohedral, monoclinic,

Fig. 60. (a) Calculated DOS plot of carbonated doped TiO_2 anatase (b) 2D structure of carbonated doped TiO_2 anatase with electron difference density maps (c) Calculated DOS plot of carbonated doped TiO_2 rutile (d) 2D structure of carbonated doped TiO_2 rutile with electron difference density maps (e) Schematic of photocatalytic H_2 evolution on mesoporous carbonate doped TiO_2 nanotubes [342]. Reproduced with permission from ref. [342]. Copyright (2018), Elsevier.

triclinic, orthogonal, and tetragonal are formed through the lattice distortion and the modification of cations [292]. The crystal structure is strongly influenced by the synthesis method. Hydrothermal method is most commonly used to synthesis perovskites due to its less complications and cost effectiveness [294,295].

Titanates with a molecular formula of $ATiO_3$ are widely used as photocatalysts for water splitting reaction. The crystal structure of $ATiO_3$ are modified by replacing the A cations. The rotation of oxygen octahedra has a significant impact on the dipole and electronic band structures of titanates, influencing photo-generated charge carrier separation, migration and transfer [301]. The octahedra rotations directly influence the Ti−O bond length and Ti−O−Ti bond angle due to the relocation of oxygen atoms from the edges [301]. Consequently, the photocatalytic performance of $ATiO_3$ are mainly controlled by Ti 3d orbital and O 2p orbital hybridization. $SrTiO_3$ [302], $BaTiO_3$ [303], $CaTiO_3$ [304], $MgTiO_3$ [305]and $NiTiO_3$ [306] were reported for the photocatalytic H_2 production activity. Various dopants and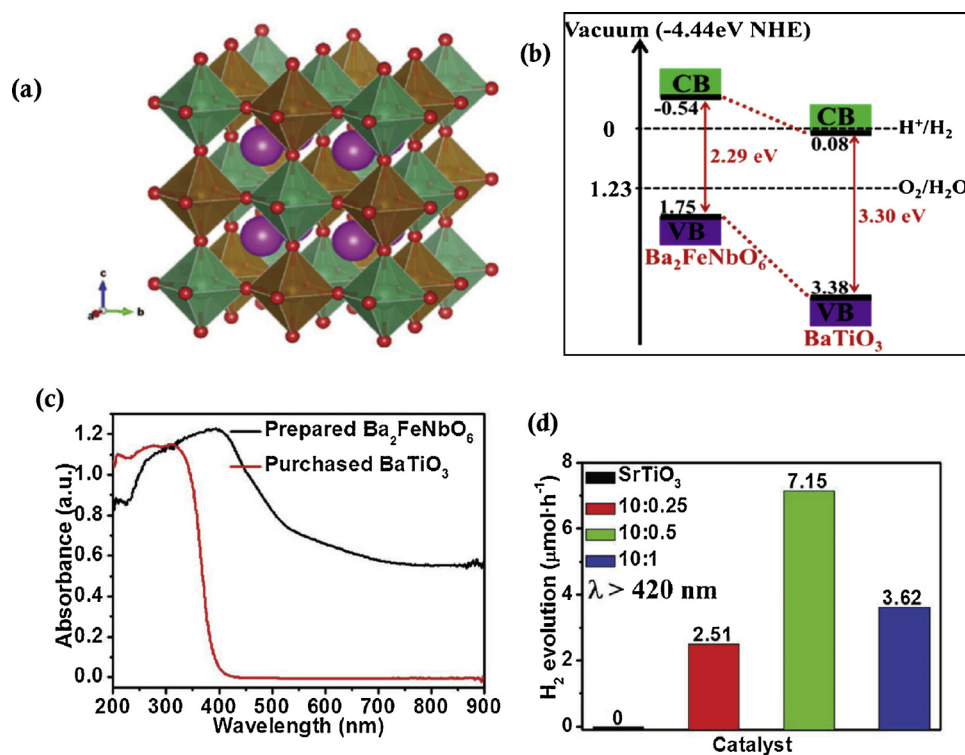 narrow bandgap semiconductors were coupled with these titanates to improve the electron-hole separation process and extend the light absorption. Some of the key findings of recently reported titanates for H_2

production are presented briefly in the following section.

La and Cr (La/Cr) doped hollow $CaTiO_3$ cubes were examined for photocatalytic water splitting [307]. The H_2 production efficiency of La/Cr doped $CaTiO_3$ cubes is higher than that of pure $CaTiO_3$. The peculiar cube morphology of $CaTiO_3$ shortens the charge migration pathway and improves photon-matter interaction (Fig. 56 (a) and (b)). Also, Cr doping induces the formation spin polarized VB inside the original bandgap of $CaTiO_3$ (Fig. 56 (c)).

Meng et al. [308] reported the H_2 production efficiency of a tri-phase ($MgTiO_3/MgTi_2O_5/TiO_2$) hetero-junction with nano-belt morphology under UV light irradiation. H_2 production efficiency of $MgTiO_3/MgTi_2O_5/TiO_2$ (356.1 mol·$g_{0.1gcat}$ h^{-1}) is two times higher than that of pure TiO_2 nano-belts. This is attributed to the maximum light utilization, more active sites, special 1D belt morphology, and high electron-hole separation on the tri-phase hetero-junction (Fig. 57)

In another study, the photocatalytic activity of $SrTiO_3$-Ba_2FeNbO_6 perovskite was evaluated under visible light irradiation [309]. Perovskites with narrow bandgap is constructed by the two different metal cations on the "B" site of ABO_3. It is predicted that Ba_2FeNbO_6 has a similar cubic crystal structure (Ti^{4+} is substituted by Nb^{5+} and Fe^{3+})
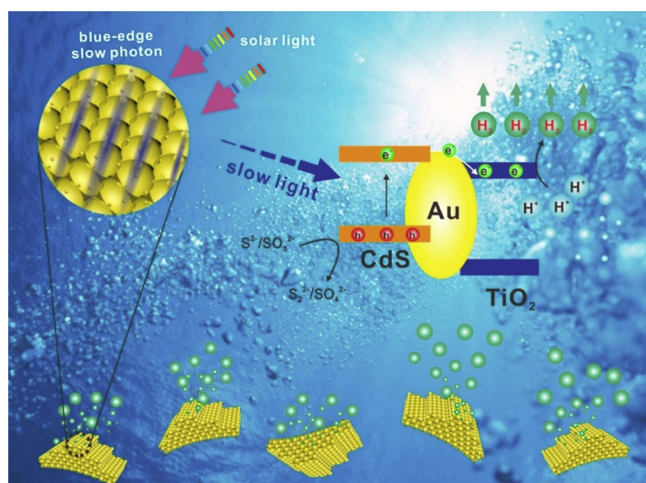
Fig. 61. Schematic of the slow photon effect in the gradient ternary 3DOM TiO_2-Au-CdS photonic crystals for H_2 production under visible light [343]. Reproduced with permission from ref. [343]. Copyright (2018), Elsevier.

like $BaTiO_3$ (Fig. 58(a)). Moreover, Ba_2FeNbO_6 is a narrow bandgap (2.29 eV) photocatalyst with appropriate band edge positions for water splitting. The results also suggested that the elements on the "B" site have a strong influence on the bandgap energy. UV–vis results revealed

that Ba_2FeNbO_6 could absorb maximum visible light when compared to $BaTiO_3$ (Fig. 58(c)). The highest H_2 production efficiency is shown by the nanocomposite of $SrTiO_3$-Ba_2FeNbO_6 with a molar ratio of 10:0.5 (bandgap = 2.92 eV).

In addition to the 2D materials and perovskites, some other novel photocatalysts have also been developed in recent years [187,218,310–340] for H_2 production. The activity of the photocatalysts is enriched by tuning the crystal structure, morphology and electronic properties. The crucial findings of selected TiO_2 photocatalysts are highlighted briefly.

The photocatalytic activity of hierarchical CdS/mesoporous TiO_2/ graphene ternary nano-composite (CdS/m-TiO_2/G) was studied under visible light irradiation [341]. The photocatalyst was synthesized through an electrostatic assembly (negative-positive-negative) technique (Fig. 59(i)). H_2 production efficiency of CdS/m-TiO_2/G is two times higher than that of pure CdS or TiO_2. The electric tri-layer (m-TiO_2/Cd^{2+}/GO) is highly favourable for the photo-stability, uniform dispersion of CdS in the core-shell structure (Fig. 59(ii)) and the strong interfacial binding of CdS/m-TiO_2/G. The photocatalytic activity and charge carrier separation process (Fig. 59(ii)) are enhanced by the atomic-scaled heterojunction. Moreover, nearly 82% of the initial photocatalytic activity is retained after 15 recycle experiments during 80 h of visible light irradiation (Fig. 59(iii)).

In another study, the charge separation and transfer of mesoporous carbonate doped TiO_2 nanotubes (C/TiO_2 NT) was examined for the photocatalytic H_2 production [342]. The photocatalyst was synthesized
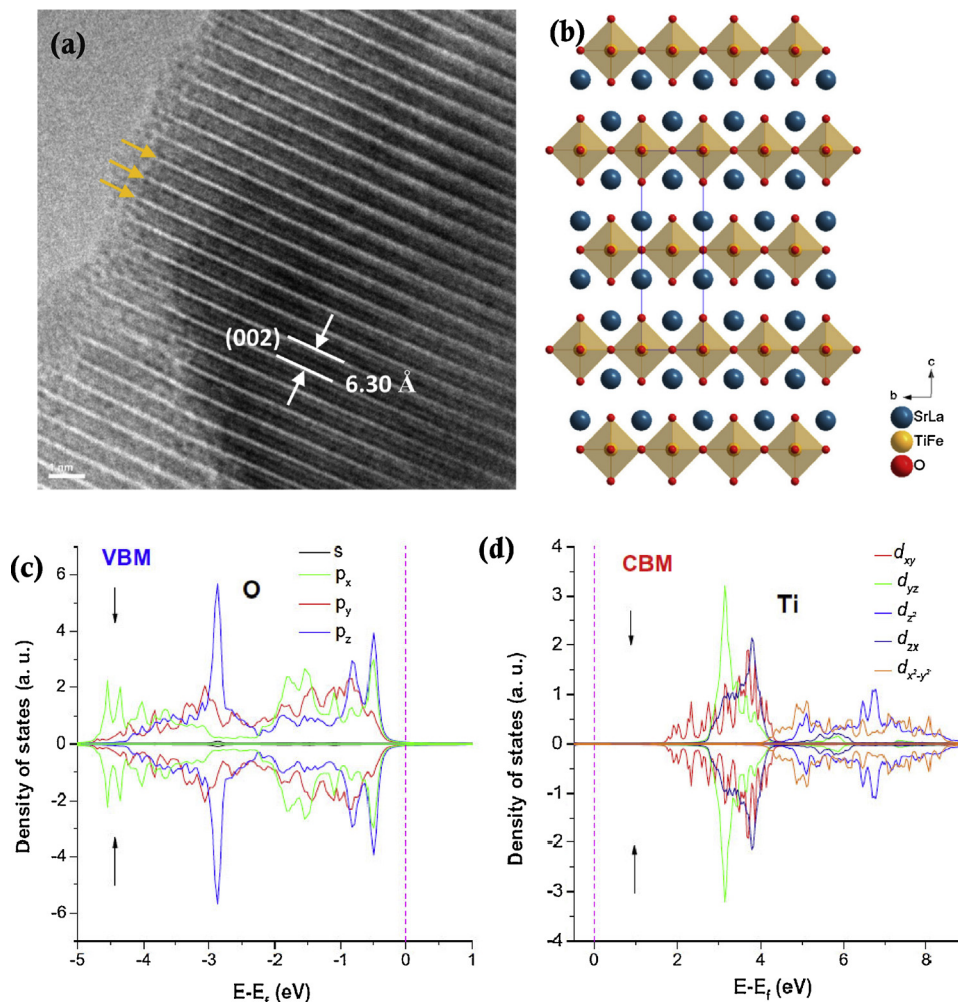
Fig. 62. (a) HR-TEM image of $Sr_{1.9}La_{0.1}Ti_{0.9}Fe_{0.1}O_4$ (b) Lattice fringe corresponds to (002) plane is marked in $Sr_{1.9}La_{0.1}Ti_{0.9}Fe_{0.1}O_4$ crystal structure projected from [100] direction (c) DOS of O 2p orbitals at VBM (d) DOS of Ti 3d orbitals at VBM [344]. Reproduced with permission from ref. [344]. Copyright (2018), Elsevier.

VBM

CBM
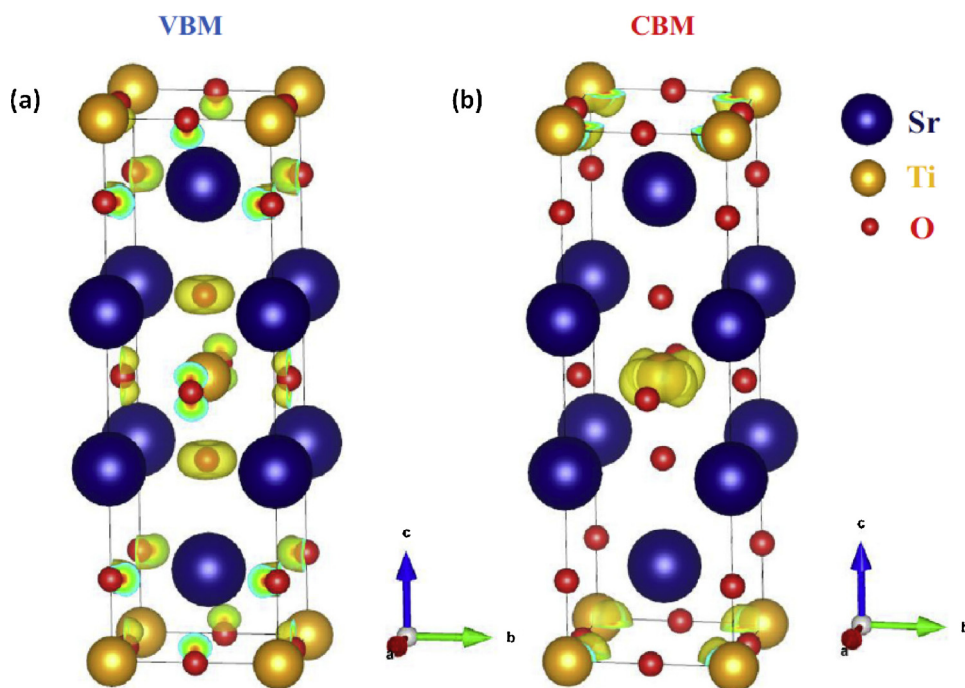
Fig. 63. Decomposed charge density of Sr_2TiO_4 at (a) VBM and (b) CBM of Sr_2TiO_4 [344]. Reproduced with permission from ref. [344]. Copyright (2018), Elsevier.

via an olive oil-assisted electrospinning technique. The efficiency of C/TiO_2 NT is six times (6108 µmol g^{-1} h^{-1}) higher than that of TiO_2 P25. The effect of carbonate doping on the electronic structure of TiO_2 was studied by DFT calculations (generalized gradient approximation with a Hubbard parameter (GGA + U) model). New energy levels are introduced near the CB and VB of TiO_2 by carbonate doping, indicating the bandgap energy is reduced (Fig. 60(a) and (c)). Electron difference density maps suggest that σ bonds are mostly formed through the interaction of C 2*p* and O *sp* orbitals in the deep valance region (Fig. 60(b) and (d)).

The porous architecture is beneficial for effective mass transfer, supply of more active sites and absorption of more light. The optical path length of incident light is increased *via* the multiple reflection effect of the porous architecture (Fig. 60(e)). The transfer and separation of photo-generated charge carriers in the nano-composite are improved by the close homo-junction between anatase and rutile phase TiO_2 (Fig. 60 (e)). The photo-generated electrons on the surface of TiO_2 are rapidly transferred into the active sites *via* the electrostatic force of carbonate dopant.

In another study, the H_2 production efficiency was examined on gradient ternary TiO_2-Au-CdS photonic crystals (materials that can block the light of certain wavelengths/frequencies from propagating any number of polarization directions inside the material) with three dimensionally ordered macro-porous (3DOM) network under visible light irradiation [343]. 3DOM of TiO_2 is beneficial for the strong light penetration and effective mass transfer whereas CdS is responsible for visible light absorption and Au is accountable for the constructive electron transfer. The enhanced H_2 production efficiency of TiO_2-Au-CdS is attributed to the slow photon effect (a structural effect that could generate more charge carriers) of photonic crystals (Fig. 61). Slow photon effect is achieved by tuning the macro-pore size of the 3D skeleton to match the photonic bandgap (energy at the blue-edge and/or red edge) of TiO_2-Au-CdS with the electronic bandgap energy of CdS. The optical path length of photons is increased when the blue edge or red edge photons overlap with the electronic bandgap of CdS. The slow photons at the blue edge (higher frequency edge) display maximum H_2 production efficiency, compared to that of red edge (lower frequency edge). This indicates that photons with high energy are required to

increase the formation of charge carriers.

Zhang et al. developed a Ruddlesden-Popper compound Sr_2TiO_4 (layered semiconductor) co-doped with La and Fe for efficient photocatalytic hydrogen production [344]. The effect of doping was investigated on the crystal structure, morphology and optical properties. H_2 production efficiency of $Sr_{1.9}La_{0.1}Ti_{0.9}Fe_{0.1}O_4$ is five times (~106.2 µmol/h) higher than that of pristine Sr_2TiO_4 under UV–vis light irradiation. The unit cell of Sr_2TiO_4 is slightly expanded after doping with La and Fe. The lattice fringe (~6.30 Å) of $Sr_{1.9}La_{0.1}Ti_{0.9}Fe_{0.1}O_4$ is matched well with the (002) plane along '*c*' direction (Fig. 62(a) and (b)). DFT calculations reveal that two spin-polarized bands are introduced in Sr_2TiO_4 by Fe doping. DOS results show that the CBM and VBM of Sr2TiO4 are dominated by Ti 3d_{xy} and O 2 p_z/2 p_x orbitals (Fig. 62(c)). The VBM and CBM of Sr_2TiO_4 are exclusively concealed (Fig. 63) in the TiO_6 octahedron layer, which can provide 2D or anisotropic charge transportation properties to Sr_2TiO_4. This is highly effective in prohibiting the photo-generated charge carrier recombination process.

6. Summary and outlook

In this review, we summarize the significant perspectives of metal-doped TiO_2 for photocatalytic H_2 production. Loading of metal dopants on TiO_2 is shown to be a promising route to enhance the charge-carrier separation on the catalyst surface and red shift the absorption maxima to the visible region. The outer shell electronic configuration and atomic radius of metal dopants should be considered for selecting the dopants. Pt (*via* Schottky barrier formation), Au and Cu (*via* SPR) have proved as effective electron traps to amplify the H_2 production efficiency of TiO_2 owing to their high work function. H_2 production yield and the electron transfer mechanism of dopants are strongly ruled by the nature of light irradiation source such as UV, visible and UV–vis or simulated solar light. The kinetics and mechanism of metal-doped TiO_2 have been reviewed in detail. Langmuir-Hinshelwood (LH) is the most widely used model to express the rate of H_2 production using metal-doped TiO_2 photocatalyst. It is noted that most of the recent studies for TiO_2 water splitting have been performed using bimetallic dopants. Simulated solar light or UV–vis light with bimetallic dopants (metal/

metal or metal/non-metal) are the foremost choice to achieve maximum H_2 production efficiency for TiO_2. Also, 2D materials and perovskites have been used as photocatalysts in recent years to improve the H_2 generation rate. Feasible photo-reactor designs for the lab scale and piolet scale for H_2 production are discussed.

However, there is still no clear information on the design of a photo-reactor to evaluate the H_2 production efficiency. Almost all the research studies have been executed at laboratory scale using custom-made micro reactors in the range of 50–100 ml with various headspace volumes. There are no transparent knowledge on data (efficiency) interpretation from the GC measurement during the experiments. The efficiency may raise if we use more headspace volume in our reactions. Several investigations need to be carried out in the future to enrich the photocatalytic H_2 production at the pilot scale under natural sunlight. Steps should also be taken for commercialization of this technology. Numerous metal and non-metal dopants have been reported to amplify the H_2 production efficiency of TiO_2. Conversely, there are no suitable alternatives still today to replace the very expensive Pt and Au dopants to achieve maximum quantum efficiency. From the economic point of view, the development of cost effective photocatalysts is still a great challenge. Because very expensive dopants and toxic sacrificial agents (*e.g.* alcohols, amines, sulphides) have been used in ultrapure water to produce H_2 gas in the range of μL to mL. There is no standard rule available to select a sacrificial agent and fix its concentration for an oxide, carbon and sulfide photocatalyst. Future studies in water splitting should be focused on the following aspects; thermally stable photocatalysts, use of inexpensive materials, non-toxic/*in-situ* sacrificial agents, non-sacrificial H_2 production and using of industrial effluent/wastewater/seawater. More studies should also be carried out to understand the kinetics of metal-doped TiO_2 for water splitting. Standards such as ISO, ASTM, and JIS to validate the H_2 production efficiency of photocatalysts should be developed. In the current scenario, theoretical or computational modelling (*e.g.* DFT) is a mandate to fabricate a photocatalyst with more active sites, utmost light harvesting property, sufficient crystal defects, required crystalline phases, suitable electronic properties, high surface area, and limited charge carrier recombination centres. Therefore, the combination of theoretical and experimental studies will be the optimal approach to understand the basic principles behind the H_2 production efficiency of metal-doped TiO_2.

Acknowledgements

References

[1] N. Armaroli, V. Balzani, Towards an electricity-powered world, Energy Environ. Sci. 4 (2011) 3193–3222.

[2] M. Höök, X. Tang, Depletion of fossil fuels and anthropogenic climate change–a review, Energy Policy 52 (2013) 797–809.

[3] S. Shafiee, E. Topal, When will fossil fuel reserves be diminished? Energy Policy 37 (2009) 181–189.

[4] M.G. Walter, E.L. Warren, J.R. McKone, S.W. Boettcher, Q. Mi, E.A. Santori, N.S. Lewis, Solar water splitting cells, Chem. Rev. 110 (2010) 6446–6473.

[5] M.R. Hoffmann, S.T. Martin, W. Choi, D.W. Bahnemann, Environmental applications of semiconductor photocatalysis, Chem. Rev. 95 (1995) 69–96.

[6] A. Fujishima, K. Honda, Electrochemical photolysis of water at a semiconductor electrode, Nature 238 (1972) 37.

[7] Z. Zou, J. Ye, K. Sayama, H. Arakawa, Direct splitting of water under visible light irradiation with an oxide semiconductor photocatalyst, Nature 414 (2001) 625.

[8] H. Wang, L. Zhang, Z. Chen, J. Hu, S. Li, Z. Wang, J. Liu, X. Wang, Semiconductor heterojunction photocatalysts: design, construction, and photocatalytic performances, Chem. Soc. Rev. 43 (2014) 5234–5244.

[9] X. Chen, S. Shen, L. Guo, S.S. Mao, Semiconductor-based photocatalytic hydrogen generation, Chem. Rev. 110 (2010) 6503–6570.

[10] X. An, C. Hu, H. Liu, J. Qu, Hierarchical nanotubular anatase/rutile/TiO2 (B)

[11] heterophase junction with oxygen vacancies for enhanced photocatalytic H2 production, Langmuir 34 (2018) 1883–1889.

[11] C. Zhang, Y. Zhou, J. Bao, Y. Zhang, J. Fang, S. Zhao, W. Chen, X. Sheng, Sn2 + -Doped double-shelled TiO2 hollow nanospheres with minimal Pt content for significantly enhanced solar H2 production, ACS Sustain. Chem. Eng. 6 (2018) 7128–7137.

[12] A.S. Hainer, J.S. Hodgins, V. Sandre, M. Vallieres, A.E. Lanterna, J.C. Scaiano, Photocatalytic hydrogen generation using metal-decorated TiO2: sacrificial donors vs true water splitting, ACS Energy Lett. 3 (2018) 542–545.

[13] Q. Xu, B. Cheng, J. Yu, G. Liu, Making co-condensed amorphous carbon/g-C3N4 composites with improved visible-light photocatalytic H2-production performance using Pt as cocatalyst, Carbon 118 (2017) 241–249.

[14] W.-K. Jo, N.C.S. Selvam, Z-scheme CdS/g-C3N4 composites with RGO as an electron mediator for efficient photocatalytic H2 production and pollutant degradation, Chem. Eng. J. 317 (2017) 913–924.

[15] X. Liu, P. Wang, H. Zhai, Q. Zhang, B. Huang, Z. Wang, Y. Liu, Y. Dai, X. Qin, X. Zhang, Synthesis of synergetic phosphorus and cyano groups (CN) modified g-C3N4 for enhanced photocatalytic H2 production and CO2 reduction under visible light irradiation, Appl. Catal. B 232 (2018) 521–530.

[16] F. Vaquero, R. Navarro, J. Fierro, Influence of the solvent on the structure, morphology and performance for H2 evolution of CdS photocatalysts prepared by solvothermal method, Appl. Catal. B 203 (2017) 753–767.

[17] M. Zhang, H. Lin, J. Cao, X. Guo, S. Chen, Construction of novel S/CdS type II heterojunction for photocatalytic H2 production under visible light: the intrinsic positive role of elementary α-S, Chem. Eng. J. 321 (2017) 484–494.

[18] N. Qin, J. Xiong, R. Liang, Y. Liu, S. Zhang, Y. Li, Z. Li, L. Wu, Highly efficient photocatalytic H2 evolution over MoS2/CdS-TiO2 nanofibers prepared by an electrospinning mediated photodeposition method, Appl. Catal. B 202 (2017) 374–380.

[19] G.M. Haselmann, D. Eder, Early-stage deactivation of platinum-loaded TiO2 using in situ photodeposition during photocatalytic hydrogen evolution, ACS Catal. 7 (2017) 4668–4675.

[20] A. Tiwari, N. Vamsi Krishna, L. Giribabu, U. Pal, Hierarchical porous TiO2 embedded unsymmetrical Zn-Phthalocyanine sensitizer for visible-light-Induced photocatalytic H2 production, J. Phys. Chem. C 122 (2017) 495–502.

[21] J. Guayaquil-Sosa, B. Serrano-Rosales, P. Valadés-Pelayo, H. de Lasa, Photocatalytic hydrogen production using mesoporous TiO2 doped with Pt, Appl. Catal. B 211 (2017) 337–348.

[22] H.-J. Hou, X.-H. Zhang, D.-K. Huang, X. Ding, S.-Y. Wang, X.-L. Yang, S.-Q. Li, Y.-G. Xiang, H. Chen, Conjugated microporous poly (benzothiadiazole)/TiO2 heterojunction for visible-light-driven H2 production and pollutant removal, Appl. Catal. B 203 (2017) 563–571.

[23] T.W. Seadira, G. Sadanandam, T. Ntho, C.M. Masuku, M.S. Scurrell, Preparation and characterization of metals supported on nanostructured TiO2 hollow spheres for production of hydrogen via photocatalytic reforming of glycerol, Appl. Catal. B 222 (2018) 133–145.

[24] N. Murakami, T. Chiyoya, T. Tsubota, T. Ohno, Switching redox site of photocatalytic reaction on titanium (IV) oxide particles modified with transition-metal ion controlled by irradiation wavelength, Appl. Catal. A Gen. 348 (2008) 148–152.

[25] S. Agrawal, N.J. English, K.R. Thampi, J. MacElroy, Perspectives on ab initio molecular simulation of excited-state properties of organic dye molecules in dye-sensitised solar cells, J. Chem. Soc. Faraday Trans. 14 (2012) 12044–12056.

[26] M.R. Gholipour, C.-T. Dinh, F. Béland, T.-O. Do, Nanocomposite heterojunctions as sunlight-driven photocatalysts for hydrogen production from water splitting, Nanoscale 7 (2015) 8187–8208.

[27] A.A. Ismail, D.W. Bahnemann, Photochemical splitting of water for hydrogen production by photocatalysis: a review, Sol. Energy Mater. Sol. Cells 128 (2014) 85–101.

[28] J. Schneider, M. Matsuoka, M. Takeuchi, J. Zhang, Y. Horiuchi, M. Anpo, D.W. Bahnemann, Understanding TiO2 photocatalysis: mechanisms and materials, Chem. Rev. 114 (2014) 9919–9986.

[29] M. Bowker, Sustainable hydrogen production by the application of ambient temperature photocatalysis, Green Chem. 13 (2011) 2235–2246.

[30] Y. Miseki, S. Fujiyoshi, T. Gunji, K. Sayama, Photocatalytic Z-scheme water splitting for independent H2/O2 production via a stepwise operation employing a vanadate redox mediator under visible light, J. Phys. Chem. C 121 (2017) 9691–9697.

[31] O. Elbanna, S. Kim, M. Fujitsuka, T. Majima, TiO2 mesocrystals composited with gold nanorods for highly efficient visible-NIR-photocatalytic hydrogen production, Nano Energy 35 (2017) 1–8.

[32] L. Yang, J. Huang, L. Shi, L. Cao, Q. Yu, Y. Jie, J. Fei, H. Ouyang, J. Ye, A surface modification resultant thermally oxidized porous g-C3N4 with enhanced photocatalytic hydrogen production, Appl. Catal. B 204 (2017) 335–345.

[33] L. Bi, X. Gao, L. Zhang, D. Wang, X. Zou, T. Xie, Enhanced photocatalytic hydrogen evolution of NiCoP/g-C3N4 with improved separation efficiency and charge transfer efficiency, ChemSusChem 11 (2018) 276–284.

[34] J. Ran, G. Gao, F.-T. Li, T.-Y. Ma, A. Du, S.-Z. Qiao, Ti 3 C 2 MXene co-catalyst on metal sulfide photo-absorbers for enhanced visible-light photocatalytic hydrogen production, Nat. Commun. 8 (2017) 13907.

[35] Y. Chang, K. Yu, C. Zhang, Z. Yang, Y. Feng, H. Hao, Y. Jiang, L.-L. Lou, W. Zhou, S. Liu, Ternary CdS/Au/3DOM-SrTiO3 composites with synergistic enhancement for hydrogen production from visible-light photocatalytic water splitting, Appl. Catal. B 215 (2017) 74–84.

[36] W. Ouyang, M.J. Munoz-Batista, A. Kubacka, R. Luque, M. Fernández-García, Enhancing photocatalytic performance of TiO2 in H2 evolution via Ru co-catalyst deposition, Appl. Catal. B 238 (2018) 434–443.

[37] O. Fontelles-Carceller, M.J. Muñoz-Batista, E. Rodríguez-Castellón, J.C. Conesa, M. Fernández-García, A. Kubacka, Measuring and interpreting quantum efficiency for hydrogen photo-production using Pt-titania catalysts, J. Catal. 347 (2017) 157–169.

[38] M.J. Muñoz-Batista, D. Motta Meira, G. Colón, A. Kubacka, M. Fernández-García, Phase-contact engineering in mono-and bimetallic Cu-Ni Co-catalysts for hydrogen photocatalytic materials, Angew. Chem. Int. Ed. 57 (2018) 1199–1203.

[39] U. Caudillo-Flores, M.J. Muñoz-Batista, J.A. Cortés, M. Fernández-García, A. Kubacka, UV and visible light driven H2 photo-production using Nb-doped TiO2: Comparing Pt and Pd co-catalysts, Mol. Catal. 437 (2017) 1–10.

[40] O. Fontelles-Carceller, M.J. Muñoz-Batista, J.C. Conesa, M. Fernández-García, A. Kubacka, UV and visible hydrogen photo-production using Pt promoted Nb-doped TiO2 photo-catalysts: interpreting quantum efficiency, Appl. Catal. B 216 (2017) 133–145.

[41] S. Obregón, M.J. Munoz-Batista, M. Fernández-García, A. Kubacka, G. Colón, Cu–TiO2 systems for the photocatalytic H2 production: influence of structural and surface support features, Appl. Catal. B 179 (2015) 468–478.

[42] J. Liu, Y. Liu, N. Liu, Y. Han, X. Zhang, H. Huang, Y. Lifshitz, S.-T. Lee, J. Zhong, Z.J.S. Kang, Metal-free efficient photocatalyst for stable visible water splitting via a two-electron pathway, Science 347 (2015) 970–974.

[43] O. Micic, Y. Zhang, K.R. Cromack, A. Trifunac, D.M. Thurnauer, Photoinduced hole transfer from titanium dioxide to methanol molecules in aqueous solution studied by electron paramagnetic resonance, J. Phys. Chem. 97 (1993) 13284–13288.

[44] A. Yamakata, T.-a. Ishibashi, H. Onishi, Electron-and hole-capture reactions on Pt/TiO2 photocatalyst exposed to methanol vapor studied with time-resolved infrared absorption spectroscopy, J. Phys. Chem. B 106 (2002) 9122–9125.

[45] J.Ø. Hansen, R. Bebensee, U. Martinez, S. Porsgaard, E. Lira, Y. Wei, L. Lammich, Z. Li, H. Idriss, F. Besenbacher, Unravelling site-specific photo-reactions of ethanol on rutile TiO2 (110), Sci. Rep. 6 (2016) 21990.

[46] N. Murakami, A. Ono, M. Nakamura, T. Tsubota, T. Ohno, Development of a visible-light-responsive rutile rod by site-selective modification of iron (III) ion on {1 1 1} exposed crystal faces, Appl. Catal. B 97 (2010) 115–119.

[47] M. Nakamura, A. Ono, E. Bae, N. Murakami, T. Ohno, Improvement of visible light responsivity of rutile TiO2 nanorods by site-selective modification of iron (III) ion on newly exposed faces formed by chemical etching treatment, Appl. Catal. B 130 (2013) 264–269.

[48] R. Abe, Recent progress on photocatalytic and photoelectrochemical water splitting under visible light irradiation, J. Photochem. Photobiol. C Photochem. Rev. 11 (2010) 179–209.

[49] F. Fresno, R. Portela, S. Suárez, J.M. Coronado, Photocatalytic materials: recent achievements and near future trends, J. Mater. Chem. A 2 (2014) 2863–2884.

[50] A. Samokhvalov, Hydrogen by photocatalysis with nitrogen codoped titanium dioxide, Renew. Sustain. Energy Rev. 72 (2017) 981–1000.

[51] F. Wang, R.J. Wong, J.H. Ho, Y. Jiang, R. Amal, Sensitization of Pt/TiO2 using plasmonic Au nanoparticles for hydrogen evolution under visible-light irradiation, ACS Appl. Mater. Interfaces 9 (2017) 30575–30582.

[52] M.D. Brady, R.N. Sampaio, D. Wang, T.J. Meyer, G.J. Meyer, Dye-sensitized hydrobromic acid splitting for hydrogen solar fuel production, J. Am. Chem. Soc. 139 (2017) 15612–15615.

[53] S.N.H. Jaafar, L.J. Minggu, K. Arifin, M.B. Kassim, W.R.D. Wan, Natural dyes as TIO2 sensitizers with membranes for photoelectrochemical water splitting: an overview, Renew. Sustain. Energy Rev. 78 (2017) 698–709.

[54] Y. Lu, B. Ma, Y. Yang, E. Huang, Z. Ge, T. Zhang, S. Zhang, L. Li, N. Guan, Y. Ma, High activity of hot electrons from bulk 3D graphene materials for efficient photocatalytic hydrogen production, Nano Res. 10 (2017) 1662–1672.

[55] Q. Lang, Y. Chen, T. Huang, L. Yang, S. Zhong, L. Wu, J. Chen, S. Bai, Graphene "bridge" in transferring hot electrons from plasmonic Ag nanocubes to TiO2 nanosheets for enhanced visible light photocatalytic hydrogen evolution, Appl. Catal. B 220 (2018) 182–190.

[56] W. Mulewa, M. Tahir, N.A.S. Amin, MMT-supported Ni/TiO2 nanocomposite for low temperature ethanol steam reforming toward hydrogen production, Chem. Eng. J. 326 (2017) 956–969.

[57] X. Xing, M. Zhang, L. Hou, L. Xiao, Q. Li, J. Yang, Z-scheme BCN-TiO2 nanocomposites with oxygen vacancy for high efficiency visible light driven hydrogen production, Int. J. Hydrogen Energy 42 (2017) 28434–28444.

[58] M.J. Muñoz-Batista, D. Rodríguez-Padrón, A.R. Puente-Santiago, A. Kubacka, R. Luque, M.J.C. Fernández-García, Sunlight-driven hydrogen production using an annular flow photoreactor and g-C3N4-based catalysts, ChemPhotoChem 2 (2018) 870–877.

[59] J.B. Priebe, Jr. Radnik, A.J. Lennox, M.-M. Pohl, M. Karnahl, D. Hollmann, K. Grabow, U. Bentrup, H. Junge, M. Beller, Solar hydrogen production by plasmonic Au–TiO2 catalysts: impact of synthesis protocol and TiO2 phase on charge transfer efficiency and H2 evolution rates, ACS Catal. 5 (2015) 2137–2148.

[60] J. Bharatvaj, V. Preethi, S. Kanmani, Hydrogen production from sulphide wastewater using Ce 3+–TiO 2 photocatalysis, Int. J. Hydrogen Energy (2018).

[61] V. Nichele, M. Signoretto, F. Menegazzo, A. Gallo, G. Dal Santo, G. Cruciani, G. Cerrato, Glycerol steam reforming for hydrogen production: design of Ni supported catalysts, Appl. Catal. B 111 (2012) 225–232.

[62] B. Liu, S. Su, W. Zhou, Y. Wang, D. Wei, L. Yao, Y. Ni, M. Cao, C. Hu, Photoreduction assisted synthesis of W-doped TiO 2 coupled with Au nanoparticles for highly efficient photocatalytic hydrogen evolution, CrystEngComm 19 (2017) 675–683.

[63] S. Sun, P. Gao, Y. Yang, P. Yang, Y. Chen, Y. Wang, N-doped TiO2 nanobelts with coexposed (001) and (101) facets and their highly efficient visible-light-driven photocatalytic hydrogen production, ACS Appl. Mater. Interfaces 8 (2016) 18126–18131.

[64] M.-C. Wu, J. Hiltunen, As. Sápi, A. Avila, W. Larsson, H.-C. Liao, M. Huuhtanen, Gz. Tóth, A. Shchukarev, Nm. Laufer, Nitrogen-doped anatase nanofibers decorated with noble metal nanoparticles for photocatalytic production of hydrogen, ACS Nano 5 (2011) 5025–5030.

[65] J.H. Park, S. Kim, A.J. Bard, Novel carbon-doped TiO2 nanotube arrays with high aspect ratios for efficient solar water splitting, Nano Lett. 6 (2006) 24–28.

[66] S.K. Parayil, H.S. Kibombo, C.-M. Wu, R. Peng, J. Baltrusaitis, R.T. Koodali, Enhanced photocatalytic water splitting activity of carbon-modified TiO2 composite materials synthesized by a green synthetic approach, Int. J. Hydrogen Energy 37 (2012) 8257–8267.

[67] J. Yuan, M. Chen, J. Shi, W. Shangguan, Preparations and photocatalytic hydrogen evolution of N-doped TiO2 from urea and titanium tetrachloride, Int. J. Hydrogen Energy 31 (2006) 1326–1331.

[68] K. Villa, A. Black, X. Domenech, J. Peral, Nitrogen doped TiO2 for hydrogen production under visible light irradiation, Sol. Energy 86 (2012) 558–566.

[69] R. Sasikala, A. Shirole, V. Sudarsan, C. Sudakar, R. Naik, R. Rao, S. Bharadwaj, Enhanced photocatalytic activity of indium and nitrogen co-doped TiO2–Pd nanocomposites for hydrogen generation, Appl. Catal. A Gen. 377 (2010) 47–54.

[70] T. Sreethawong, S. Laehsalee, S. Chavadej, Comparative investigation of mesoporous-and non-mesoporous-assembled TiO2 nanocrystals for photocatalytic H2 production over N-doped TiO2 under visible light irradiation, Int. J. Hydrogen Energy 33 (2008) 5947–5957.

[71] Q. Xiang, J. Yu, W. Wang, M. Jaroniec, Nitrogen self-doped nanosized TiO 2 sheets with exposed {001} facets for enhanced visible-light photocatalytic activity, Chem. Commun. 47 (2011) 6906–6908.

[72] C. Wang, Q.-Q. Hu, J.-Q. Huang, Z.-H. Deng, H.-L. Shi, L. Wu, Z.-G. Liu, Y.-G. Cao, Effective water splitting using N-doped TiO2 films: role of preferred orientation on hydrogen production, Int. J. Hydrogen Energy 39 (2014) 1967–1971.

[73] C. Yang, Z. Wang, T. Lin, H. Yin, X. Lü, D. Wan, T. Xu, C. Zheng, J. Lin, F. Huang, Core-shell nanostructured "black" rutile titania as excellent catalyst for hydrogen production enhanced by sulfur doping, J. Am. Chem. Soc. 135 (2013) 17831–17838.

[74] G.L. Chiarello, M.V. Dozzi, M. Scavini, J.-D. Grunwaldt, E. Selli, One step flame-made fluorinated Pt/TiO2 photocatalysts for hydrogen production, Appl. Catal. B 160 (2014) 144–151.

[75] F. Zuo, L. Wang, T. Wu, Z. Zhang, D. Borchardt, P. Feng, Self-doped Ti3+ enhanced photocatalyst for hydrogen production under visible light, J. Am. Chem. Soc. 132 (2010) 11856–11857.

[76] R. Sasikala, V. Sudarsan, C. Sudakar, R. Naik, L. Panicker, S. Bharadwaj, Modification of the photocatalytic properties of self doped TiO2 nanoparticles for hydrogen generation using sunlight type radiation, Int. J. Hydrogen Energy 34 (2009) 6105–6113.

[77] Y. Wu, G. Lu, S. Li, The doping effect of Bi on TiO2 for photocatalytic hydrogen generation and photodecolorization of rhodamine B, J. Phys. Chem. C 113 (2009) 9950–9955.

[78] Y.H. Hu, A highly efficient photocatalyst—hydrogenated black TiO2 for the photocatalytic splitting of water, Angew. Chem. Int. Ed. 51 (2012) 12410–12412.

[79] W. Zhou, W. Li, J.-Q. Wang, Y. Qu, Y. Yang, Y. Xie, K. Zhang, L. Wang, H. Fu, D. Zhao, Ordered mesoporous black TiO2 as highly efficient hydrogen evolution photocatalyst, J. Am. Chem. Soc. 136 (2014) 9280–9283.

[80] F.N. Sayed, O. Jayakumar, R. Sasikala, R. Kadam, S.R. Bharadwaj, L. Kienle, U. Schürmann, Sr. Kaps, R. Adelung, J. Mittal, Photochemical hydrogen generation using nitrogen-doped TiO2–Pd nanoparticles: facile synthesis and effect of Ti3+ incorporation, J. Phys. Chem. C 116 (2012) 12462–12467.

[81] H. Bahruji, M. Bowker, P.R. Davies, F. Pedrono, New insights into the mechanism of photocatalytic reforming on Pd/TiO2, Appl. Catal. B 107 (2011) 205–209.

[82] M.-S. Park, M. Kang, The preparation of the anatase and rutile forms of Ag–TiO2 and hydrogen production from methanol/water decomposition, Mater. Lett. 62 (2008) 183–187.

[83] T. Sun, E. Liu, J. Fan, X. Hu, F. Wu, W. Hou, Y. Yang, L. Kang, High photocatalytic activity of hydrogen production from water over Fe doped and Ag deposited anatase TiO2 catalyst synthesized by solvothermal method, Chem. Eng. J. 228 (2013) 896–906.

[84] E. Bae, W. Choi, Effect of the anchoring group (carboxylate vs phosphonate) in Ru-complex-sensitized TiO2 on hydrogen production under visible light, J. Phys. Chem. B 110 (2006) 14792–14799.

[85] D. Jing, Y. Zhang, L. Guo, Study on the synthesis of Ni doped mesoporous TiO2 and its photocatalytic activity for hydrogen evolution in aqueous methanol solution, Chem. Phys. Lett. 415 (2005) 74–78.

[86] G. Sadanandam, K. Lalitha, V.D. Kumari, M.V. Shankar, M. Subrahmanyam, Cobalt doped TiO2: a stable and efficient photocatalyst for continuous hydrogen production from glycerol: water mixtures under solar light irradiation, Int. J. Hydrogen Energy 38 (2013) 9655–9664.

[87] H.-y. Lin, C.-y. Shih, Efficient one-pot microwave-assisted hydrothermal synthesis of M (M = Cr, Ni, Cu, Nb) and nitrogen co-doped TiO2 for hydrogen production by photocatalytic water splitting, J. Mol. Catal. A Chem. 411 (2016) 128–137.

[88] J. Yu, Y. Hai, B. Cheng, Enhanced photocatalytic H2-production activity of TiO2 by Ni (OH) 2 cluster modification, J. Phys. Chem. C 115 (2011) 4953–4958.

[89] Y. Li, G. Ma, S. Peng, G. Lu, S. Li, Boron and nitrogen co-doped titania with enhanced visible-light photocatalytic activity for hydrogen evolution, Appl. Surf. Sci. 254 (2008) 6831–6836.

[90] V. Nichele, M. Signoretto, F. Menegazzo, I. Rossetti, G. Cruciani, Hydrogen production by ethanol steam reforming: effect of the synthesis parameters on the activity of Ni/TiO2 catalysts, Int. J. Hydrogen Energy 39 (2014) 4252–4258.

[91] Y. Wu, G. Lu, S. Li, The doping effect of Bi on TiO2 for photocatalytic hydrogen

generation and photodecolorization of rhodamine B, J. Phys. Chem. C 113 (2009) 9950–9955.

[92] S. Peng, Y. Li, F. Jiang, G. Lu, S. Li, Effect of Be2+ doping TiO2 on its photo-catalytic activity, Chem. Phys. Lett. 398 (2004) 235–239.

[93] H. Luo, T. Takata, Y. Lee, J. Zhao, K. Domen, Y. Yan, Photocatalytic activity enhancing for titanium dioxide by co-doping with bromine and chlorine, Chem. Mater. 16 (2004) 846–849.

[94] K. Maeda, Rhodium-doped barium titanate perovskite as a stable p-Type semiconductor photocatalyst for hydrogen evolution under visible light, ACS Appl. Mater. Interfaces 6 (2014) 2167–2173.

[95] R. Sasikala, V. Sudarsan, C. Sudakar, R. Naik, T. Sakuntala, S. Bharadwaj, Enhanced photocatalytic hydrogen evolution over nanometer sized Sn and Eu doped titanium oxide, Int. J. Hydrogen Energy 33 (2008) 4966–4973.

[96] L. Li, G. Rohrer, P. Salvador, Heterostructured Ceramic Powders for Photocatalytic Hydrogen Production: Nanostructured TiO2 Shells Surrounding Microcrystalline (Ba,Sr)TiO3 Cores, J. Am. Ceram. Soc. 95 (2012) 1414–1420.

[97] M.K. Kumar, K. Bhavani, B. Srinivas, S.N. Kumar, M. Sudhakar, G. Naresh, A. Venugopal, Nano structured bismuth and nitrogen co-doped TiO2 as an efficient light harvesting photocatalyst under natural sunlight for the production of H2 by H2O splitting, Appl. Catal. A Gen. 515 (2016) 91–100.

[98] W. Zhao, X. Wang, H. Sang, K. Wang, Synthesis of Bi-doped TiO2 nanotubes and enhanced photocatalytic activity for hydrogen evolution from glycerol solution, Chin. J. Chem. 31 (2013) 415–420.

[99] M.-C. Wu, J.-S. Chih, W.-K. Huang, Bismuth doping effect on TiO2 nanofibres for morphological change and photocatalytic performance, CrystEngComm 16 (2014) 10692–10699.

[100] C. HUANG, Y. Wansheng, D. Liqin, L. Zhibin, S. Zhengang, L. ZHANG, Effect of Nd3+ doping on photocatalytic activity of TiO2 nanoparticles for water decomposition to hydrogen, Chin. J. Catal. 27 (2006) 203–209.

[101] J. Yu, L. Qi, M. Jaroniec, Hydrogen production by photocatalytic water splitting over Pt/TiO2 nanosheets with exposed (001) facets, J. Phys. Chem. C 114 (2010) 13118–13125.

[102] W.-C. Lin, W.-D. Yang, I.-L. Huang, T.-S. Wu, Z.-J. Chung, Hydrogen production from Methanol/Water photocatalytic decomposition using Pt/TiO2− x N x catalyst, Energy Fuels 23 (2009) 2192–2196.

[103] D. Tristantini, M. Ibadurrohman, Photocatalytic hydrogen production from glycerol–water mixture over Pt-N-TiO2 nanotube photocatalyst, Int. J. Energy Res. 37 (2013) 1372–1381.

[104] T. Sreethawong, S. Laehsalee, S. Chavadej, Use of Pt/N-doped mesoporous-assembled nanocrystalline TiO2 for photocatalytic H2 production under visible light irradiation, Catal. Commun. 10 (2009) 538–543.

[105] Y. Yang, C.-H. Chang, H. Idriss, Photo-catalytic production of hydrogen form ethanol over M/TiO2 catalysts (M= Pd, Pt or Rh), Appl. Catal. B 67 (2006) 217–222.

[106] T. Chen, Z. Feng, G. Wu, J. Shi, G. Ma, P. Ying, C. Li, Mechanistic studies of photocatalytic reaction of methanol for hydrogen production on Pt/TiO2 by in situ Fourier transform IR and time-resolved IR spectroscopy, J. Phys. Chem. C 111 (2007) 8005–8014.

[107] A. Galińska, J. Walendziewski, Photocatalytic water splitting over Pt− TiO2 in the presence of sacrificial reagents, Energy Fuels 19 (2005) 1143–1147.

[108] J. Guayaquil-Sosa, A. Calzada, B. Serrano, S. Escobedo, H.J.C. de Lasa, Hydrogen production via water dissociation using Pt–TiO2 photocatalysts: an oxidation–reduction network, Catalysts 7 (2017) 324.

[109] Z.W. Seh, S. Liu, M. Low, S.Y. Zhang, Z. Liu, A. Mlayah, M.Y. Han, Janus Au-TiO2 photocatalysts with strong localization of plasmonic near-fields for efficient visible-light hydrogen generation, Adv. Mater. 24 (2012) 2310–2314.

[110] G.L. Chiarello, E. Selli, L. Forni, Photocatalytic hydrogen production over flame spray pyrolysis-synthesised TiO2 and Au/TiO2, Appl. Catal. B 84 (2008) 332–339.

[111] B. Naik, S.M. Kim, C.H. Jung, S.Y. Moon, S.H. Kim, J.Y. Park, Enhanced H2 generation of Au-Loaded, nitrogen-doped TiO2 hierarchical nanostructures under visible light, Adv. Mater. Interfaces 1 (2014).

[112] Cu. Gomes Silva, R. Juárez, T. Marino, R. Molinari, H. García, Influence of excitation wavelength (UV or visible light) on the photocatalytic activity of Titania containing gold nanoparticles for the generation of hydrogen or oxygen from water, J. Am. Chem. Soc. 133 (2010) 595–602.

[113] S. Oros-Ruiz, R. Zanella, R. López, A. Hernández-Gordillo, R. Gómez, Photocatalytic hydrogen production by water/methanol decomposition using Au/TiO2 prepared by deposition–precipitation with urea, J. Hazard. Mater. 263 (2013) 2–10.

[114] F. Wang, Y. Jiang, D.J. Lawes, G.E. Ball, C. Zhou, Z. Liu, R. Amal, Analysis of the promoted activity and molecular mechanism of hydrogen production over fine Au–Pt alloyed TiO2 photocatalysts, ACS Catal. 5 (2015) 3924–3931.

[115] F. Wang, Y. Jiang, A. Gautam, Y. Li, R. Amal, Exploring the origin of enhanced activity and reaction pathway for photocatalytic H2 production on Au/B-TiO2 catalysts, ACS Catal. 4 (2014) 1451–1457.

[116] T. Sreethawong, S. Yoshikawa, Impact of photochemically deposited monometallic Pt and bimetallic Pt–Au nanoparticles on photocatalytic dye-sensitized H2 production activity of mesoporous-assembled TiO2–SiO2 mixed oxide nanocrystal, Chem. Eng. J. 197 (2012) 272–282.

[117] L. Yoong, F.K. Chong, B.K. Dutta, Development of copper-doped TiO2 photocatalyst for hydrogen production under visible light, Energy 34 (2009) 1652–1661.

[118] K. Lalitha, G. Sadanandam, V.D. Kumari, M. Subrahmanyam, B. Sreedhar, N.Y. Hebalkar, Highly stabilized and finely dispersed Cu2O/TiO2: a promising visible sensitive photocatalyst for continuous production of hydrogen from glycerol: water mixtures, J. Phys. Chem. C 114 (2010) 22181–22189.

[119] S. Xu, A.J. Du, J. Liu, J. Ng, D.D. Sun, Highly efficient CuO incorporated TiO2 nanotube photocatalyst for hydrogen production from water, Int. J. Hydrogen Energy 36 (2011) 6560–6568.

[120] Z. Li, J. Liu, D. Wang, Y. Gao, J. Shen, Cu2O/ Cu/TiO2 nanotube Ohmic heterojunction arrays with enhanced photocatalytic hydrogen production activity, Int. J. Hydrogen Energy 37 (2012) 6431–6437.

[121] R. Bashiri, N.M. Mohamed, C.F. Kait, S. Sufian, Hydrogen production from water photosplitting using Cu/TiO2 nanoparticles: effect of hydrolysis rate and reaction medium, Int. J. Hydrogen Energy 40 (2015) 6021–6037.

[122] S. Xu, J. Ng, X. Zhang, H. Bai, D.D. Sun, Fabrication and comparison of highly efficient Cu incorporated TiO2 photocatalyst for hydrogen generation from water, Int. J. Hydrogen Energy 35 (2010) 5254–5261.

[123] J. Bandara, C. Udawatta, C. Rajapakse, Highly stable CuO incorporated TiO 2 catalyst for photocatalytic hydrogen production from H2O, Photochem. Photobiol. Sci. 4 (2005) 857–861.

[124] D.P. Kumar, N.L. Reddy, M.M. Kumari, B. Srinivas, V.D. Kumari, B. Sreedhar, V. Roddatis, O. Bondarchuk, M. Karthik, B. Neppolian, Cu2O-sensitized TiO2 nanorods with nanocavities for highly efficient photocatalytic hydrogen production under solar irradiation, Sol. Energy Mater. Sol. Cells 136 (2015) 157–166.

[125] Q. Hu, J. Huang, G. Li, Y. Jiang, H. Lan, W. Guo, Y. Cao, Origin of the improved photocatalytic activity of Cu incorporated TiO2 for hydrogen generation from water, Appl. Surf. Sci. 382 (2016) 170–177.

[126] L. Clarizia, D. Spasiano, I. Di Somma, R. Marotta, R. Andreozzi, D.D. Dionysiou, Copper modified-TiO2 catalysts for hydrogen generation through photoreforming of organics. A short review, Int. J. Hydrogen Energy 39 (2014) 16812–16831.

[127] J.M. Valero, S. Obregón, G. Colón, Active site considerations on the photocatalytic H2 evolution performance of Cu-doped TiO2 obtained by different doping methods, ACS Catal. 4 (2014) 3320–3329.

[128] T. Montini, V. Gombac, L. Sordelli, J.J. Delgado, X. Chen, G. Adami, P. Fornasiero, Nanostructured Cu/TiO2 Photocatalysts for H2 Production from Ethanol and Glycerol Aqueous Solutions, ChemCatChem 3 (2011) 574–577.

[129] F. Wu, X. Hu, J. Fan, E. Liu, T. Sun, L. Kang, W. Hou, C. Zhu, H. Liu, Photocatalytic activity of Ag/TiO 2 nanotube arrays enhanced by surface plasmon resonance and application in hydrogen evolution by water splitting, Plasmonics 8 (2013) 501–508.

[130] T.K. Rahul, M. Mohan, N. Sandhyarani, Enhanced solar hydrogen evolution over in situ gold-platinum bimetallic nanoparticle-loaded Ti3+ self-doped titania photocatalysts, ACS Sustain. Chem. Eng. 6 (2018) 3049–3059.

[131] A.T. Montoya, E.G. Gillan, Enhanced photocatalytic hydrogen evolution from transition-metal surface-modified TiO2, ACS Omega 3 (2018) 2947–2955.

[132] T. Sun, J. Fan, E. Liu, L. Liu, Y. Wang, H. Dai, Y. Yang, W. Hou, X. Hu, Z. Jiang, Fe and Ni co-doped TiO2 nanoparticles prepared by alcohol-thermal method: application in hydrogen evolution by water splitting under visible light irradiation, Powder Technol. 228 (2012) 210–218.

[133] R. Dholam, N. Patel, M. Adami, A. Miotello, Hydrogen production by photocatalytic water-splitting using Cr-or Fe-doped TiO2 composite thin films photocatalyst, Int. J. Hydrogen Energy 34 (2009) 5337–5346.

[134] B. Banerjee, V. Amoli, A. Maurya, A.K. Sinha, A. Bhaumik, Green synthesis of Pt-doped TiO2 nanocrystals with exposed (001) facets and mesoscopic void space for photo-splitting of water under solar irradiation, Nanoscale 7 (2015) 10504–10512.

[135] B.-S. Huang, M.-Y. Wey, Properties and H2 production ability of Pt photodeposited on the anatase phase transition of nitrogen-doped titanium dioxide, Int. J. Hydrogen Energy 36 (2011) 9479–9486.

[136] M.Z. Selcuk, M.S. Boroglu, I. Boz, Hydrogen production by photocatalytic water-splitting using nitrogen and metal co-doped TiO 2 powder photocatalyst, React. Kinet. Mech. Catal. 106 (2012) 313–324.

[137] X. Zhang, P. Song, X. Cui, Nitrogen-doped TiO2 photocatalysts synthesized from titanium nitride: characterizations and photocatalytic hydrogen evolution performance, J. Adv. Oxid. Technol. 16 (2013) 131–136.

[138] Z. Xing, Z. Li, X. Wu, G. Wang, W. Zhou, In-situ S-doped porous anatase TiO2 nanopillars for high-efficient visible-light photocatalytic hydrogen evolution, Int. J. Hydrogen Energy 41 (2016) 1535–1541.

[139] Y. Yang, K. Ye, D. Cao, P. Gao, M. Qiu, L. Liu, P. Yang, Efficient charge separation from F-Selectively etching and doping of Anatase-TiO2 {001} for enhanced photocatalytic hydrogen production, ACS Appl. Mater. Interfaces 10 (2018) 19633–19638.

[140] T. Sun, E. Liu, X. Liang, X. Hu, J. Fan, Enhanced hydrogen evolution from water splitting using Fe-Ni codoped and Ag deposited anatase TiO2 synthesized by solvothermal method, Appl. Surf. Sci. 347 (2015) 696–705.

[141] X. Fan, J. Wan, E. Liu, L. Sun, Y. Hu, H. Li, X. Hu, J. Fan, High-efficiency photoelectrocatalytic hydrogen generation enabled by Ag deposited and Ce doped TiO2 nanotube arrays, Ceram. Int. 41 (2015) 5107–5116.

[142] W. Zhang, S. Wang, J. Li, X. Yang, Photocatalytic hydrogen production from methanol aqueous solution under visible-light using Cu/S–TiO2 prepared by electroless plating method, Catal. Commun. 59 (2015) 189–194.

[143] X. Li, Q. Liu, X. Jiang, J. Huang, Enhanced photocatalytic activity of Ga-N Co-doped anatase TiO2 for water decomposition to hydrogen, Int. J. Electrochem. Sci. 7 (2012) 11519–11527.

[144] S. Luo, T.-D. Nguyen-Phan, D. Vovchok, I. Waluyo, R.M. Palomino, A.D. Gamalski, L. Barrio, W. Xu, D.E. Polyansky, J.A. Rodriguez, Enhanced, robust light-driven H 2 generation by gallium-doped titania nanoparticles, J. Chem. Soc. Faraday Trans. 20 (2018) 2104–2112.

[145] K.K. Mandari, A.K.R. Police, J.Y. Do, M. Kang, C. Byon, Rare earth metal Gd influenced defect sites in N doped TiO 2: defect mediated improved charge transfer for enhanced photocatalytic hydrogen production, Int. J. Hydrogen Energy 43 (2018) 2073–2082.

[146] J. Huang, G. Li, Z. Zhou, Y. Jiang, Q. Hu, C. Xue, W. Guo, Efficient photocatalytic hydrogen production over Rh and Nb codoped TiO2 nanorods, Chem. Eng. J. 337 (2018) 282–289.

[147] S.E. Salas, B.S. Rosales, H. de Lasa, Quantum yield with platinum modified TiO2 photocatalyst for hydrogen production, Appl. Catal. B 140 (2013) 523–536.

[148] R.A. Rather, S. Singh, B. Pal, A Cu+ 1/Cu0-TiO2 mesoporous nanocomposite exhibits improved H2 production from H2O under direct solar irradiation, J. Catal. 346 (2017) 1–9.

[149] M.J. Rivero, O. Iglesias, P. Ribao, I. Ortiz, Kinetic performance of TiO2/Pt/reduced graphene oxide composites in the photocatalytic hydrogen production, Int. J. Hydrogen Energy (2018), https://doi.org/10.1016/j.ijhydene.2018.02.115 (In Press).

[150] J. Jin, C. Wang, X.-N. Ren, S.-Z. Huang, M. Wu, L.-H. Chen, T. Hasan, B.-J. Wang, Y. Li, B.-L. Su, Anchoring ultrafine metallic and oxidized Pt nanoclusters on yolk-shell TiO2 for unprecedentedly high photocatalytic hydrogen production, Nano Energy 38 (2017) 118–126.

[151] A.L. Luna, D. Dragoe, K. Wang, P. Beaunier, E. Kowalska, B. Ohtani, D. Bahena Uribe, M.A. Valenzuela, H. Remita, C. Colbeau-Justin, Photocatalytic hydrogen evolution using Ni–Pd/TiO2: correlation of light absorption, charge-carrier dynamics, and quantum efficiency, J. Phys. Chem. C 121 (2017) 14302–14311.

[152] V. Likodimos, Photonic crystal-assisted visible light activated TiO 2 photocatalysis, Appl. Catal. B 230 (2018) 269–303.

[153] Z. Xing, J. Zhang, J. Cui, J. Yin, T. Zhao, J. Kuang, Z. Xiu, N. Wan, W. Zhou, Recent advances in floating TiO 2-based photocatalysts for environmental application, Appl. Catal. B 225 (2017) 452–467.

[154] S. Banerjee, D.D. Dionysiou, S.C. Pillai, Self-cleaning applications of TiO 2 by photo-induced hydrophilicity and photocatalysis, Appl. Catal. B 176 (2015) 396–428.

[155] X. Zhang, Y. Wang, B. Liu, Y. Sang, H. Liu, Heterostructures construction on TiO2 nanobelts: a powerful tool for building high-performance photocatalysts, Appl. Catal. B 202 (2017) 620–641.

[156] A.H. Mamaghani, F. Haghighat, C.-S. Lee, Photocatalytic oxidation technology for indoor environment air purification: the state-of-the-art, Appl. Catal. B 203 (2017) 247–269.

[157] Z. Shayegan, C.-S. Lee, F. Haghighat, TiO 2 photocatalyst for removal of volatile organic compounds in gas phase–a review, Chem. Eng. J. 334 (2017) 2408–2439.

[158] P. Ganguly, C. Byrne, A. Breen, S.C. Pillai, Antimicrobial activity of photocatalysts: fundamentals, mechanisms, kinetics and recent advances, Appl. Catal. B 225 (2017) 51–75.

[159] V. Etacheri, C. Di Valentin, J. Schneider, D. Bahnemann, S.C. Pillai, Visible-light activation of TiO2 photocatalysts: advances in theory and experiments, J. Photochem. Photobiol. C Photochem. Rev. 25 (2015) 1–29.

[160] B. Ohtani, Titania photocatalysis beyond recombination: a critical review, Catalysts 3 (2013) 942–953.

[161] K. Wenderich, G. Mul, Methods, mechanism, and applications of photodeposition in photocatalysis: a review, Chem. Rev. 116 (2016) 14587–14619.

[162] Y. Boyjoo, H. Sun, J. Liu, V.K. Pareek, S. Wang, A review on photocatalysis for air treatment: from catalyst development to reactor design, Chem. Eng. J. 310 (2017) 537–559.

[163] M. Wang, J. Ioccozia, L. Sun, C. Lin, Z. Lin, Inorganic-modified semiconductor TiO2 nanotube arrays for photocatalysis, Energy Environ. Sci. 7 (2014) 2182–2202.

[164] M. Pelaez, N.T. Nolan, S.C. Pillai, M.K. Seery, P. Falaras, A.G. Kontos, P.S. Dunlop, J.W. Hamilton, J.A. Byrne, K. O'shea, A review on the visible light active titanium dioxide photocatalysts for environmental applications, Appl. Catal. B 125 (2012) 331–349.

[165] M. Ni, M.K. Leung, D.Y. Leung, K. Sumathy, A review and recent developments in photocatalytic water-splitting using TiO2 for hydrogen production, Renew. Sustain. Energy Rev. 11 (2007) 401–425.

[166] T.-D. Nguyen-Phan, A.E. Baber, J.A. Rodriguez, S.D. Senanayake, Au and Pt nanoparticle supported catalysts tailored for H 2 production: from models to powder catalysts, Appl. Catal. A Gen. 518 (2016) 18–47.

[167] J. Ran, J. Zhang, J. Yu, M. Jaroniec, S.Z. Qiao, Earth-abundant cocatalysts for semiconductor-based photocatalytic water splitting, Chem. Soc. Rev. 43 (2014) 7787–7812.

[168] P.S. Kumar, J. Sundaramurthy, S. Sundarrajan, V.J. Babu, G. Singh, S.I. Allakhverdiev, S. Ramakrishna, Hierarchical electrospun nanofibers for energy harvesting, production and environmental remediation, Energy Environ. Sci. 7 (2014) 3192–3222.

[169] K. Shimura, H. Yoshida, Heterogeneous photocatalytic hydrogen production from water and biomass derivatives, Energy Environ. Sci. 4 (2011) 2467–2481.

[170] J.C. Colmenares, R. Luque, Heterogeneous photocatalytic nanomaterials: prospects and challenges in selective transformations of biomass-derived compounds, Chem. Soc. Rev. 43 (2014) 765–778.

[171] D.Y. Leung, X. Fu, C. Wang, M. Ni, M.K. Leung, X. Wang, X. Fu, Hydrogen production over titania-based photocatalysts, ChemSusChem 3 (2010) 681–694.

[172] M. Ge, Q. Li, C. Cao, J. Huang, S. Li, S. Zhang, Z. Chen, K. Zhang, S.S. Al-Deyab, Y. Lai, One-dimensional TiO2 nanotube photocatalysts for solar water splitting, Adv. Sci. 4 (2017).

[173] K.C. Christoforidis, P. Fornasiero, Photocatalytic hydrogen production: a rift into the future energy supply, ChemCatChem 9 (2017) 1523–1544.

[174] A.V. Puga, Photocatalytic production of hydrogen from biomass-derived feedstocks, Coord. Chem. Rev. 315 (2016) 1–66.

[175] G. Colón, Towards the hydrogen production by photocatalysis, Appl. Catal. A Gen. 518 (2016) 48–59.

[176] S.K. Saraswat, D.D. Rodene, R.B. Gupta, Recent advancements in semiconductor materials for photoelectrochemical water splitting for hydrogen production using visible light, Renew. Sustain. Energy Rev. 89 (2018) 228–248.

[177] B. Gupta, A.A. Melvin, T. Matthews, S. Dash, A. Tyagi, TiO2 modification by gold (Au) for photocatalytic hydrogen (H2) production, Renew. Sustain. Energy Rev. 58 (2016) 1366–1375.

[178] S.G. Ullattil, S.B. Narendranath, S.C. Pillai, P. Periyat, Black TiO 2 nanomaterials: a review of recent advances, Chem. Eng. J. (2018).

[179] M. Abdullah, S. Kamarudin, Titanium dioxide nanotubes (TNT) in energy and environmental applications: an overview, Renew. Sustain. Energy Rev. 76 (2017) 212–225.

[180] T. Hisatomi, J. Kubota, K. Domen, Recent advances in semiconductors for photocatalytic and photoelectrochemical water splitting, Chem. Soc. Rev. 43 (2014) 7520–7535.

[181] J. Liqiang, S. Xiaojun, S. Jing, C. Weimin, X. Zili, D. Yaoguo, F. Honggang, Review of surface photovoltage spectra of nano-sized semiconductor and its applications in heterogeneous photocatalysis, Sol. Energy Mater. Sol. Cells 79 (2003) 133–151.

[182] Z. Zhang, J.T. Yates Jr, Band bending in semiconductors: chemical and physical consequences at surfaces and interfaces, Chem. Rev. 112 (2012) 5520–5551.

[183] V. Subramanian, E.E. Wolf, P.V. Kamat, Catalysis with TiO2/gold nanocomposites. Effect of metal particle size on the Fermi level equilibration, J. Am. Chem. Soc. 126 (2004) 4943–4950.

[184] P.V. Kamat, Quantum dot solar cells. Semiconductor nanocrystals as light harvesters, J. Phys. Chem. C 112 (2008) 18737–18753.

[185] N. Guo, Y. Zeng, H. Li, X. Xu, H. Yu, Crumpled and flexible cotton-fiber-like TiO2 with Pt anchored and its notable photocatalytic activity facilitate by Schottky junction interface, Mater. Lett. 221 (2018) 183–186.

[186] F. López-Tenllado, J. Hidalgo-Carrillo, V. Montes, A. Marinas, F. Urbano, J. Marinas, L. Ilieva, T. Tabakova, F. Reid, A comparative study of hydrogen photocatalytic production from glycerol and propan-2-ol on M/TiO2 systems (M= Au, Pt, Pd), Catal. Today 280 (2017) 58–64.

[187] C.-C. Nguyen, D.T. Nguyen, T.-O. Do, A novel route to synthesize C/Pt/TiO2 phase tunable anatase–Rutile TiO2 for efficient sunlight-driven photocatalytic applications, Appl. Catal. B 226 (2018) 46–52.

[188] J. Zhang, Z. Yu, Z. Gao, H. Ge, S. Zhao, C. Chen, S. Chen, X. Tong, M. Wang, Z. Zheng, Porous TiO2 nanotubes with spatially separated platinum and CoOx cocatalysts produced by atomic layer deposition for photocatalytic hydrogen production, Angew. Chem. Int. Ed. 56 (2017) 816–820.

[189] H. Belhadj, S. Hamid, P.K. Robertson, D.W. Bahnemann, Mechanisms of simultaneous hydrogen production and formaldehyde oxidation in H2O and D2O over platinized TiO2, ACS Catal. 7 (2017) 4753–4758.

[190] B. Liu, Y. Jiang, Y. Wang, S. Shang, Y. Ni, N. Zhang, M. Cao, C. Hu, Influence of dimension and crystallization on visible-light hydrogen production of Au@ TiO2 core-shell photocatalysts based on localized surface plasmon resonance, Catal. Sci. Technol. 8 (2018) 1094–1103.

[191] Y. Si, S. Cao, Z. Wu, Y. Ji, Y. Mi, X. Wu, X. Liu, L. Piao, What is the predominant electron transfer process for Au NRs/TiO2 nanodumbbell heterostructure under sunlight irradiation? Appl. Catal. B 220 (2018) 471–476.

[192] Z. Li, B. Tian, W. Zhen, Y. Wu, G. Lu, Inhibition of hydrogen and oxygen recombination using oxygen transfer reagent hemin chloride in Pt/TiO2 dispersion for photocatalytic hydrogen generation, Appl. Catal. B 203 (2017) 408–415.

[193] S. Escobedo, B. Serrano, A. Calzada, J. Moreira, H. de Lasa, Hydrogen production using a platinum modified TiO2 photocatalyst and an organic scavenger, Kinet. Model. Fuel 181 (2016) 438–449.

[194] C. Marchal, A. Piquet, M. Behr, T. Cottineau, V. Papaefthimiou, V. Keller, V. Caps, Activation of solid grinding-derived Au/TiO2 photocatalysts for solar H2 production from water-methanol mixtures with low alcohol content, J. Catal. 352 (2017) 22–34.

[195] T.K. Rahul, M. Mohan, N. Sandhyarani, Enhanced solar hydrogen evolution over in situ gold–Platinum bimetallic nanoparticle-loaded Ti3+ self-doped titania photocatalysts, ACS Sustain. Chem. Eng. 6 (2018) 3049–3059.

[196] D. Wang, S.C. Pillai, S.-H. Ho, J. Zeng, Y. Li, D.D. Dionysiou, Plasmonic-based nanomaterials for environmental remediation, Appl. Catal. B 237 (2018) 721–741.

[197] D. Panayotov, A. Frenkel, J. Morris, Catalysis and photocatalysis by nanoscale Au/ TiO2: perspectives for renewable energy, ACS Energy Lett. 2 (2017) 1223–1231.

[198] W. Hou, S. Cronin, A review of surface plasmon resonance-enhanced photocatalysis, Adv. Funct. Mater. 23 (2013) 1612–1619.

[199] G.V. Hartland, L.V. Besteiro, P. Johns, A.O. Govorov, What's so hot about electrons in metal nanoparticles? ACS Energy Lett. 2 (2017) 1641–1653.

[200] K.K. Patra, C.S. Gopinath, Bimetallic and plasmonic Ag–Au on TiO2 for solar water splitting: an active nanocomposite for entire visible-light-Region absorption, ChemCatChem 8 (2016) 3294–3311.

[201] J. Fang, S.-W. Cao, Z. Wang, M.M. Shahjamali, S.C.J. Loo, J. Barber, C. Xue, Mesoporous plasmonic Au–TiO2 nanocomposites for efficient visible-light-driven photocatalytic water reduction, Int. J. Hydrogen Energy 37 (2012) 17853–17861.

[202] S. Linic, P. Christopher, D.B. Ingram, Plasmonic-metal nanostructures for efficient conversion of solar to chemical energy, Nat. Mater. 10 (2011) 911.

[203] E. Liu, L. Kang, Y. Yang, T. Sun, X. Hu, C. Zhu, H. Liu, Q. Wang, X. Li, J. Fan, Plasmonic Ag deposited TiO2 nano-sheet film for enhanced photocatalytic hydrogen production by water splitting, Nanotechnology 25 (2014) 165401.

[204] A. Naldoni, U. Guler, Z. Wang, M. Marelli, F. Malara, X. Meng, L.V. Besteiro, A.O. Govorov, A.V. Kildishev, A. Boltasseva, Broadband hot-electron collection for solar water splitting with plasmonic titanium nitride, Adv. Opt. Mater. 5 (2017) 1601031.

[205] E.W. Awin, A. Lale, K.H. Kumar, U.B. Demirci, S. Bernard, R. Kumar, Plasmon enhanced visible light photocatalytic activity in polymer-derived TiN/Si-OCN nanocomposites, Mater. Des. 157 (2018) 87–96.

[206] A. Capretti, Y. Wang, N. Engheta, L. Dal Negro, Comparative study of second-harmonic generation from epsilon-near-zero indium tin oxide and titanium nitride nanolayers excited in the near-infrared spectral range, ACS Photonics 2 (2015) 1584–1591.

[207] J.A. Briggs, G.V. Naik, T.A. Petach, B.K. Baum, D. Goldhaber-Gordon, J.A. Dionne, Fully CMOS-compatible titanium nitride nanoantennas, Appl. Phys. Lett. 108 (2016) 051110.

[208] L. Gui, S. Bagheri, N. Strohfeldt, M. Hentschel, C.M. Zgrabik, B. Metzger, H. Linnenbank, E.L. Hu, H. Giessen, Nonlinear refractory plasmonics with titanium nitride nanoantennas, Nano Lett. 16 (2016) 5708–5713.

[209] S. Martha, P.C. Sahoo, K. Parida, An overview on visible light responsive metal oxide based photocatalysts for hydrogen energy production, RSC Adv. 5 (2015) 61535–61553.

[210] G. Liu, C. Sun, X. Yan, L. Cheng, Z. Chen, X. Wang, L. Wang, S.C. Smith, G.Q.M. Lu, H.-M. Cheng, Iodine doped anatase TiO 2 photocatalyst with ultra-long visible light response: correlation between geometric/electronic structures and mechanisms, J. Mater. Chem. 19 (2009) 2822–2829.

[211] V.J. Babu, M.K. Kumar, A.S. Nair, T.L. Kheng, S.I. Allakhverdiev, S. Ramakrishna, Visible light photocatalytic water splitting for hydrogen production from N-TiO2 rice grain shaped electrospun nanostructures, Int. J. Hydrogen Energy 37 (2012) 8897–8904.

[212] J. Fang, F. Wang, K. Qian, H. Bao, Z. Jiang, W. Huang, Bifunctional N-doped mesoporous TiO2 photocatalysts, J. Phys. Chem. C 112 (2008) 18150–18156.

[213] G. Zhang, X. Ding, Y. Hu, B. Huang, X. Zhang, X. Qin, J. Zhou, J. Xie, Photocatalytic degradation of 4BS dye by N, S-codoped TiO2 pillared montmorillonite photocatalysts under visible-light irradiation, J. Phys. Chem. C 112 (2008) 17994–17997.

[214] R. Shi, Z. Li, H. Yu, L. Shang, C. Zhou, G.I. Waterhouse, L.-Z. Wu, T. Zhang, Effect of nitrogen doping level on the performance of N-doped carbon quantum dot/TiO2 composites for photocatalytic hydrogen evolution, ChemSusChem 10 (2017) 4650–4656.

[215] Y.-P. Peng, H. Chen, C. Huang, The synergistic effect of photoelectrochemical (PEC) reactions exemplified by concurrent perfluorooctanoic acid (PFOA) degradation and hydrogen generation over carbon and nitrogen codoped TiO2 nanotube arrays (CN-TNTAs) photoelectrode, Appl. Catal. B 209 (2017) 437–446.

[216] L. Preethi, R.P. Antony, T. Mathews, L. Walczak, C.S. Gopinath, A study on doped heterojunctions in TiO 2 nanotubes: an efficient photocatalyst for solar water splitting, Sci. Rep. 7 (2017) 14314.

[217] R. Asahi, T. Morikawa, T. Ohwaki, K. Aoki, Y. Taga, Visible-light photocatalysis in nitrogen-doped titanium oxides, Science 293 (2001) 269–271.

[218] J. Huang, G. Li, Z. Zhou, Y. Jiang, Q. Hu, C. Xue, W. Guo, Efficient photocatalytic hydrogen production over Rh and Nb codoped TiO2 nanorods, Chem. Eng. J. (2017).

[219] X. Wang, R. Long, D. Liu, D. Yang, C. Wang, Y. Xiong, Enhanced full-spectrum water splitting by confining plasmonic Au nanoparticles in N-doped TiO2 bowl nanoarrays, Nano Energy 24 (2016) 87–93.

[220] M. Jung, J.N. Hart, J. Scott, Y.H. Ng, J. Jiang, R. Amal, Exploring Cu oxidation state on TiO2 and its transformation during photocatalytic hydrogen evolution, Appl. Catal. A Gen. 521 (2016) 190–201.

[221] Z. Wang, Y. Liu, D.J. Martin, W. Wang, J. Tang, W. Huang, CuO x–TiO 2 junction: what is the active component for photocatalytic H 2 production? J. Chem. Soc. Faraday Trans. 15 (2013) 14956–14960.

[222] S. Zhang, B. Peng, S. Yang, Y. Fang, F. Peng, The influence of the electrodeposition potential on the morphology of Cu2O/TiO2 nanotube arrays and their visible-light-driven photocatalytic activity for hydrogen evolution, Int. J. Hydrogen Energy 38 (2013) 13866–13871.

[223] I.-H. Tseng, W.-C. Chang, J.C. Wu, Photoreduction of CO2 using sol–gel derived titania and titania-supported copper catalysts, Appl. Catal. B 37 (2002) 37–48.

[224] J.M. Kum, Y.J. Park, H.J. Kim, S.O. Cho, Plasmon-enhanced photocatalytic hydrogen production over visible-light responsive Cu/TiO2, Nanotechnology 26 (2015) 125402.

[225] M. Jung, J.N. Hart, D. Boensch, J. Scott, Y.H. Ng, R. Amal, Hydrogen evolution via glycerol photoreforming over Cu–Pt nanoalloys on TiO2, Appl. Catal. A Gen. 518 (2016) 221–230.

[226] L. Clarizia, G. Vitiello, G. Luciani, I. Di Somma, R. Andreozzi, R. Marotta, In situ photodeposited nanoCu on TiO2 as a catalyst for hydrogen production under UV/visible radiation, Appl. Catal. A Gen. 518 (2016) 142–149.

[227] A. Pérez-Larios, A. Hernández-Gordillo, G. Morales-Mendoza, L. Lartundo-Rojas, Á. Mantilla, R. Gómez, Enhancing the H2 evolution from water–methanol solution using Mn2+–Mn+ 3–Mn4+ redox species of Mn-doped TiO2 sol–gel photocatalysts, Catal. Today 266 (2016) 9–16.

[228] B. Choudhury, A. Choudhury, Oxygen vacancy and dopant concentration dependent magnetic properties of Mn doped TiO2 nanoparticle, Curr. Appl. Phys. 13 (2013) 1025–1031.

[229] J. Jung, H. Gress, Single-photon absorption of liquid methanol and ethanol in the vacuum ultraviolet, Chem. Phys. Lett. 359 (2002) 153–157.

[230] J. Jung, Single-photon ionisation of liquid methanol and ethanol, Chem. Phys. Lett. 366 (2002) 67–72.

[231] S. Paul, P. Chetri, A. Choudhury, Effect of manganese doping on the optical property and photocatalytic activity of nanocrystalline titania: experimental and theoretical investigation, J. Alloys Compd. 583 (2014) 578–586.

[232] Y. Xu, B. Lei, L. Guo, W. Zhou, Y. Liu, Preparation, characterization and photocatalytic activity of manganese doped TiO2 immobilized on silica gel, J. Hazard. Mater. 160 (2008) 78–82.

[233] L.G. Devi, S.G. Kumar, B.N. Murthy, N. Kottam, Influence of Mn2+ and Mo6+ dopants on the phase transformations of TiO2 lattice and its photo catalytic

activity under solar illumination, Catal. Commun. 10 (2009) 794–798.

[234] L.G. Devi, N. Kottam, S.G. Kumar, Preparation and characterization of Mn-doped titanates with a bicrystalline framework: correlation of the crystallite size with the synergistic effect on the photocatalytic activity, J. Phys. Chem. C 113 (2009) 15593–15601.

[235] X. Yan, C. Xue, B. Yang, G. Yang, Novel three-dimensionally ordered macroporous Fe3 + -doped TiO2 photocatalysts for H2 production and degradation applications, Appl. Surf. Sci. 394 (2017) 248–257.

[236] A. Banisharif, A.A. Khodadadi, Y. Mortazavi, A.A. Firooz, J. Beheshtian, S. Agah, S. Menbari, Highly active Fe2O3-doped TiO2 photocatalyst for degradation of trichloroethylene in air under UV and visible light irradiation: experimental and computational studies, Appl. Catal. B 165 (2015) 209–221.

[237] X. Wang, J.-G. Li, H. Kamiyama, Y. Moriyoshi, T. Ishigaki, Wavelength-sensitive photocatalytic degradation of methyl orange in aqueous suspension over iron (III)-doped TiO2 nanopowders under UV and visible light irradiation, J. Phys. Chem. B 110 (2006) 6804–6809.

[238] X. Hong, D. Wang, S. Cai, H. Rong, Y. Li, Single-crystalline octahedral Au–Ag nanoframes, J. Am. Chem. Soc. 134 (2012) 18165–18168.

[239] M.A. Nadeem, M. Al-Oufi, A.K. Wahab, D. Anjum, H. Idriss, Hydrogen Production on Ag-Pd/TiO2 Bimetallic Catalysts: Is there a Combined Effect of Surface Plasmon Resonance with Schottky Mechanism on the Photo-Catalytic Activity? ChemistrySelect 2 (2017) 2754–2762.

[240] Y. Tian, T. Tatsuma, Mechanisms and applications of plasmon-induced charge separation at TiO2 films loaded with gold nanoparticles, J. Am. Chem. Soc. 127 (2005) 7632–7637.

[241] S.K. Cushing, J. Li, F. Meng, T.R. Senty, S. Suri, M. Zhi, M. Li, A.D. Bristow, N. Wu, Photocatalytic activity enhanced by plasmonic resonant energy transfer from metal to semiconductor, J. Am. Chem. Soc. 134 (2012) 15033–15041.

[242] K. Awazu, M. Fujimaki, C. Rockstuhl, J. Tominaga, H. Murakami, Y. Ohki, N. Yoshida, T. Watanabe, A plasmonic photocatalyst consisting of silver nanoparticles embedded in titanium dioxide, J. Am. Chem. Soc. 130 (2008) 1676–1680.

[243] J. Lee, T. Javed, T. Skeini, A.O. Govorov, G.W. Bryant, N.A. Kotov, Bioconjugated Ag nanoparticles and CdTe nanowires: metamaterials with field-enhanced light absorption, Angew. Chem. Int. Ed. 45 (2006) 4819–4823.

[244] A.L. Luna, E. Novoseltceva, E. Louarn, P. Beaunier, E. Kowalska, B. Ohtani, M.A. Valenzuela, H. Remita, C. Colbeau-Justin, Synergetic effect of Ni and Au nanoparticles synthesized on titania particles for efficient photocatalytic hydrogen production, Appl. Catal. B 191 (2016) 18–28.

[245] H. Zhuang, Y. Zhang, Z. Chu, J. Long, X. An, H. Zhang, H. Lin, Z. Zhang, X. Wang, Synergy of metal and nonmetal dopants for visible-light photocatalysis: a case-study of Sn and N co-doped TiO 2, J. Chem. Soc. Faraday Trans. 18 (2016) 9636–9644.

[246] X. Chen, C. Burda, Photoelectron spectroscopic investigation of nitrogen-doped titania nanoparticles, J. Phys. Chem. B 108 (2004) 15446–15449.

[247] X. Chen, Y.B. Lou, A.C. Samia, C. Burda, J.L. Gole, Formation of oxynitride as the photocatalytic enhancing site in nitrogen-doped titania nanocatalysts: comparison to a commercial nanopowder, Adv. Funct. Mater. 15 (2005) 41–49.

[248] L. Gao, Y. Li, J. Ren, S. Wang, R. Wang, G. Fu, Y. Hu, Passivation of defect states in anatase TiO2 hollow spheres with Mg doping: realizing efficient photocatalytic overall water splitting, Appl. Catal. B 202 (2017) 127–133.

[249] M. Murdoch, G. Waterhouse, M. Nadeem, J. Metson, M. Keane, R. Howe, J. Llorca, H. Idriss, The effect of gold loading and particle size on photocatalytic hydrogen production from ethanol over Au/TiO 2 nanoparticles, Nat. Chem. 3 (2011) 489.

[250] L. Clarizia, I. Di Somma, L. Onotri, R. Andreozzi, R. Marotta, Kinetic modeling of hydrogen generation over nano-Cu (s)/TiO2 catalyst through photoreforming of alcohols, Catal. Today 281 (2017) 117–123.

[251] J. Krýsa, G. Waldner, H. Měšt'ánková, J. Jirkovský, G. Grabner, Photocatalytic degradation of model organic pollutants on an immobilized particulate TiO2 layer: roles of adsorption processes and mechanistic complexity, Appl. Catal. B 64 (2006) 290–301.

[252] Y. Tamaki, A. Furube, M. Murai, K. Hara, R. Katoh, M. Tachiya, Direct observation of reactive trapped holes in TiO2 undergoing photocatalytic oxidation of adsorbed alcohols: evaluation of the reaction rates and yields, J. Am. Chem. Soc. 128 (2006) 416–417.

[253] P. Gomathisankar, D. Yamamoto, H. Katsumata, T. Suzuki, S. Kaneco, Photocatalytic hydrogen production with aid of simultaneous metal deposition using titanium dioxide from aqueous glucose solution, Int. J. Hydrogen Energy 38 (2013) 5517–5524.

[254] M. Bernareggi, M.V. Dozzi, L.G. Bettini, A.M. Ferretti, G.L. Chiarello, E. Selli, Flame-made Cu/TiO2 and Cu-Pt/TiO2 photocatalysts for hydrogen production, Catalysts 7 (2017) 301.

[255] G.L. Chiarello, D. Ferri, E. Selli, Effect of the CH3OH/H2O ratio on the mechanism of the gas-phase photocatalytic reforming of methanol on noble metal-modified TiO2, J. Catal. 280 (2011) 168–177.

[256] J. Marugán, R. Van Grieken, A.E. Cassano, O.M. Alfano, Intrinsic kinetic modeling with explicit radiation absorption effects of the photocatalytic oxidation of cyanide with TiO2 and silica-supported TiO2 suspensions, Appl. Catal. B 85 (2008) 48–60.

[257] A.E. Cassano, O.M. Alfano, Reaction engineering of suspended solid heterogeneous photocatalytic reactors, Catal. Today 58 (2000) 167–197.

[258] M.L. Satuf, R.J. Brandi, A.E. Cassano, O.M. Alfano, Experimental method to evaluate the optical properties of aqueous titanium dioxide suspensions, Ind. Eng. Chem. Res. 44 (2005) 6643–6649.

[259] R. Acosta-Herazo, M.Á. Mueses, G.L. Puma, F. Machuca-Martínez, Impact of photocatalyst optical properties on the efficiency of solar photocatalytic reactors

rationalized by the concepts of initial rate of photon absorption (IRPA) dimensionless boundary layer of photon absorption and apparent optical thickness, Chem. Eng. J. 356 (2019) 839–849.

[260] J. Colina-Márquez, F. Machuca-Martínez, G.L.J.Es. Puma, Radiation absorption and optimization of solar photocatalytic reactors for environmental applications, Environ. Sci. Technol. 44 (2010) 5112–5120.

[261] G.L. Puma, A.J.C.T. Brucato, Dimensionless analysis of slurry photocatalytic reactors using two-flux and six-flux radiation absorption–scattering models, Catal. Today 122 (2007) 78–90.

[262] Z. Xing, X. Zong, J. Pan, L. Wang, On the engineering part of solar hydrogen production from water splitting: photoreactor design, Chem. Eng. Sci. 104 (2013) 125–146.

[263] M.J. Muñoz-Batista, M. de los Milagros Ballari, A. Kubacka, A.E. Cassano, O.M. Alfano, M. Fernández-García, Acetaldehyde degradation under UV and visible irradiation using CeO2–TiO2 composite systems: evaluation of the photocatalytic efficiencies, Chem. Eng. J. 255 (2014) 297–306.

[264] G.E. Imoberdorf, A.E. Cassano, H.A. Irazoqui, O.M. Alfano, Simulation of a multi-annular photocatalytic reactor for degradation of perchloroethylene in air: parametric analysis of radiative energy efficiencies, Chem. Eng. Sci. 62 (2007) 1138–1154.

[265] V. Preethi, S. Kanmani, Performance of four various shapes of photocatalytic reactors with respect to hydrogen and sulphur recovery from sulphide containing wastestreams, J. Clean. Prod. 133 (2016) 1218–1226.

[266] S. Rajamohan, V. Kumaravel, R. Muthuramalingam, S. Ayyadurai, A. Abdel-Wahab, B.S. Kwak, M. Kang, S. Sreekantan, Fe 3 O 4–Ag 2 WO 4: facile synthesis, characterization and visible light assisted photocatalytic activity, New J. Chem. 41 (2017) 11722–11730.

[267] D. Jing, L. Guo, L. Zhao, X. Zhang, H. Liu, M. Li, S. Shen, G. Liu, X. Hu, X. Zhang, Efficient solar hydrogen production by photocatalytic water splitting: from fundamental study to pilot demonstration, Int. J. Hydrogen Energy 35 (2010) 7087–7097.

[268] N. Skillen, M. Adams, C. McCullagh, S.Y. Ryu, F. Fina, M.R. Hoffmann, J.T. Irvine, P.K. Robertson, The application of a novel fluidised photo reactor under UV–visible and natural solar irradiation in the photocatalytic generation of hydrogen, Chem. Eng. J. 286 (2016) 610–621.

[269] E. Baniasadi, I. Dincer, G. Naterer, Exergy and environmental impact assessment of solar photoreactors for catalytic hydrogen production, Chem. Eng. J. 213 (2012) 330–337.

[270] Y. Yuan, Z. Ye, H. Lu, B. Hu, Y. Li, D. Chen, J. Zhong, Z. Yu, Z. Zou, Constructing anatase TiO2 nanosheets with exposed (001) Facets/Layered MoS2 two-dimensional nanojunctions for enhanced solar hydrogen generation, ACS Catal. 6 (2016) 532–541.

[271] Q. Lu, Y. Yu, Q. Ma, B. Chen, H. Zhang, 2D transition-metal-Dichalcogenide-Nanosheet-Based composites for photocatalytic and electrocatalytic hydrogen evolution reactions, Adv. Mater. 28 (2016) 1917–1933.

[272] Q. Liu, H. Lu, Z. Shi, F. Wu, J. Guo, K. Deng, L. Li, 2D ZnIn2S4 Nanosheet/lD TiO2 nanorod heterostructure arrays for improved photoelectrochemical water splitting, ACS Appl. Mater. Interfaces 6 (2014) 17200–17207.

[273] Y.-J. Yuan, D. Chen, J. Zhong, L.-X. Yang, J. Wang, M.-J. Liu, W.-G. Tu, Z.-T. Yu, Z.-G. Zou, Interface engineering of a noble-metal-free 2D–2D MoS 2/Cu-ZnIn 2 S 4 photocatalyst for enhanced photocatalytic H 2 production, J. Mater. Chem. A 5 (2017) 15771–15779.

[274] K. Zhang, S. Qian, W. Kim, J.K. Kim, X. Sheng, J.Y. Lee, J.H. Park, Double 2-dimensional H2-evolving catalyst tipped photocatalyst nanowires: a new avenue for high-efficiency solar to H2 generation, Nano Energy 34 (2017) 481–490.

[275] J. Ran, W. Guo, H. Wang, B. Zhu, J. Yu, S.Z. Qiao, Metal-free 2D/2D Phosphorene/g-C3N4 van der waals heterojunction for highly enhanced visible-light photocatalytic H2 production, Adv. Mater. (2018) 1800128.

[276] C. Liu, L. Wang, Y. Tang, S. Luo, Y. Liu, S. Zhang, Y. Zeng, Y. Xu, Vertical single or few-layer MoS2 nanosheets rooting into TiO2 nanofibers for highly efficient photocatalytic hydrogen evolution, Appl. Catal. B 164 (2015) 1–9.

[277] D. Voiry, H. Shin, K. Loh, M. Chhowalla, Low-dimensional catalysts for hydrogen evolution and CO2 reduction, Nat. Rev. Chem. 2 (2018).

[278] A.K. Singh, K. Mathew, H.L. Zhuang, R.G. Hennig, Computational screening of 2D materials for photocatalysis, J. Phys. Chem. Lett. 6 (2015) 1087–1098.

[279] M. Chhowalla, D. Voiry, J. Yang, H. Shin, K. Loh, Phase-engineered transition-metal dichalcogenides for energy and electronics, MRS Bull. 40 (2015) 585–591.

[280] D. Voiry, J. Yang, M. Chhowalla, Recent Strategies for Improving the Catalytic Activity of 2D TMD Nanosheets Toward the Hydrogen Evolution Reaction, Adv. Mater. 28 (2016) 6197–6206.

[281] K. Chan, C. Tsai, H. Hansen, J. Norskov, Molybdenum sulfides and selenides as possible electrocatalysts for CO2 reduction, ChemCatChem 6 (2014) 1899–1905.

[282] A. Tuxen, J. Kibsgaard, H. Gobel, E. Laegsgaard, H. Topsoe, J. Lauritsen, F. Besenbacher, Size threshold in the dibenzothiophene adsorption on MoS2 nanoclusters, ACS Nano 4 (2010) 4677–4682.

[283] J. Lauritsen, M. Nyberg, J. Norskov, B. Clausen, H. Topsoe, E. Laegsgaard, F. Besenbacher, Hydrodesulfurization reaction pathways on MoS2 nanoclusters revealed by scanning tunneling microscopy, J. Catal. 224 (2004) 94–106.

[284] A. Kuc, N. Zibouche, T. Heine, Influence of quantum confinement on the electronic structure of the transition metal sulfide TS2, Phys. Rev. B 83 (2011).

[285] M. Pandey, K. Jacobsen, K. Thygesen, Atomically thin ordered alloys of transition metal dichalcogenides: stability and band structures, J. Phys. Chem. C 120 (2016) 23024–23029.

[286] S. Bai, L. Wang, X. Chen, J. Du, Y. Xiong, Chemically exfoliated metallic MoS2 nanosheets: a promising supporting co-catalyst for enhancing the photocatalytic performance of TiO2 nanocrystals, Nano Res. 8 (2015) 175–183.

[287] J. Kang, S. Tongay, J. Zhou, J. Li, J. Wu, Band offsets and heterostructures of two-dimensional semiconductors, Appl. Phys. Lett. 102 (2013).

[288] Y. Li, Y. Li, B. Sa, R. Ahuja, Review of two-dimensional materials for photocatalytic water splitting from a theoretical perspective, Catal. Sci. Technol. 7 (2017) 545–559.

[289] T. Su, Q. Shao, Z. Qin, Z. Guo, Z. Wu, Role of interfaces in two-dimensional photocatalyst for water splitting, ACS Catal. 8 (2018) 2253–2276.

[290] B. Lin, H. Li, H. An, W. Hao, J. Wei, Y. Dai, C. Ma, G. Yang, Preparation of 2D/2D g-C3N4 nanosheet@ ZnIn2S4 nanoleaf heterojunctions with well-designed high-speed charge transfer nanochannels towards high-efficiency photocatalytic hydrogen evolution, Appl. Catal. B 220 (2018) 542–552.

[291] P. Kanhere, Z. Chen, A review on visible light active perovskite-based photocatalysts, Molecules 19 (2014) 19995–20022.

[292] E. Grabowska, Selected perovskite oxides: characterization, preparation and photocatalytic properties—a review, Appl. Catal. B 186 (2016) 97–126.

[293] H. Tanaka, M. Misono, Advances in designing perovskite catalysts, Curr. Opin. Solid State Mater. Sci. 5 (2001) 381–387.

[294] P. Ju, H. Fan, B. Zhang, K. Shang, T. Liu, S. Ai, D. Zhang, Enhanced photocatalytic activity of β-AgVO3 nanowires loaded with Ag nanoparticles under visible light irradiation, Sep. Purif. Technol. 109 (2013) 107–110.

[295] C. Li, Y. Zhu, S. Fang, H. Wang, Y. Gui, L. Bi, R. Chen, Preparation and characterization of SrSnO3 nanorods, J. Phys. Chem. Solids 72 (2011) 869–874.

[296] P. Liu, J. Nisar, B. Pathak, R. Ahuja, Hybrid density functional study on SrTiO3 for visible light photocatalysis, Int. J. Hydrogen Energy 37 (2012) 11611–11617.

[297] C. Hu, H. Teng, Influence of structural features on the photocatalytic activity of NaTaO3 powders from different synthesis methods, Appl. Catal. Gen. 331 (2007) 44–50.

[298] T. Zhang, K. Zhao, J. Yu, J. Jin, Y. Qi, H. Li, X. Hou, G. Liu, Photocatalytic water splitting for hydrogen generation on cubic, orthorhombic, and tetragonal KNbO 3 microcubes, Nanoscale 5 (2013) 8375–8383.

[299] P. Li, S. Ouyang, G. Xi, T. Kako, J. Ye, The effects of crystal structure and electronic structure on photocatalytic H2 evolution and CO2 reduction over two phases of perovskite-structured NaNbO3, J. Phys. Chem. C 116 (2012) 7621–7628.

[300] Y. Zhu, Y. Dai, K. Lai, Z. Li, B. Huang, Optical transition and photocatalytic performance of d1 metallic perovskites, J. Phys. Chem. C 117 (2013) 5593–5598.

[301] L. Lu, S. Ni, G. Liu, X. Xu, Structural dependence of photocatalytic hydrogen production over La/Cr co-doped perovskite compound ATiO3 (A = Ca, Sr and Ba), Int. J. Hydrogen Energy 42 (2017) 23539–23547.

[302] W. Chen, H. Liu, X. Li, S. Liu, L. Gao, L. Mao, Z. Fan, W. Shangguan, W. Fang, Y. Liu, Polymerizable complex synthesis of SrTiO3:(Cr/Ta) photocatalysts to improve photocatalytic water splitting activity under visible light, Appl. Catal. B 192 (2016) 145–151.

[303] J. Zou, L. Zhang, S. Luo, L. Leng, X. Luo, M. Zhang, Y. Luo, G. Guo, Preparation and photocatalytic activities of two new Zn-doped SrTiO3 and BaTiO3 photocatalysts for hydrogen production from water without cocatalysts loading, Int. J. Hydrogen Energy 37 (2012) 17068–17077.

[304] H. Zhang, G. Chen, Y. Li, Y. Teng, Electronic structure and photocatalytic properties of copper-doped CaTiO3, Int. J. Hydrogen Energy 35 (2010) 2713–2716.

[305] N. Zhang, Y. Qu, K. Pan, G. Wang, Y. Li, Synthesis of pure phase Mg1.2Ti1.8O5 and MgTiO3 nanocrystals for photocatalytic hydrogen production, Nano Res. 9 (2016) 726–734.

[306] J. Huang, Y. Jiang, G. Li, C. Xue, W. Guo, Hetero-structural NiTiO3/TiO2 nanotubes for efficient photocatalytic hydrogen generation, Renew. Energy 111 (2017) 410–415.

[307] R. Wang, S. Ni, G. Liu, X. Xu, Hollow CaTiO3 cubes modified by La/Cr co-doping for efficient photocatalytic hydrogen production, Appl. Catal. B Environ. 225 (2018) 139–147.

[308] L. Meng, Z. Ren, W. Zhou, Y. Qu, G. Wang, MgTiO3/MgTi2O5/TiO2 heterogeneous belt-junctions with high photocatalytic hydrogen production activity, Nano Res. 10 (2017) 295–304.

[309] G. Zhang, S. Sun, W. Jiang, X. Miao, Z. Zhao, X. Zhang, D. Qu, D. Zhang, D. Li, Z. Sun, A novel perovskite SrTiO3-Ba2FeNbO6 solid solution for visible light photocatalytic hydrogen production, Adv. Energy Mater. 7 (2017).

[310] M. Sandroni, R. Gueret, K. Wegner, P. Reiss, J. Fortage, D. Aldakov, M.-N. Collomb, Cadmium-free CuInS 2/ZnS quantum dots as efficient and robust photosensitizers in combination with a molecular catalyst for visible light-driven H 2 production in water, Energy Environ. Sci. 11 (2018) 1752–1761.

[311] X. Xu, L. Xiao, Y. Jia, Z. Wu, F. Wang, Y. Wang, N.O. Haugen, H. Huang, Pyrocatalytic hydrogen evolution by Ba 0.7 Sr 0.3 TiO 3 nanoparticles: harvesting cold–hot alternation energy near room-temperature, Energy Environ. Sci. 11 (2018) 2198–2207.

[312] L. Guo, Z. Yang, K. Marcus, Z. Li, B. Luo, L. Zhou, X. Wang, Y. Du, Y. Yang, MoS 2/TiO 2 heterostructures as nonmetal plasmonic photocatalysts for highly efficient hydrogen evolution, Energy Environ. Sci. 11 (2018) 106–114.

[313] A.-Y. Zhang, W.-Y. Wang, J.-J. Chen, C. Liu, Q.-X. Li, X. Zhang, W.-W. Li, Y. Si, H.-Q. Yu, Epitaxial facet junctions on TiO 2 single crystals for efficient photocatalytic water splitting, Energy Environ. Sci. (2018).

[314] Y. Jiang, H. Ning, C. Tian, B. Jiang, Q. Li, H. Yan, X. Zhang, J. Wang, L. Jing, H. Fu, Single-crystal TiO2 nanorods assembly for efficient and stable cocatalyst-free photocatalytic hydrogen evolution, Appl. Catal. B 229 (2018) 1–7.

[315] X. Kong, X. Xu, Z. Cui, Z. Li, Y. Liang, Z. Gao, S. Zhu, X. Yang, Defect enhances photocatalytic activity of ultrathin TiO2 (B) nanosheets for hydrogen production by plasma engraving method, Appl. Catal. B 230 (2018) 11–17.

[316] M. Maldonado, A. López-Martín, G. Colón, J. Peral, J. Martínez-Costa, S. Malato, Solar pilot plant scale hydrogen generation by irradiation of Cu/TiO2 composites in presence of sacrificial electron donors, Appl. Catal. B 229 (2018) 15–23.

[317] G. Yang, H. Ding, D. Chen, J. Feng, Q. Hao, Y. Zhu, Construction of urchin-like ZnIn2S4-Au-TiO2 heterostructure with enhanced activity for photocatalytic hydrogen evolution, Appl. Catal. B 234 (2018) 260–267.

[318] J. Liu, J. Ke, Y. Li, B. Liu, L. Wang, H. Xiao, S. Wang, Co 3 O 4 quantum dots/TiO 2 nanobelt hybrids for highly efficient photocatalytic overall water splitting, Appl. Catal. B 236 (2018) 396–403.

[319] S.A. Rawool, M.R. Pai, A.M. Banerjee, A. Arya, R. Ningthoujam, R. Tewari, R. Rao, B. Chalke, P. Ayyub, A. Tripathi, Pn Heterojunctions in NiO: TiO2 composites with type-II band alignment assisting sunlight driven photocatalytic H2 generation, Appl. Catal. B 221 (2018) 443–458.

[320] D. Pan, Z. Han, Y. Miao, D. Zhang, G. Li, Thermally stable TiO2 quantum dots embedded in SiO2 foams: Characterization and photocatalytic H2 evolution activity, Appl. Catal. B 229 (2018) 130–138.

[321] D. Spanu, S. Recchia, S. Mohajernia, P. Schmuki, M. Altomare, Site-selective Pt dewetting on WO 3-Coated TiO 2 nanotube arrays: an Electron transfer cascade-based H 2 evolution photocatalyst, Appl. Catal. B 237 (2018) 198–205.

[322] C. Zhang, Y. Zhou, J. Bao, J. Fang, S. Zhao, Y. Zhang, X. Sheng, W. Chen, Structure regulation of ZnS@ g-C3N4/TiO2 nanospheres for efficient photocatalytic H2 production under visible-light irradiation, Chem. Eng. J. 346 (2018) 226–237.

[323] M. Liu, F. Xue, X. Wang, W. Fu, Y. Wang, Y. Lu, N. Li, Conformal deposition of atomic TiO2 layer on chalcogenide nanorod with excellent activity and durability towards solar H2 generation, Chem. Eng. J. 341 (2018) 335–343.

[324] T.H. Chiang, H. Lyu, T. Hisatomi, Y. Goto, T. Takata, M. Katayama, T. Minegishi, K. Domen, Efficient photocatalytic water splitting using Al-Doped SrTiO3 coloaded with molybdenum oxide and rhodium–Chromium oxide, ACS Catal. 8 (2018) 2782–2788.

[325] X. Sun, Y. Mi, F. Jiao, X. Xu, Activating layered perovskite compound Sr2TiO4 via La/N codoping for visible light photocatalytic water splitting, ACS Catal. 8 (2018) 3209–3221.

[326] K.E. Sanwald, T.F. Berto, A. Jentys, D.M. Camaioni, O.Y. Gutiérrez, J.A. Lercher, Kinetic coupling of water splitting and photoreforming on SrTiO3-Based photocatalysts, ACS Catal. 8 (2018) 2902–2913.

[327] S. Zhang, X. Liu, C. Liu, S. Luo, L. Wang, T. Cai, Y. Zeng, J. Yuan, W. Dong, Y. Pei, MoS2 quantum dots growth induced by S vacancy in ZnIn2S4 monolayer: atomic-level heterostructure for photocatalytic hydrogen production, ACS Nano 12 (2017) 751–758.

[328] Y. Wang, H. Suzuki, J. Xie, O. Tomita, D.J. Martin, M. Higashi, D. Kong, R. Abe, J. Tang, Mimicking natural photosynthesis: solar to renewable H2 fuel synthesis by Z-Scheme water splitting systems, Chem. Rev. 118 (2018) 5201–5241.

[329] T. Weller, L. Deilmann, J. Timm, T.S. Doerr, P.A. Beaucage, A.S. Cherevan, U. Wiesner, D. Eder, R. Marschall, A crystalline and 3D periodically ordered mesoporous quaternary semiconductor for photocatalytic hydrogen generation, Nanoscale 10 (2018) 3225–3234.

[330] W. Yuan, L. Cheng, Y. An, S. Lv, H. Wu, X. Fan, Y. Zhang, X. Guo, J. Tang, Laminated Hybrid junction of sulfur-doped TiO2 and a carbon substrate derived from Ti3C2 MXenes: toward highly visible light-driven photocatalytic hydrogen evolution, Adv. Sci. (2018) 1700870.

[331] E. Rahmanian, R. Malekfar, M. Pumera, Nanohybrids of two-dimensional transition-metal dichalcogenides and titanium dioxide for photocatalytic applications, Chem. Eur. J. 24 (2018) 18–31.

[332] Q. Chen, R. Tong, X. Chen, Y. Xue, Z. Xie, Q. Kuang, L. Zheng, Ultrafine ZnO quantum dot-modified TiO 2 composite photocatalysts: the role of the quantum size effect in heterojunction-enhanced photocatalytic hydrogen evolution, Catal. Sci. Technol. 8 (2018) 1296–1303.

[333] Z. Geng, X. Jin, R. Wang, X. Chen, Q. Guo, Z. Ma, D. Dai, H. Fan, X. Yang, Low temperature hydrogen production via water conversion on Pt/TiO2, J. Phys. Chem. C 122 (2018) 10956–10962.

[334] Y.-C. Nie, F. Yu, L.-C. Wang, Q.-J. Xing, X. Liu, Y. Pei, J.-P. Zou, W.-L. Dai, Y. Li, S.L. Suib, Photocatalytic degradation of organic pollutants coupled with simultaneous photocatalytic H2 evolution over graphene quantum dots/Mn-N-TiO2/g-C3N4 composite catalysts: performance and mechanism, Appl. Catal. B 227 (2018) 312–321.

[335] H. Liang, Q. Meng, X. Wang, H. Zhang, J. Wang, Nanoplasmonically engineered interfaces on amorphous TiO2 for highly efficient photocatalysis in hydrogen evolution, ACS Appl. Mater. Interfaces 10 (2018) 14145–14152.

[336] Y. Tan, Z. Shu, J. Zhou, T. Li, W. Wang, Z. Zhao, One-step synthesis of nanostructured g-C3N4/TiO2 composite for highly enhanced visible-light photocatalytic H2 evolution, Appl. Catal. B 230 (2018) 260–268.

[337] J. Oliva, C. Gomez-Solis, L.A. Diaz-Torres, A. Martinez-Luevanos, A.I. Martinez, E. Coutiño-Gonzalez, Photocatalytic Hydrogen evolution by flexible graphene composites decorated with Ni (OH) 2 nanoparticles, J. Phys. Chem. C 122 (2018) 1477–1485.

[338] G. Wang, X. Ma, S. Wei, S. Li, J. Qiao, J. Wang, Y. Song, Highly efficient visible-light driven photocatalytic hydrogen production from a novel Z-scheme Er3+:YAlO3/Ta2O5-V5+ parallel to Fe3+-TiO2/Au coated composite, J. Power Sources 373 (2018) 161–171.

[339] S. Kampouri, T.N. Nguyen, C. Ireland, B. Valizadeh, F. Ebrahim, G. Capano, D. Ongari, M. Mace, N. Guijarro, K. Sivula, Photocatalytic hydrogen generation from a visible-light responsive metal-organic framework system: the impact of nickel phosphide nanoparticles, J. Mater. Chem. A 6 (2018) 2476–2481.

[340] T. Weller, L. Deilmann, J. Timm, T. Dorr, P. Beaucage, A. Cherevan, U. Wiesner, D. Eder, R. Marschall, A crystalline and 3D periodically ordered mesoporous quaternary semiconductor for photocatalytic hydrogen generation, Nanoscale 10 (2018) 3225–3234.

[341] Y. Lu, X. Cheng, G. Tian, H. Zhao, L. He, J. Hu, S. Wu, Y. Dong, G. Chang, S. Lenaerts, S. Siffert, G. Van Tendeloo, Z. Li, L. Xu, X. Yang, B. Su, Hierarchical

[342] P. Wang, Q. Zhou, Y. Xia, S. Zhan, Y. Li, Understanding the charge separation and transfer in mesoporous carbonate-doped phase-junction TiO 2 nanotubes for photocatalytic hydrogen production, Appl. Catal. B 225 (2018) 433–444.

[343] H. Zhao, Z. Hu, J. Liu, Y. Li, M. Wu, G. Van Tendeloo, B. Su, Blue-edge slow photons promoting visible-light hydrogen production on gradient ternary 3DOM TiO2-Au-CdS photonic crystals, Nano Energy 47 (2018) 266–274.

[344] H. Zhang, S. Ni, Y. Mi, X. Xu, Ruddlesden-Popper compound Sr2TiO4 co-doped with La and Fe for efficient photocatalytic hydrogen production, J. Catal. 359 (2018) 112–121.

CdS/m-TiO2/G ternary photocatalyst for highly active visible light-induced hydrogen production from water splitting with high stability, Nano Energy 47 (2018) 8–17.

Dr. Vignesh Kumaravel obtained his PhD in Chemistry from Madurai Kamaraj University, India in 2013. Then, he worked as a Research Professor at Yeungnam University, Republic of Korea. After the successful accomplishment, he designated as a post-doctoral fellow in an industrial project at Universiti Sains Malaysia. Later, he joined as an Assistant Research Scientist at Texas A & M University at Qatar in October 2016. Currently, Vignesh is working in IT Sligo as a Senior Research Fellow in the Renewable Engine project. He has published several scientific research articles in international peer reviewed journals and presented his research findings in several international conferences. He has also delivered two international invited talks in Republic of Korea and India. He is acting as a co-investigator for three major research grants sponsored by Malaysian funding agencies. He is acting as a potential reviewer for many Elsevier, ACS, RSC and Wiley journals. To his credit, he has reviewed more than 50 research articles. He is acting as a guest editor for Catalysts.
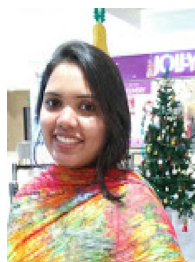
Snehamol Mathew received her bachelor's degree in chemistry and master's degree in Nanoscience and Nanotechnology from Mahatma Gandhi University, India. For her Master's project, she worked in University of British Columbia, Canada. Currently, she is working as Renewable engine Ph.D. student, investigating the fabrication of modified TiO2 nanomaterials for energy and environmental applications under the supervision of Prof. Suresh C. Pillai and Dr. John Bartlett at IT Sligo. Her research focuses on synthesis and characterization of modified TiO2 nanomaterials for photocatalytic hydrogen production, and antimicrobial coatings.

Dr. John Bartlett is Head of Research at the Institute of Technology, Sligo, responsible for developing a research culture based on scholarship, multi-disciplinarity and collaboration, including the development of policy, strategy, administrative systems, quality assurance, budgets, capital infrastructure and project initiatives with internal and external stakeholders/agencies. Dr. Bartlett was founding Director of the Centre for Sustainability and founder of the Contract Research Unit at IT, Sligo. An environmental scientist, his work has included ecotoxicology, environmental impact assessment, waste management technology, renewable energy technology, public access to environmental information, decision making and justice, and public services innovation. He has been Principal Investigator on a number of large scale research programmes funded by HEA (PRTLI), EPA, EU (INTERREG), and other agencies. Recent research includes partnership in an INTERREG funded study into the use of marine algae for renewable fuels. Current research includes support for businesses working in the area of renewable energy and sustainable building technologies, public service systems innovation in the health and environmental areas, and building research capacity in companies in the renewable energy area. He has worked with a number of agencies to contribute to regional and national policy development in Ireland in the areas of sustainability, public services and health innovation.

Prof. Suresh C. Pillai obtained his PhD in the area of Nanotechnology from Trinity College Dublin and then performed postdoctoral research at California Institute of Technology (Caltech), USA. Upon the completion of this appointment he returned to Trinity College Dublin as a Research Fellow before joining CREST-DIT as a Senior Research Manager in April 2004. Suresh joined IT Sligo as a Senior Lecturer in Nanotechnology in October 2013. He is an elected fellow of the UK's Royal Microscopical Society (FRMS) and the Institute of Materials, Minerals and Mining (FIMMM). Suresh was responsible for acquiring more than €4 million direct R&D funding. He has published several scientific articles in leading peer reviewed journals and has presented papers in several international conferences. He has delivered over fifty international invited talks including several key-note and plenary talks. His research work was featured in the BBC London, BBC World Radio, Times UK, 'The Investigators (RTE TV)' programme, RTE-1 TV News, Aljazeera TV, Ocean FM Radio and a number of national and international news media. He was also the recipient of the 'Hothouse Commercialisation Award 2009' from the Minister of Science, Technology and Innovation and also the recipient of the 'Enterprise Ireland Research Commercialization Award 2009'. He is an editor for the journal Environmental Science and Pollution Research (ESPR, Springer) and Editororial Board Member for the Chemical Engineering Journal and Applied Catalysis B (Elsevier).